Non-Contact Process Control Sensors for Nanoliter Dispensing Systems

Dissertation zur Erlangung des Doktorgrades
der Technischen Fakultät
der Albert-Ludwigs-Universität Freiburg im Breisgau

vorgelegt von
Diplom-Ingenieur (FH) Andreas Ernst

Freiburg im Breisgau, März 2013

Dekan

Prof. Dr. Bernd Becker

Referenten

Prof. Dr. Roland Zengerle (Freiburg)

Prof. Dr. Leonhard Reindl (Freiburg)

Tag der Abgabe: 08.10.2012

Tag der Prüfung: 18.03.2013

Lehrstuhl für Anwendungsentwicklung

Institut für Mikrosystemtechnik – IMTEK

Technische Fakultät

Albert-Ludwigs-Universität Freiburg

Erklärung

nach §5(2) der Promotionsordnung.

Ich erkläre hiermit, dass ich die vorliegende Arbeit ohne unzulässige Hilfe Dritter und ohne Benutzung anderer als der angegebenen Hilfsmittel angefertigt habe. Die aus anderen Quellen direkt oder indirekt übernommenen Daten und Konzepte sind unter Angabe der Quelle gekennzeichnet. Insbesondere habe ich hierfür nicht die entgeltliche Hilfe von Vermittlungs- oder Beratungsdiensten (Promotionsberaterinnen oder Promotionsberatern oder anderer Personen) in Anspruch genommen. Niemand hat von mir unmittelbar oder mittelbar geldwerte Leistungen für Arbeiten erhalten, die im Zusammenhang mit dem Inhalt der vorgelegten Dissertation stehen. Die Arbeit wurde bisher weder im In- noch im Ausland in gleicher oder ähnlicher Form einer anderen Prüfungsbehörde vorgelegt.

Freiburg im Breisgau, den

_____

Andreas Ernst

Abstract

This thesis deals with the design, the development and the characterisation of non - contact process control sensors to monitor the droplet ejection process of drop-on-demand dispensing systems in the nanoliter range. The design of the sensors is focussed on a small mounting size to enable a smart integration to the dispensing device. The non - contact working method implements a contamination free and non - invasive measurement technique which does not affect the dispensing process. In contrast to the commonly applied process observation systems, which are mostly unable to provide online process information, the developed sensors serve with analogue signals which enable to realise a real-time process control. As the entire sensors are fabricated in printed circuit board technology, very cost effective competitors to the state-of-the-art systems can be placed on market.

The implementation of the process control sensors is realised by an optical approach, based on the effects of geometrical optics induced by a droplet passing a measurement light beam and a capacitive measurement method, exploiting the interaction of a dispensed droplet with the electric field of an open capacitor. The volumes of the droplets which are measured by the sensors are in the range V = { 5 to 100 nl }. This volume range arises from the applied dispensing system, based on the PipeJet^{TM} technology, and defines the minimum size of the individual measurement transducers.

The application of the optical measurement method is based on the change of the intensity of a measurement light beam while a liquid droplet passes through it. The light beam is present in the flight path of the dispensed droplet and changes it's intensity due to absorption, refraction and reflection effects. This enables to extract droplet dependent analogue signals which are used to analyse several parameters like droplet velocity, droplet shape, malfunctions in the dispensing process or to identify the reproducibility of successively ejected droplets by the correlation of so called droplet 'fingerprint' signals. The smallest detectable droplet was identified to be V_{min}= 1.5 nl, definig the resolution of the optical sensor. The determination of the droplet velocity could be implemented with an error in accuracy of Δu_{ac}= ±0.3 m/s. Additionally, the detection of free flying liquid jets was studied. It was found that the sensor can be applied for the determination of the volume of the liquid jets by the integral of the analogue sensor signals. This however requires to know the velocity of the liquid jet which can not be simply deduced like the velocity of single droplets. The gained results imply the feasibility to realise quantitative process control for micro liter dispensing systems like e.g. dispensing valves or jet ejecting pipettes. An application example is given

which describes the successful improvement of the observation of batch process manufacturing of lateral flow immuno assay test stripes by the application of the optical sensor. The developed optical sensor provides a small and cost effective online process control unit which features functinallity far beyond simple droplet presence detection.

The capacitive measurement method is based on the change of the capacity of an open plate capacitor induced by the presence of a droplet in between the electrodes. The change in capacity yields magnitudes in the region of $\Delta C = 0.7$ to 3 fF for the considered volume range. The measurement capacitor is placed below the dispenser orifice and aligned to the droplet's flight path to avoid the contact of the droplet to the electrodes. To study the occuring physical effects in detail, a multi disciplinary computational fluid dynamics (CFD) simulation was established. The correct physical system description was identified to be the effect of capacitive coupling, implying the specific signal characteristics featuring a leading negative signal dip. The target quantity of the simulation study was the change of the charge on the measurement electrode induced by a passing droplet. Based on the simulation results two different sensor electronic read out circuits were designed, differing in their front - end impedance and amplification circuits. The individual designs of the electronic circuits were improved by an established network simulation. The characterisation of both sensors led to a calibration function which was adapted to the individual sensor circuit performance by the adjustment of the calibration factors. The application of this function enabled to determine the volume of single dispensed droplets in the volume range $V = 20$ to 85 nl with an accuracy of $\Delta V_{sensor1} = \pm 3$ nl for sensor type 1 and $\Delta V_{sensor2} = \pm 4$ nl for sensor type 2 on the fly. The major difference of both sensor types was found in the volume sensitivity which was $S_{i\text{-}sensor1} = 5.3$ mV/nl and $S_{i\text{-}sensor2} = 77.2$ mV/nl. The sensors resolutions were identified to be $V_{min\text{-}sensor1} = 1.5$ nl and $V_{min\text{-}sensor2} = 6.5$ nl. The sensors can also be applied to determine the velocity of the dispensed droplets with an accuracy of $\Delta u_{max} = \pm 0.1$ m/s. The influence of the misalignment of the droplet's lateral position in between the capacitor electrodes could be quantified to falsify the determined droplet volume by an maximum error of $\Delta V = \pm 12$ nl. Also variations of the liquid's relative permittivity were studied in detail by experiment. It turned out that the capacitive measurement principle is mostly independent to changes in the relative permittivity for values $\varepsilon_r > 40$. Therefore, an online process control sensor for the non - contact measurement of the volume of droplets in the nanoliter range, which is largely independend from the media properties, could be implemented.

Zusammenfassung

Die vorliegende Arbeit behandelt die Entwicklung und Charakterisierung von Sensoren zur Überwachug von Nanoliter Dosiersystemen. Diese Sensoren werden eingesetzt um dispensierte Flüssigkeitstropfen, die aus der Düse eines kontaktfrei arbeitenden Dosiersystems abgegeben wurden, während des Flugs zu vermessen. Somit wird eine zeitechte Kontrolle des Dosierprozesses realisiert. Das Design dieser Sensoren zielt auf eine möglichst kleine Bauform ab um eine einfache Integration in die Dosiersysteme zu ermöglichen. Die kontaktfreie Arbeitsweise der Sensoren implementiert eine kontaminationsfreie und nicht-invasive Messtechnik, die keinerlei Einfluss auf den Dosierprozess ausübt. Im Gegensatz zu herkömmlichen Prozesskontrollsystemen, die oft nicht in der Lage sind zeitecht Prozessdaten zu liefern, bieten die entwickelten Sensoren analoge Signale, die zur direkten Kontrolle eines Dosierprozesses herangezogen werden können. Durch die Fabrikation der Sensoren in Leiterplattentechnologie kann eine sehr kosteneffiziente Konkurrenz zu den Standardsystemen an den Markt gebracht werden.

Die Umsetzung der Sensoren wurde durch ein optisches und ein kapazitives Messprinzip realisiert. Die optische Methode basiert auf Effekten der geometrischen Optik, die durch einen Tropfen, der einen Messlichtstrahl passiert, verursacht werden. Die kapazitive Vermessung der Tropfen beruht auf dem Einfluss des Tropfens auf das elektrische Feld eines Messkondensators. Die Größe der zu vermessenden Tropfen liegt im Bereich zwischen 5 und 100 nl. Dieser Größenbereich ergibt sich durch das verwendete PipeJet^{TM} Dosiersystem und definiert die minimale geometrische Größe des Messgebers. Die Signalgenerierung der optischen Methode erfasst die Intensität eines Messlichtstrahls, welche durch die Präsenz eines Tropfens verändert wird. Dies ermöglicht es analoge Signale zu generieren, die zur Ermittlung verschiedener Parameter wie Tropfengeschwindigkeit, Tropfenform oder Störungen im Dosierprozess herangezogen werden können. Außerdem kann die Reproduzierbarkeit aufeinanderfolgender Tropfen anhand der Korrelation der generierten Signale bestimmt werden. Die Auflösung des Sensors wurde durch die Ermittlung des kleinsten detektierbaren Tropfens auf V_{min} = 1.5 nl bestimmt. Die Messung der Tropfengeschwindigkeit konnte mit einem Fehler von Δu_{ac}= ±0.3 m/s umgesetzt werden. Zusätzlich wurde die Bestimmung von dosierten Freistrahlen charakterisiert. Dabei stellte sich heraus, dass das bestimmte Integral unter den generierten Signalen sehr gut mit den Volumina der vermessenen Flüssigkeitsmengen einher geht. Zur korrekten Bestimmung wird allerdings die Geschwindigkeit der Freistrahlen

benötigt, die in diesem Fall nicht einfach bestimmt werden kann. Ein Anwendungsbeispiel für den Einsatz des entwickelten optischen Tropfensensors wurde im Bereich der Kleinserienfertigung von kapillaren Teststreifen gegeben. Es konnte eine online Prozessüberwachung des Liniendruckprozesses verwirklicht werden, was mit herkömmlichen Überwachungssystemen bisher nicht umgesetzt werden konnte.

Die kapazitive Messmethode basiert auf der Veränderung der Kapazität eines offenen Messkondensators während ein Flüssigkeitstropfen diesen passiert. Die hervorgerufenen Kapazitätsänderungen durch Tropfen im betrachteten Volumenbereich liegen im Bereich von $\Delta C = 0.7$ bis 3 fF. Der Messkondensator befindet sich unterhalb der Dosierdüse und ist auf die Flugbahn der Tropfen ausgerichtet, sodass der Tropfen diesen keinesfalls berührt. Zur Untersuchung der auftretenden physikalischen Effekte wurde eine 'Computational Fluid Dynamics (CFD)' Simulation durchgeführt. Die korrekte Systembeschreibung wurde mit dem Model der kapazitiven Kopplung beschrieben, die auch den sehr spezifischen, anfänglich negativen Signalverlauf verursacht. Die betrachtete Zielgröße zur Auswertung der Simulation war die Änderung der Ladung auf der Messelektrode. Basierend auf den Erkenntnissen der Simulation wurden zwei verschiedene elektronische Schaltkreise entworfen, die sich im Wesentlichen in ihrer Eingansimpedanz und dem Verstärkerschaltkreis unterscheiden. Die Entwicklung der Schaltkreise wurde durch entsprechende Netzwerksimulationen unterstützt. Die Charakterisierung der Sensoren führte zur Herleitung einer Kalibrierfunktion die durch Anpassung der Kalibrierfaktoren für beide Senoren verwendet werden konnte. Diese Funktion ermöglichte es das Volumen einzelner Tropfen im Bereich von $V = 20$ bis 85 nl während des Fluges mit einer Genauigkeit von $\Delta V_{sensor1} = \pm 3$ nl für Sensor Typ 1 und $\Delta V_{sensor2} = \pm 4$ nl für Sensor Typ 2 zu bestimmen. Der hauptsächliche Unterschied beider Sensortypen kann in deren Volumensensitivität gesehen werden. Während Sensor Typ 1 eine Sensitivität von $S_{i\text{-}sensor1} = 5.3$ mV/nl bietet, zeigt Sensor Typ 2 eine Sensitivität von $S_{i\text{-}sensor2} = 77.2$ mV/nl. Die Auflösung der Sensoren wurde auf $V_{min\text{-}sensor1} = 1.5$ nl und $V_{min\text{-}sensor2} = 6.5$ nl bestimmt. Als weitere Eigenschaft kann mit den Sensoren die Geschwindigkeit der Tropfen mit einer Genauigkeit von $\Delta u_{max} = \pm 0.1$ m/s bestimmt werden. Fehlereinflüsse wie Abweichungen der Tropfenflugbahn wurden quantitativ untersucht und ein maximal annehmbarer Fehler von $\Delta V = \pm 12$ nl ermittelt. Es wurde erkannt, dass das Messprinzip weitgehend Unabhängig von der Permittivität des Mediums, im Bereich $\varepsilon_r > 40$, arbeitet. Somit konnten echtzeitfähige und kontaktfrei messende Sensoren zur Volumenbestimmung von dispensierten nanoliter Tropfen bereitgestellt werden.

Own Publications

Journal Articles

A. Ernst, W. Streule, N. Schmitt, R. Zengerle, P. Koltay, „A capacitive sensor for non-contact nanoliter droplet detection“, Sensors and Actuators A 153 (2009), pp. 57–63

A. Ernst, L. Ju, B. Vondenbusch, R. Zengerle, P. Koltay, „Noncontact Determination of Velocity and Volume of Nanoliter Droplets on the Fly“, IEEE Sensors Journal, Vol. 11, No. 8, 2011, 1736-1742

A. Ernst, K. Mutschler, N. Paust, R. Zengerle and P. Koltay, „Numerical investigation of electric field characteristics with respect to capacitive detection of free flying droplets“, accepted for publication at Sensors online

J. Trondle, A. Ernst,W. Streule, R. Zengerle, P. Koltay, „Non-contact optical sensor to detect free flying droplets in the nanolitre range“, Sensors and Actuators A 158 (2010), pp. 254–262

Patent Applications

A. Ernst, C. Steinert, L. Tanguy, P. Koltay, „Vorrichtung und Verfahren zur Abgabe oder Aufnahme eines Flüssigkeitsvolumens“, deutsche Patentanmeldung 102012209314.1, 01.06.2012

S. Bammesberger, A. Ernst, P. Koltay, N. Losleben, L. Tanguy, „Dispenser combining a syringe pump and an impulse generator“, 30944 EP, 08.05.2012

Conference Proceedings

A. Ernst, W. Streule, R. Zengerle, P. Koltay, „ Non-contact detection of free flying nanoliter droplets “, Proc. of Transducers ’07 and Eurosensors XXI, Lyon, 2007

A. Ernst, W. Streule, R. Zengerle, P. Koltay, „Kontaktfreie Detektion von frei fliegenden Nanoliter-Tropfen“, Proc. of Sensoren und Messsysteme, Ludwigsburg, 2008

A. Ernst, W. Streule, R. Zengerle, P. Koltay, „Quantitative volume determination of dispensed nanoliter droplets on the fly“, Proc. of Transducers ’09, Denver, 2009

A. Ernst, B. Vondenbusch, R. Zengerle, P. Koltay, “Non-contact volume de-

termination of free flying nanoliter droplets using an adjustable capacitive measurement bridge“,Smart Sensors, Actuators, and MEMS V, Vol. 8066, 2011, p. 806620

A. Ernst, R. Zengerle, P. Koltay, „Kontaktfreie quantitative Volumenbestimmung dispensierter Nanolitertropfen mittels eines kapazitiven Tropfensensors“, Tagungsband Mikrosystemtechnik-Kongress, Darmstadt, Deutschland, 2011, 799-802

K. Mutschler, A. Ernst, N. Paust, R. Zengerle, P. Koltay, “Capacitive detection of nanoliter droplets on the fly - investigation of electric field during droplet formation using CFD-simulation“, 16th International Solid-State Sensors, Actuators and Microsystems Conference (TRANSDUCERS), 2011

A. Yusof, L. Riegger, N. Paust, A. Ernst, R. Zengerle, P. Koltay, „A Non-Invasive Single Cell Dispensing Approach for 2-Dimensional Micro-Patterning “, Proc. of Actuator ’10, Bremen, 2010

N. Lass, A. Tropmann, A. Ernst, R. Zengerle, P. Koltay, „Rapid prototyping of 3D microstructures by direct printing of liquid metal at temperatures up to 500°C using the starjet technology“,16th International Solid-State Sensors, Actuators and Microsystems Conference (TRANSDUCERS), 2011

D. Liang, A. Gross, J. Schöndube, S. Rubenwolf, A. Yusof, A. Ernst, R. Zengerle, G. Roth, P. Koltay, „Improved Machine Vision for Single Cell Printing“, Tagungsband Mikrosystemtechnik-Kongress, Darmstadt, 2011, 891-894

A. Madjarov, W. Streule, P. Prokopp, A. Ernst, R. Zengerle, P. Koltay, „Nanoliter dispensing on pipetting workstations by disposable PipeJet-tips“, Proc. of the13th International Conference on New Actuators, Bremen, Germany, 16.-18.06.2012, pp. 430-433

D. Liang, J. Zhang, L. Tanguy, A. Ernst, P. Koltay, R. Zengerle, „Nanoliter droplet characterization using vibrating crystal sensor with surface-attached polymer hydrogel coating“, Proc. Eurosensors XXVI, September 9-12, 2012, Kraków, Poland

K. Mutschler, W. Kunert, R. Ingenpaß, K. E. Grund, L. Tanguy, A. Ernst, R. Zengerle, P. Koltay, „EndoMediskop - Trans-Endoscopic Microinjection for Flexible Endoscopy“, accepted as oral presentation at BMT Jena 2012

D. Liang, L. Tanguy, A. Ernst, R. Zengerle, P. Koltay, „Novel Gravimetric Calibration Method for Nano Liter Liquid Handling Devices“ accepted as poster presentation at MFHS-2012 Conference Enschede

D. Liang, T. G. Muniyogeshbabu, L. Tanguy, A. Ernst, R. Zengerle1, P.

Koltay, „Online Liquid Calibration Technologies“, accepted as poster presentation at MFHS-2012 Conference Enschede

S. Bammesberger, A. Ernst, L. Tanguy, P. Koltay, R. Zengerle, „A Calibration-Free, Disposable, Non-Contact Reagent Dosing Cartridge for the Sub-µL Range“, accepted as oral presentation at MFHS-2012 Conference Enschede

L. Tanguy, A. Ernst, S. Bammesberger, R. Zengerle, P. Koltay, „Pressure Driven and Regulated Dispenser for the Microliter Range“, accepted as oral-presentation at MFHS-2012 Conference Enschede

N.Lass,L.Riegger, A. Ernst, R. Zengerle, P. Koltay, „Enhanced Liquid Metal Micro Droplet Generation by Pneumatic Actuation Based on the StarJet Method“, accepted as oral presentation at MFHS-2012 Conference Ensched

S. Bammesberger, S. Kartmann, L. Tanguy, D. Liang, K. Mutschler, A. Ernst, P. Koltay, R. Zengerle, „A Low-Cost, Normally Closed, Solenoid Valve for Non-Contact Dispensing in the Sub-µL Range“, accepted as poster presentation at MFHS-2012 Conference Enschede

Table of Contents

Chapter 1
Introduction

This thesis deals with the development and characterisation of non-contact process control sensors for the online monitoring of low volume non-contact dispensing systems. The constantly growing market in the field of non-contact dispensing devices for the application of liquid droplets in the nanoliter range implies an increasing need of proper process control systems to monitor the accuracy and reproducibility of the dispensing processes [1; 2]. Online, non-contact sensors measure or detect dispensed liquid quantities without any contact to the liquid to avoid contamination or loss of the medium and enable the inline extraction of process information.

The selective application of well defined aliquots of liquid in the pico- to nanoliter range has gained in interest for many different industrial- as well as for research applications in the past years [3]. The release of small amounts of liquid can be performed by several different dispensing techniques. The commonly applied techniques can basically be separated into two different sectors, which are the contact and non-contact dispensing applications. A non-contact dispensing system generates single liquid quantities which are released as free flying droplets or jets out of a dispenser nozzle. This means that each single droplet has to traverse a certain distance through ambient air, defined by the distance of the dispenser orifice to the target substrate. Several different techniques are applied to generate single free flying droplets [4]. The variety of different techniques won't be studied in detail in this work, rather the dispensing system used to accomplish the sensor characterisation is explained in some detail.

Beside the most common application of non-contact dispensing systems, the inkjet office printers which presents 28% of the complete MEMS market [5], also many other fields require well defined aliquots of liquids, representing considerable market shares. One of these is the life-science sector, especially the field of medical- and pharmaceutical research. Small liquid quantities are required to find novel drugs, using combinatorial chemistry and to perform hundreds and thousands of experiments by high throughput screening (HTS) [6-10]. Another application in the field of life-science, requiring well defined liquid quantities, is the printing of lateral flow assays [11]. Single lines of sample liquid are printed to generate the identification- or detection lines on non-woven target materials. Such test stripes enable to identify the incidence of specific analytes in a sample assay, applicable in the field of point-of-care diagnostics [12; 13]. The detection lines are often printed by the application of

single droplets, which merge on the surface of the target material to generate the desired lines. Beside the required tiny geometry of the lines, which is defined by the size of the droplets as well as by the absorption properties of the absorbing material, the accurate volume application of the samples is of highest interest. The quantification of such tests requires to know the amount of the accumulated ligand and receptor molecules (antigen/ antibody) in the printed lines precisely, which are proportional to the applied liquid volume for a specific concentration [14].

However, not only life-science applications require well defined liquid quantities. Also several industrial processes constitute the application of single droplets, e.g. for the fabrication of solar cells flux melting agents are required to enable the reliable soldering of conductor strips to the cells' surface. The quantity of the applied flux melting agent has to be well defined and applied on the target areas only. Misalignments imply an certain impairment of the performance of the final solar cell due to the aggressive material properties. Also other applications like the dosage of lubricants, cooling agents or adhesives [15; 16] are daily required processes which have to be monitored and documented to guarantee correct production processes. Even the production of small soldering bumps is realised by non-contact dispensing where liquid metal is dispensed to form small metal balls [17].

The methods of standard process control systems to monitor non-contact dispensing processes are rarely documented. Commonly, dispensing devices are characterised and calibrated by the producer and offered with specific performance data sheets. This however, does not guarantee that even well performing systems constantly serve with adequate metered liquid quantities. Furthermore, occurring malfunctions in the process might influence the dispensing performance up to the case of absence of the required droplets. To investigate the status and performance of a dispensing process, online control systems are required to investigate any alternation in the performance of the applied dispensing process. The standard process control systems, applied to monitor the performance of non-contact dispensing processes, are expensive and often imply many drawbacks for the implementation at fully automated industrial product lines. Big installation sizes and indirect measurement principles, e.g of stroboscopic cameras or fluorescent readers, are prohibitive to the application in a wide range of relevant settings. Also the demand to get in contact with the measured liquid, which implies contamination or even the loss of measured liquid, excludes the methods of gravimetric measurement by high precision balances or contact flow measurement to be applied for online process control. To overcome such drawbacks recently novel smart system integration approaches are reported like the capacitive observation of the

movement of the liquid meniscus inside a dispenser nozzle [18; 19] or the miniaturisation and improved evaluation of stroboscopic imaging systems [20]. Historically the interest in detecting free flying droplets emerged in the early 1940's. Several methods were reported to measure the size of droplets and their distribution in clouds. In 1949 A.C. Best published a review paper including the applied methods and their results which are mostly based on the 'filter paper method' [21]. But these early approaches are not applicable to realise non-contact process control systems for the measurement and detection of dispensed droplets. The presented methods mostly require to get in contact to the measured liquid and imply the loss of the liquid. But also contactless measurement approaches like the measurement of light scattering caused by droplets [22] or the use of pulsed doppler radars [23] were reported before 1968. The first approach which implies a feasibility to realise a non-contact sensor was reported in 1968 by W.P. Winn [24]. He investigated the interaction of a liquid droplet with the electrical field of an open plate capacitor. A theoretic approach for the non-contact measurement is given whereas the presented experiments depend on contact methods only. Another field which is intensively researched over the years is the generation and atomization of sprays. In this field many different process control techniques are reported, which are probably qualified for single droplet detection in the nanoliter range as well. Huimin Liu categorized several different approches into four specific sectors: mechanical-, electrical-, optical- and acoustical methods. A list of the reported principles is given in table 1.1. Considering the measurable droplet size, which is given in column 3, techniques which are able to detect droplets with diameters $d > 100$ µm could be suitable to cope with the considered requirements in this work. More detailed information about the listed techniques can be taken from [25].

Table 1.1 Droplet detection principles for spray generation applications [25]

Category	Method	Size range [µm]
Mechanical	Collection of droplets on slides or in cells	> 3
	Cascade impactor	
	Molten-wax and frozen-drop techniques	
	Mechanical sieving of metal powder	

Table 1.1 Droplet detection principles for spray generation applications [25]

Category	Method	Size range [µm]
Electrical	Pulse counting technique	
	Charged wire technique	
	Hot wire technique	1 - 600
Optical	***Imaging***	> 5
	Photography	
	Videography	
	Holography	5 - 1000
	Non-imaging	5 - 3000
	Light scattering interferometry	
	Phase-Doppler anemometry	0.5 - 3000
	Light intensity deconvolution technique	0.2 - 200
	Light scattering technique	10 - 250
	Malvern particle analyzer	1 - 500
	Polarization ratio particle sizer	
	Intensity ratio method	
	Phaseotpical-microwave method	
	Dual-cylindrical wave laser technique	
Acoustical	- - -	5- 30

1.1 Aim and structure of the thesis

The aim of the presented work is focused on the development of process control sensors applicable to non-contact, drop on demand dispensing systems in the nanoliter range. The applied measurement technique needs to monitor a dispensed liquid quantity directly after it is released out of the dispenser nozzle and before it impinges on the target substrate to realise an online process control like illustrated in figure 1.1. The applied measurement technique needs to work without any contact to the dispensed liquid to avoid contamination or loss of the liquid droplets.

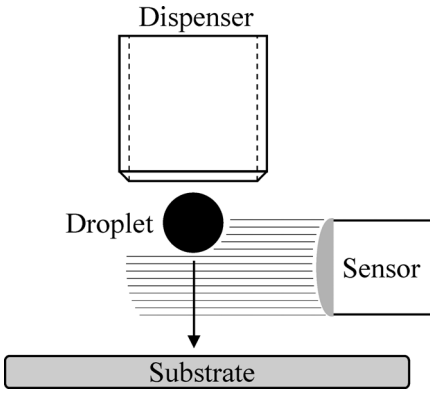

Figure 1.1 Basic principle and major specification for the development of the non-contact droplet detection sensors

Furthermore, a small mounting size is required to enable a smart system integration to the dispenser unit. The application of a low cost fabrication technology allows for a price effective alternative to the currently available state-of-the-art systems. The target volume range of the droplets to be measured is defined to be V= { 5 - 100 nl} which arises from the applied droplet generation unit. Beside the mechanical requirements and the basic specification for the measurement technique, the requested sensor performance is structured in different fields of practical relevance which are identified by the phrase 'priority' like follows:

Priority I: Detection of the presence or absence of a single droplet, indicated by a signal peak.

Priority II: Monitoring of a droplet 'fingerprint signal' to realise a semi-quantitative evaluation of a dispensing process. Fingerprint signals enable to quantify the reproducibility of a dispensing process by the correlation of the individually droplet generated signals.

Priority III: Quantitative measurement of certain droplet parameters like droplet volume or droplet velocity by correct interpretation of the generated signals.

Priority IV: Media independent droplet volume determination.

Whereas priority I leads to purely qualitative information and is a minimum requirement for the realisation of a droplet detection system, priority IV seems to be hardly implementable. Quantitative sensor performance has to be specified at least by the definition of the sensor properties like accuracy,

defined by the variation of the extracted values to a corresponding reference, the significance, given by the ratio of the extracted value to the measured quantity (e.g. [V/nl]) and the resolution, defining the smallest detectable value related to a defined signal to noise ratio (SNR). The implementation of the given specifications is realised by the development of an optical and an capacitive measurement technique. The optical measurement technique is based on geometrical optic effects induced by a liquid droplet which passes a measurement light beam. The capacitive measurement method is based on the interaction of a liquid droplet with the elctric field of an open plate capacitor. Theoretically, both methods are able to cope with the given requirements. The developement and characterisation of the different measurement techniques are described and discussed in detail in this work and are the core topic of the thesis. The implementation of the work is structured in seven chapters:

Chapter 1 was already read at this point, which contains the introduction to the topic and motivates the need of the aspired devices.

Chapter 2 introduces the currently available state-of-the-art techniques in the field of process control for non-contact dispensing devices. Beside several standard techniques which are commercially available on market, recently published research results and patent specifications are presented. Chapter 2 points out the limitations and drawbacks of these systems which have to be overcome by the developed methods in this work.

Chapter 3 provides the theoretical fundamentals to the different considered sensor techniques and the applied tools. The individual basics are given in separate sections to simplify the understanding of the different working principles and the presented proceedings.

Chapter 4 describes the applied nanoliter dispensing system used for experiments. It briefly introduces the working principle of the dispenser which helps to understand the parameter adjustability of the device. This is an essential detail to generate droplets of defined volume and velocity for the characterisation of the developed sensors.

Chapter 5 starts with the proof of different optical droplet detection concepts. It continues with the improvement and characterisation of the prefered method. Beside the detection of single liquid droplets also the measurement of ejected liquid jets was characterised. Chapter 5 ends with a first application example, implementing a novel online observation method of an imprinting process for the production of lateral flow immuno assays (LFIA).

Chapter 6 presents theoretical considerations of the capacitive droplet measurement method. It starts with analytical calculations regarding the

capacitive measurement principle followed by a comprehensive CFD simulation study of the principle's physics.

Chapter 7 deals with the fabrication and characterisation of two different electronic read out circuitries realised to implement the capacitive droplet measurement method. The chapter ends with the experimental validation of the achieved sensor performance.

Finally, the thesis is summarized in **chapter 8** and ends with an outlook for future progress on the presented topic.

Chapter 2
State of the Art

To open the technical part of this thesis, a detailed overview of the state-of-the-art techniques to monitor the performance of non - contact dispensing systems is given in the following sections of chapter 2. Since online process control systems for the observation of free flying droplets in the nanoliter range are rarely documented and hardly commercial available, some of the commonly applied techniques in practice as well as a few published methods for the field of focus are illustrated.

2.1 Gravimetrical volume determination

One of the most common principles applied for the determination of the volume of dispensed liquid droplets is the application of highly precise gravimetric balances. These devices provide the possibility to resolve liquid quantities down to a mass of m = 100 ng (equivalent to a volume of V = 100 pl for water droplets), featuring a maximum measurement range of 2.1 g [26, 27]. Obviously, such balances are extremely sensitive to environmental influences like vibrations or air streams. Also high evaporation rate is a considerable issue for the correct determination of liquid quantities in the nanoliter range, which corresponds to masses in the range of a few µg.

The determination method of droplet volumes in the nanoliter range can be realised by weighing the mass of single droplets, followed by the calculation of the droplet volume via media density. Thereby, influencing factors like temperature or ambient pressure have to be considered to achieve accurate results. Whereas single nanoliter droplets can be measured one by one, smaller droplets (e.g. in the picoliter range) under-run the resolution of the balance. Multi-droplet weighing processes have to be applied where several droplets have to be dispensed on the weighing table successively. The total mass of the complete dispensing sequence has to be divided by the number of dispensed droplets to estimate the average mass of the droplets. The application of such processes require high repeatability of the dispensing device to minimize the measurement errors. The effect of evaporation increases especially for small droplets. Even absent droplets can not be detected, thus the results achieved by a multi-droplet weighing process should be taken as rough droplet volume estimation only.

Figure 2.1 High precision balance - Sartorius SE 2 [26].

The standard process for the determination of a droplet's volume by a gravimetrical balance is performed by dispensing the liquid quantity onto the weighing table of the balance. Due to the mass impact on the table at the impingement of the droplet and the mentioned evaporation rate, a complex signal analysis procedure has to be applied to enable an accurate determination of the liquid quantity. To improve the accuracy of the weighing procedure environmental influence factors have to be eliminated. Vibrations occurring from laboratory work are damped by pneumatic supported installation platforms. Heavy granite tables are beared on air cushions to compensate mechanical movement from the ground floor. Disturbing airstreams are prevented by wind shield covers which surround the complete measurement setup. Beside the environmental shielding, the essential part for a precise measurement is the software controlled weighing procedure. Ideally a balance would not imply any measurement error, thus a weighing process could be performed by recording two values only. One before a droplet impinges on the weighing table (x_a) and one thereafter (x_b). Therefore, the mass of the measured droplet would be given simply by $m_{drop} = x_b - x_a$. However, realistic contemplations imply the consideration of several errors which occur during the weighing process. Beside systematic errors, caused by the used balance and the measurement setup, also random errors can occur, which have to be considered by a proper error estimation. Therefore, a suitable error assessment is established, which needs to be applied for each weighing experiment. Such an error assessment requires the consideration of several different errors which might occur during a measurement procedure. The first considerably error is the balance measurement error itself Δx_{bal} which is typically provided by the balance data sheet.

This error is present for each value given by the balance and is considered by the gauss law of error propagation [28]:

$$m_{drop} \pm \Delta m_{drop} = (x_b - x_a) \pm \sqrt{2 \cdot (\Delta x_{bal})^2} \tag{2.1}$$

where, m_{drop} is the droplet mass and Δm_{drop} represents the systematic mass error. Beside such standard errors the influence of the mentioned environmental errors are considered by a specific measurement procedure. Several datapoints are acquired before ($x_{a(1\text{-}n)}$) and after ($x_{b(1\text{-}n)}$) the droplet impinges on the balance table which is typically preloaded with the measured liquid. Since the environmental influences (vibration, evaporation, etc.) are recognized by the balance and reflected by the single datapoints, the final measurement error can be estimated by the definition of the irregularity of the acquired data sets related to their corresponding linear regression x^{LR}. These irregularities are considered by the application of statistical prognosis interval estimation with 5% probability of error [28]. The prognosis interval defines a prospective value, which says that 95% of all successive measurement points will be in between the calculated boundaries and is calculated like follows:

$$x^P = x^{LR} \pm s \cdot t_{n-2;\left(1-\frac{\alpha}{2}\right)} \cdot \sqrt{1 + \frac{1}{n} + \frac{(\bar{x} - x)^2}{\sum_{n=1}^{n} (x_n - \bar{x})^2}} \tag{2.2}$$

with, x^P is the positive and negative boundary value of the prognosis interval, x^{LR} is the discrete value of the linear regression of the measured sequence before or after the dispense, s is the standard deviation of the sequence, $t_{n\text{-}s;1\text{-}a/2}$ quantile of the students t distribution, n the number of datapoints, x the discrete datapoint and $\bar{x}$ the mean value of the set of datapoints. Applying the described method enables to determine the weight of a dispensed droplet including an error assessment to define a proper mass deviation, considering all environmental influences like displayed in figure 2.2. The determination of the droplet mass m_{drop} requires the interpolation of the linear regressions x^{LR}, calculated from the acquired data sets before and after the dispense, to the actual time of the dispense t_{dis}. The time t_{dis} is monitored by the measurement hardware and transferred to the software application.

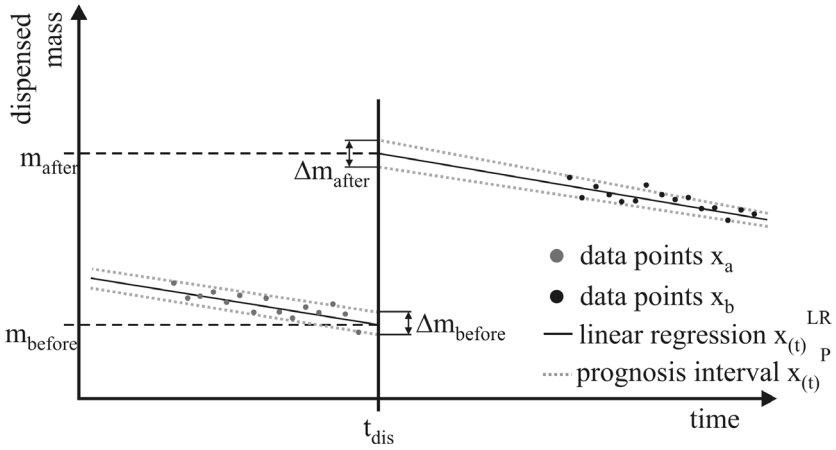

Figure 2.2 Error assessment to determine the accuracy of the gravimetrical droplet volume determination procedure. Applied prognosis interval estimation enables to determine the weighing error quantitatively.

This procedure enables the determination of the measured weight before (m_{before}) and after (m_{after}) the dispense. The final mass m_{drop} is calculated by the subtraction of m_{after} and m_{before}. To estimate the measurement error $\Delta m_{regression}$ the discrete values of the prognosis intervals for both data sets are calculated at time t_{dis}. Therefore, the prospective values of the interval at t_{dis} (Δm_{before}; Δm_{after}) can be taken to calculate a significant measurement error, applying gauss law of error propagation. The final equation to calculate the droplet mass can be written as:

$$m_{drop} = m_{after} - m_{before} \pm \Delta m_{regression} \tag{2.3}$$

Finally, the droplet volume can be calculated considering the density of the weighted sample liquid. A considerably drawback of the application of highly precise balances is the loss of the weighted liquid quantity, thus the use of the described method for online quality control is not applicable. Also the required complex setup to protect the measurement from the influence of environmental errors prohibits an industrial application.

2.2 Stroboscopic imaging

A further method to measure the volume of a dispensed droplet is the application of a stroboscopic set up. Such systems require a camera featuring very fast shutter times combined with an adapted high intensity illumination.

Several methods and algorithms are published, applicable for the determination of droplet properties by image recording [22, 29]. Basically, a camera (CCD or CMOS technology) is installed underneath the dispenser unit, facing the illumination source, thus a dispensed droplet passes the lense of the camera in the bright field.

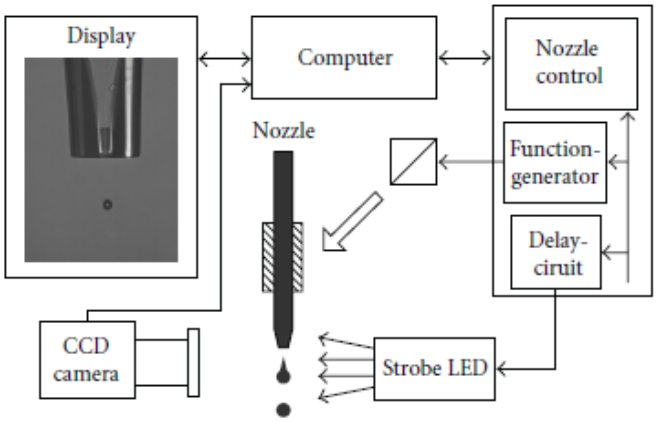

Figure 2.3 Sketch of a stroboscopic imaging setup, including the block diagram of the connection of the required components [20].

The camera trigger to capture one picture has to be synchronized with the actuation of the dispensing device. This enables to record droplets at different positions and delays after their ejection out of the dispenser nozzle. A block diagram of a stroboscopic setup is given in fig. 2.3. One recorded picture of a single droplet can be used to determine the volume of a droplet by the measurement of the droplet diameter. Basically, the volume of a sphere can be calculated by:

$$V_{sphere} = \frac{4}{3} r^3 \pi \tag{2.4}$$

where r is the radius of the sphere. This equation holds only for the determination of the volume of absolute spherical shaped bodies. The challenge in case of droplet volume calculation is the consideration of non-spherical geometries. Dispensed droplets leave a nozzle mostly as non-spherically shaped bodies, thus specific algorithms have to be applied to calculate their volume [22, 29]. From equation 2.4 can be seen that the radius of the measured sphere influences the volume V_{sphere} by the power of 3, which implies the need for very high image resolutions to enable the measurement of correct radii.

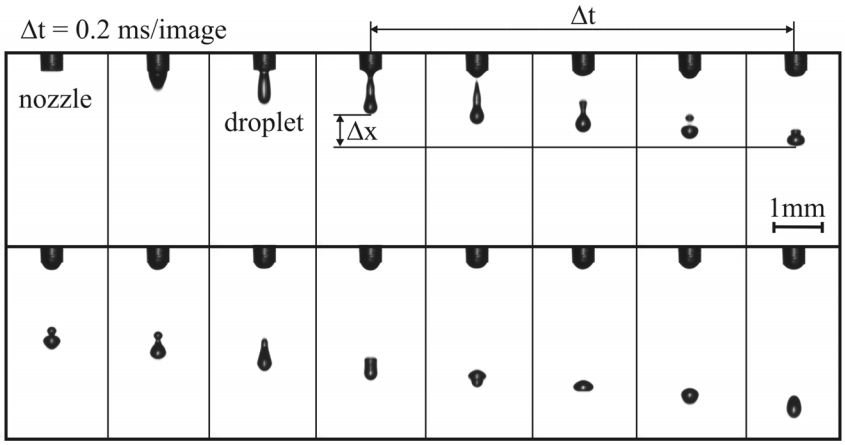

Figure 2.4 Stroboscopic droplet image sequence of a PipeJet™ dispensing process recorded with a specific stroboscopic setup from BioFluidix GmbH [30].

But deviations in the evaluation of pixel graphics can not be avoided, thus entail high volume errors applying this method for the volume determination. However, the stroboscopic imaging method is helpful to investigate further droplet characteristics, like the droplet velocity. Therefore, a sequence of single droplets have to be recorded, whereas the time delay between dispenser actuation and camera trigger has to be increased for each successive droplet, see fig. 2.4. This enables to measure the distance Δx which the droplet has moved in a specific time interval Δt to calculate its velocity $u_{droplet}$.

$$u_{droplet} = \frac{\Delta x}{\Delta t} \tag{2.5}$$

Considerable drawbacks for the application of stroboscopic cameras are the mentioned high volume error and the big mounting size. Furthermore, online process control can not be realised by the required complex image processing which takes time to be completed. Also the high initial costs, which are > 10000 € is a negative aspect for the application of stroboscopic cameras for process control of dispensing systems.

2.3 Fluorescence measurement (fluorometry)

Fluorescence methods are commonly applied in biochemistry and medical research to measure the volume of liquid quantities on a target substrate, like well plates or microscope slides. It is based on the quantitative detection of fluorescence pigments, mixed to a sample liquid [31].

Fluorescence is an optical phenomenon which describes the molecular absorption of light energy at one specific wavelength by a material and the almost instantly triggered emission of light at a different, longer wavelength [32]. Fluorometry is the measurement of the fluorescence intensity and is used to determine the amount of fluorescent pigments in a sample liquid. This amount is proportional to the analyte concentration of the measured sample. Fluorescence is measured by the use of a so called fluorometer. The quantitative results of a fluorometer are given in counts. One count is a dimensionless light unit. To classify the values in a volume scale, measurements with calibrated liquids are required. The number of counts varies with the concentration of the pigment and the distribution of the fluid in a well or liquid spot on a microscope slide, thus the volume of the liquid. The application of fluorometry to determine the volume of a droplet, requires the mixture of fluorescent labelled markers to the sample liquid to estimate the amount of markers in the droplet. Therefore, the droplet has to be dispensed on a suited support material to be analyzed in an external fluorometer by the described procedure.

2.4 Nozzle integrated capacitive sensor

One of the latest published techniques to realise an online process control for contactless dispensing systems is the nozzle integrated capacitive sensor, developed at University Delft in 2009. The measurement technique is based on a couple of silicon electrodes integrated in the nozzle of a bubble jet system to create a measurement capacitor, see fig. 2.5. The sensor is fabricated in MEMS technology, whereas the silicon electrodes are embedded in the sidewall of a bubble jet's nozzle.

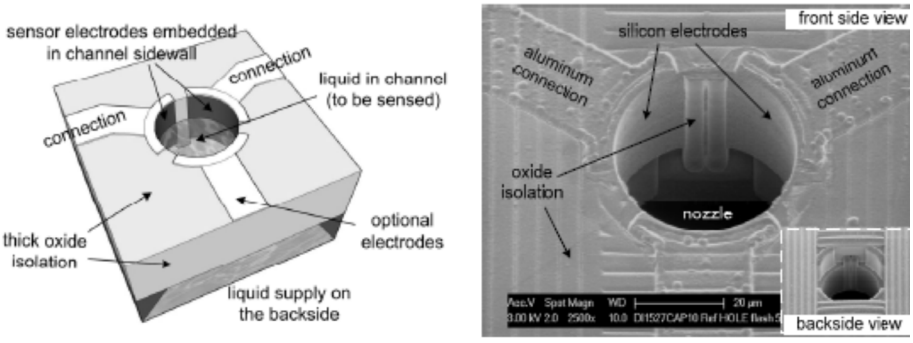

Figure 2.5 Principle draft and SEM image of the nozzle integrated capacitive sensor [19].

Based on the change in capacity, caused due to variation of the dielectric in between the electrodes, this technology enables the measurement of movement of a liquid meniscus within the dispenser nozzle. A liquid can be seen as dielectric material, thus changes in the filling level of the nozzle go along with changes in the average capacity of the sensor' measurement capacitor. The signals are recorded via a complex lock-in amplification technique. Therefore, a dispensing process can be monitored with respect to filling behaviour of the nozzle, clogging and qualitative dispensing performance. However, quantitative results of measuring droplet volumes are not reported yet, thus the performance of such a system can not be quantified [19].

2.5 Droplet detection applying two parallel light beams

The method explained in the following is part of the japanese patent specification JP2004/251818 published in 2004 [33]. The described droplet detection system consists of two parallel infinitesimal light beams, which are separated by a defined distance in vertical direction. The light emitted from a light emitting diode (LED) is directed by a lense and slendered by an adapted aperture to generate each of the measurement light beams. The light intensity is detected by two photo detectors (PD) which are installed opposite the light emitting sources facing the aperture. The space in between the components needs to be big enough to enable a dispensed droplet to pass through. Both of the photo detectors are connected to a separate memory via individual A/D converters, enabling to store the signal characteristics of each photo detector separately. The complete system is installed underneath a dispensing device, aligned to the systems dispensing nozzle, thus a dispensed droplet passes the described light beams. The detection procedure is triggered by the actuation of the used dispensing device and initiates the recording of the photo detector generated signals by the memory components for a defined time. The sampling rate of the A/D converters, which is essential for the volume calculation later, is given by a connected time defining clock component. A droplet, which is ejected out of the dispenser nozzle, passes the light beams and entails a specific characteristics of the recorded datasets like shown in fig. 2.6. The volume calculation is started after each dispensing process by the following procedure, which is based on the information stored in the recorded data. In first instance, the droplet velocity is determined by the ratio of the distance between the two light beam to the time t which a droplet needs to transit the distance from the first beam to the second (see fig. 2.6), given by the initiation of the two signals.

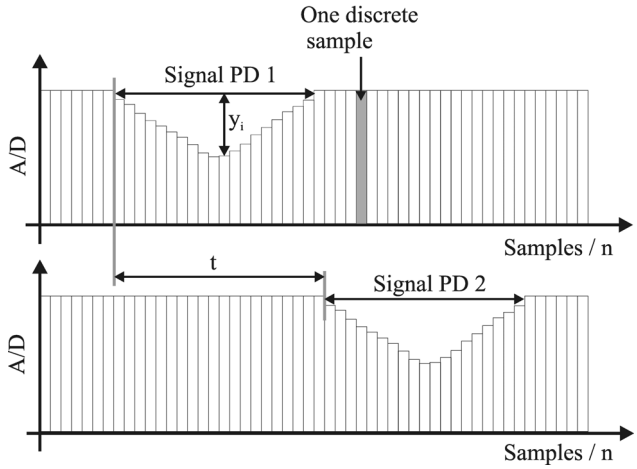

Figure 2.6 Visualisation of a dataset, generated by a droplet passing the two infinitesimal light beams.

The calculation of the droplet volume is based on the time discrete consideration of the detection process with respect to the sample frequency. Assumed that a droplet has a constant velocity, it travels a defined distance at one sampling period. The sensor response for each sampling period is recorded by the memory and can be seen as a rectangular with a certain height, c.f. fig. 2.6. This height y_i is proportional to the shading at the photo detector caused by a droplet, thus to the actually detected radius. Therefore, a droplet can be considered as body which is sliced into a specific amount of discrete cylindrical volume elements defined by the sampling frequency *f*. The volume V_i of each element can be calculated by:

$$V_i = (y_i + \alpha)^2 \cdot \pi \cdot v_{droplet} \cdot \frac{1}{f} \tag{2.6}$$

For error compensation, a factor α is considered, which is an experimentally found value. Finally, the volume of the detected droplet is the sum of each calculated volume for one sampling sequence at each sampling period:

$$V_{droplet} = \sum V_i \tag{2.7}$$

Apart from this method other optical droplet detection approaches are reported in different patent applications, which are based on the application of one or multiple light sources [34- 41]. However, there are no experimental proofs available, thus this methods are not noted here in detail.

2.6 Flow measurement

A commonly applied process control system used for online control of syringe solenoid dispensing systems is the use of MEMS flow sensors. These sensors are invasively installed into the liquid supply path of the dispensing system and enable the measurement of the liquid's movement inside the system. Therefore, aspiration as well as dispensing processes can be monitored in real time. The principle of such a controlled syringe solenoid dispensing device is published in the patent specification EP1327152B1 by the Seyonic SA, Swizerland, in 2001 [42 - 44]. A sketch of the system in given in fig. 2.7. A MEMS flow sensor, installed close to the nozzle, measures the movement of the system liquid, which acts as hydraulic medium to transmit the pressure, which is adjusted by a pressure controller, see fig. 2.7. The non- compressible system liquid enables a high acceleration of the sample liquid to reach the required jetting speed at the nozzle. While the solenoid valve opens, the sample liquid flows through the nozzle, whereas the sensor measures the flow rate of the liquid. The monitored signals, see fig. 2.8, allow for the calculation of the volume of the system liquid which passed the sensor during the active dispense time by integration of the flow signal. Assumed that the volume of the passed system liquid equals the dispensed sample liquid, an online process control for the mentioned systems is realised. The major drawback of such a system is the invasive measurement technology, which requires the contact to the liquid inside the system, thus omits the detection of malfunctions occurring at the nozzle e.g. due to nozzle wetting. Also the slow response time of such difference pressure based flow sensors disables the application of this method for the measurement of liquid quantities below V = 25 nl.

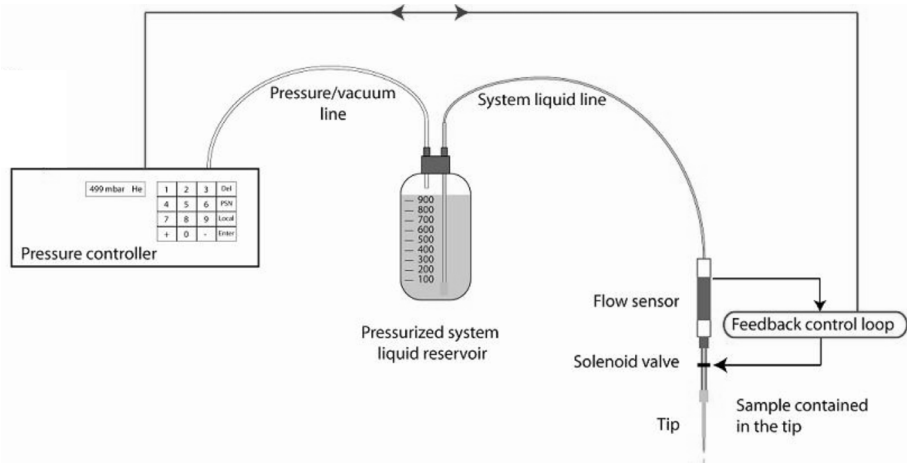

Figure 2.7 Sketch of a flow controlled dispensing system offered by Seyonic SA [43].

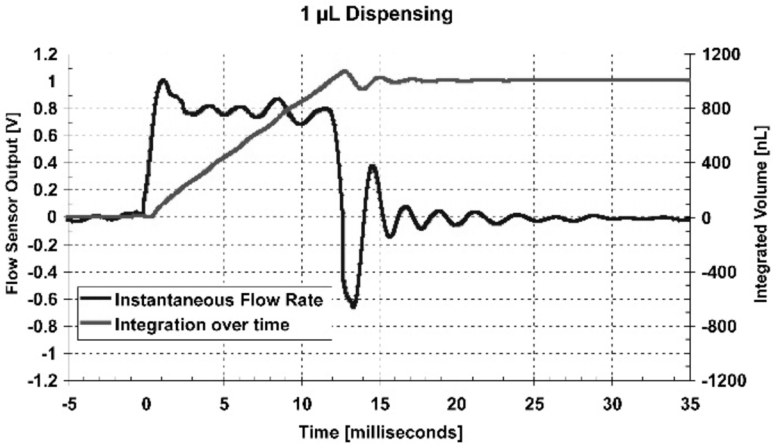

Figure 2.8 Typical signal of a seyonic flow sensor and signal processing by signal integration over time [43].

An alternative non-invasive process control method applying flow sensors, which means that the sensor does not get in contact with the sample liquid have been reported. One specific method is based on the measurement of the gasflow into and out of a liquid reservoir, balancing the occuring pressure deviation after a dispensing procedure. Highly sensitive thermal flow sensors, which are developed at the Hahn-Schickard-Gesellschaft, Institut für Mikro- und Informationstechnik (HSG-IMIT) [45, 46] were applied, which allow for the quantitative measurement of small airflows by a calorimetric measurement principle. A sketch of the applied measurement setup, to realise the proof of principle of the described technique is given in figure 2.9.

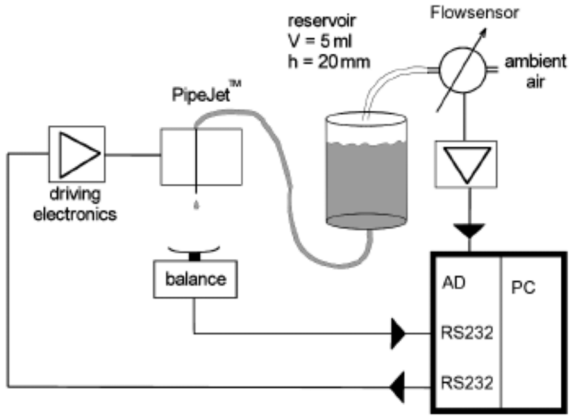

Figure 2.9 Principle sketch of the experimental setup for the non-invasive flow measurement technique [47].

A droplet which is dispensed out of a dispenser nozzle reduces the liquid level in the reservoir by the ejected volume. This entails a pressure drop in the reservoir, which has to be balanced by an airflow through the reservoirs inlet. Connecting the said flow sensor to this inlet enables the measurement of the balancing air flow. Applying an integral to the calibrated flow sensor signal enables to calculate the ejected liquid volume. Figure 2.10 shows the quantitative evaluation results in comparison to a gravimetric measurement presented in [47].

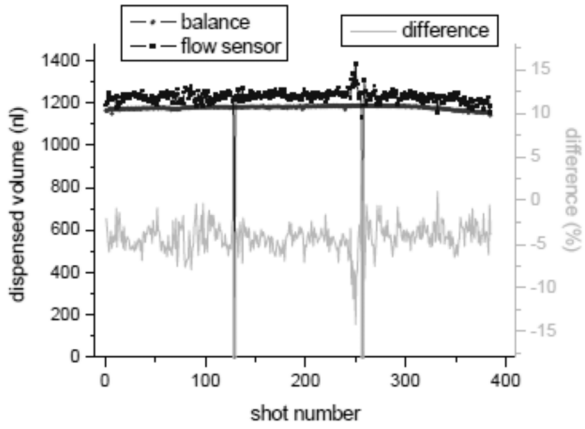

Figure 2.10 Quantitative results achieved by the flow sensor application [47].

To finalize the introduction of the state-of-the-art of droplet detection techniques can be summarized that several drawback regarding integratability and real time data acquisition are still not solved. The application of gravimetrically based weighing procedures provide the required accuracy but implies the loss of the measured liquid. Also the complex measurement setup does not allow the use of higly precise balances for online process control at industrial applications. The application of stroboscopic cameras is a feasible but valuable alternative. The high volume errors, indirect measurement procedures and big installation size are considerable drawbacks for the use of this technique. The application of fluorometry requires a premix of the sample liquid with fluorescent pigments followed by a calibration experiment. The readout by an external plate reader and the complex handling steps preclude this method from the repertoire of online process control systems. The principle of the nozzle integrated sensor seems to provide a smart measurement alternative. But this technique still requires contact to liquid and is not experimentally characterised yet. Also the described optical approach is an interesting method for droplet detection, unfortunately without of experimental proof of principle so far. Thermal flow sensors offer the

possibility of smart system integration and contactless, real-time measurement. However, the high sensitivity to environmental influence is a considerable drawback for the application for single droplet detection in the nano liter range.

Chapter 3
Fundamentals

The following section provides the theoretical background to understand the applied methods for the development of the optical and capacitive droplet measurement techniques. Beside the fundamentals of geometrical optics and electrostatic theory this section introduces the basic equations of computational fluid dynamic simulation, which is applied to study the physics of the capacitive droplet sensor in chapter 6, as well as the basic dimensionless numbers defining a droplet ejection process.

3.1 Geometrical optics

The optical droplet detection method relies on the fundamental characteristics of a light beam influenced by a particle. The particles in case of this work are droplets in the nanoliter range, which corresponds to droplet diameters $d > 120$ µm, thus the minimum droplet size is in the order of factor 1000 bigger than the wave length of the measurement light beam. Therefore, the theory of geometrical optics holds for this topic [48]. For smaller sized particles with dimensions smaller or equal to the wavelength of the measurement light beam, different theories would hold (Mie scattering or Rayleigh scattering).

3.1.1 Reflection

One of the optical effects, caused by a droplet subjected to a light beam, is the reflection of light at the interface of a droplet, which contributes to the signal generation by the change of the measurement light beam's intensity [49]. This effect is based on the law of reflection which claims that the angle of a reflected ray equals the angle of incidence ($\theta = \theta'$) as well that the incident ray, the normal and the reflected ray occur in the same plane (plane of incidence), see figure 3.1.

3.1.2 Snell's law - Refraction

A further optical effect contributing to the measurement principle is the refraction of light at the interface to a certain medium. Figure 3.1 illustrates the refraction of a ray at a boundary layer of air to water. The ray gets partly reflected at the surface like explained in chapter 3.1.1, whereas the remaining part of the ray permeates the second medium. Like depicted in figure 3.1, the ray gets refracted into the direction to the surfaces normal, defined by the ratio of the speed of light, transmitting the different media:

$$n = \frac{\text{speed of light in vacuum}}{\text{speed of light in media}} = \frac{c}{v} \tag{3.1}$$

Snell's law relates the angle of refraction to the index of refraction, respectively the specific speed of light in the medium.

$$n_1 \cdot \sin(\theta_1) = n_2 \cdot \sin(\theta_2) \tag{3.2}$$

Figure 3.1 shows a ray that radiates from a certain medium into a different medium with a higher index of refraction n_2. Therefore, the ray is bent towards the normal according to Snell's law. Light rays which impinge on a surface of a medium perpendicularly are not bent. A further phenomenon, which is described by Snell's law, is the total internal reflection of light, which occurs for angles of incident light rays greater than the critical angle θ_c. According to Snell's law, the critical angle is calculated as follows [49]:

$$\theta_c = \operatorname{asin}\left(\frac{n_2}{n_1}\right) \tag{3.3}$$

The value of the reflected light intensity is given by the reflection coefficient R, which can be calculated by the Fresnel equation.

3.1.3 Fresnel equation

The Fresnel equation describes the power of the reflected or refracted light at an interface between two media of different indices of refraction (n_1; n_2) related to the angle of incidence. The reflection coefficient depends on the polarisation of the incident light ray.

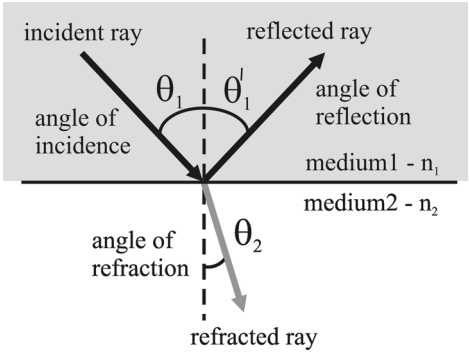

Figure 3.1 Sketch regarding to reflection and refraction

Thus, the calculation of the reflection coefficient for two different polarisation orientations, s-polarisation (perpendicular to the plane of incidence) or p-polarisation (polarised in the plane of incidence) R_s and R_p can be written as:

s-polarisation:

$$R_s = \left(\frac{n_1 \cos\theta_1 - n_2 \cos\theta_2}{n_1 \cos\theta_1 + n_2 \cos\theta_2} \right)^2 \tag{3.4}$$

p-polarisation:

$$R_p = \left(\frac{n_1 \cos\theta_2 - n_2 \cos\theta_1}{n_1 \cos\theta_2 + n_2 \cos\theta_1} \right)^2 \tag{3.5}$$

For non-polarised incident light, the coefficient of reflection is considered as:

$$R = \frac{R_s + R_p}{2} \tag{3.6}$$

3.1.4 Beer Lambert law - Absorbtion

Absorption is the phenomena of loss of intensity while an electro magnetic wave transmits a certain medium. This is described by the Beer- Lambert law, which gives the relationship between the absorbance and the concentration of a specific absorber of an electromagnetic wave. The Beer- Lambert law can generally be written as:

$$A_b = \alpha_\lambda \cdot l \cdot c \tag{3.7}$$

where A_b is the absorbance, α_λ the absorbance coefficient (dependent on the wavelength), l is the path length of transition and c is the concentration of the absorbent material. Commonly used for optical applications is the transmittance T as measure for the intensity loss. In terms of liquid absorbation is usually written as:

$$T = \frac{I}{I_0} = 10^{-\alpha_\lambda l} \tag{3.8}$$

where I is the intensity of light after the transition through the absorbent material, I_0 is the initial intensity of the emitted light, l is the path length and α is absorption coefficient.

The relation of absorbance A_b and transmittance T is defined by [49]:

$$A_b = -\log_{10}(T) = -\log_{10}\left(\frac{I}{I_0}\right) \tag{3.9}$$

3.2 Electrostatic theory

One of the presented sensor approaches in this work is based on a capacitive measurement method, which enables to measure a dispensed droplet during its flight in an electrical, contactless manner. For more details on the method see chapter 6. For the better understanding of the characteristics of the presented approach the necessary theoretical fundamentals are briefly reviewed in the following.

3.2.1 Maxwell equation

The existence and the characteristics of electromagnetic waves were first consistently explained by J. C. Maxwell in 1865. He established the mathematical formulation in a set of four fundamental equations, known as the Maxwell's equations, to describe the relation of the field sizes electric field $\vec{E}$, electric flux density $\vec{D}$, magnetic field $\vec{H}$ and the magnetic flux density $\vec{B}$. In relation to this work Maxwell's first equation will be presented only. This equation describes the basic principle of the presented capacitive droplet detection method. Simply speaking, it states that a change of the electric flux density $\vec{D}$ over time t entails a so called displacement current in an electric field. Since electric fields don't support the flux of electric currents, the displacement currents do not consist of charge carriers, they are conceptional defined entities by Maxwell to explain the characteristics in an alterable electric field. The electric current in terms of mobile charge carriers appears out side the field and is equal to the displacement current, thus Maxwell's first equation can be described by [50]:

$$i = \oint H ds = A \cdot \frac{dD}{dt} \tag{3.10}$$

For an easy understanding of the properties of the measurement procedure, the fundamental of the electric field in particular, the phrase 'capacitance' and other electrostatic phenomena will be given following.

3.2.2 Electric field

It is generally known that charged bodies exert forces onto each other which increase for small distances. Either they attract one another or they repel. This

effect depends on the electric charge of the bodies, thus two equally charged bodies will repell, whereas two opposite charged bodies will attract each other. A positive charged element comprehends a lack of electrons, thus more positive protons are embedded in the surface of the element. Negative charged elements consist of electrons, thus the average surface charge is negative. As general description the electric field surrounding an element depends on the charge of the element and is indicated by so called field lines. This lines are drawn from the positive pole in direction to the negative pole, whereas the direction is marked by arrowheads, see figure 3.2. This direction is an arbitrary definition but commonly used. It indicates for the direction of the electric force exerted on a positive test charge placed at any point in an electric field. Field lines do always appear orthogonal to a element's surface. A force, indicated by a field line, of a different angle to the surface than 90° can be split into two dimensions, the normal and the tangential force. Due to the fact that electrons are highly mobile and follow the tangential component on a conductors surface, they always move until the electric equilibration is reached, thus the orthogonal position of the field line is mandatory on conductive surfaces. The definition of the electric field strength $\vec{E}$ is the electrostatic force $\vec{F}$ per charge unit Q and oriented radially outward from a positive charge. It is defined as the proportionality constant between charge Q and force $\vec{F}$ [51]:

$$\vec{E} = \frac{\vec{F}}{Q} \tag{3.11}$$

where $\vec{F}$ is the electrostatic force, given by Coulomb's law and Q the electric charge. The SI unit for electric field strength $\vec{E}$ is derived as follows:

$$[E] = \frac{N}{C} = \frac{N \cdot m}{A \cdot s \cdot m} = \frac{W \cdot s}{A \cdot s \cdot m} = \frac{V \cdot A \cdot s}{A \cdot s \cdot m} = \frac{V}{m} \tag{3.12}$$

The field strength is indicated by the density of the field lines, thus a high accumulation of lines goes along with a high field strength. Thereby, the electric potential U can be introduced, which describes the required work W to move a charged element Q in a static electric field for a certain distance $\vec{s}$ and is defined to be:

$$U = \frac{W}{Q} = \frac{\vec{F} \cdot \vec{s}}{Q} \tag{3.13}$$

Two plane conductor plates of different charge and equal size create a so called plane parallel plate capacitor.

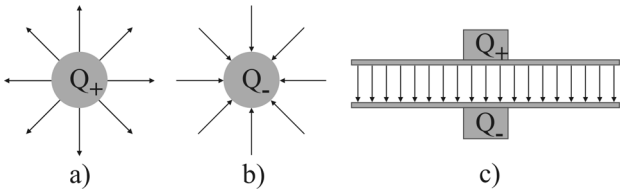

Figure 3.2 Electric field; a) positive charge; b) negative charge; c) plate capacitor

The electric field within the parallel plates distributes homogeneously which is indicated by parallel field lines, see figure 3.2, thus the field strength, implementing an electric force which acts on an imaginary test charge Q introduced in the electric field is constant at each point in the field. Therefore, we can obtain, by considering the work $W = F \cdot s = Q \cdot U$, the numerical equation for the electric field strength in a homogeneous field:

$$\vec{E} = \frac{U}{\vec{s}} \tag{3.14}$$

3.2.3 Capacity

Capacitance is a measure for the amount of electrical charge which can be stored by a capacitor for a given electrical potential. It is defined as the ratio of the charge Q of one sign (+ or -) to the voltage potential U between the capacitor electrodes.

$$C = \frac{Q}{U} \tag{3.15}$$

The charge Q and the potential U are always given in positive quantities, unaffected of the charge sign, hence a capacitance can not be negative! The SI unit for the capacitance [F] (Farad) is given by C/V and named in honor of Michael Farady who introduced the concept of the electric field. The derivation for the capacitance of a plane parallel plate capacitor, assuming a homogeneous electric field, in terms of geometrical dimensions of the electrode arrangement can be done by the combination of a set of equations like given in the following. The electric flux density is described by:

$$\vec{D} = \varepsilon_0 \cdot \vec{E} \tag{3.16}$$

the electric flux by:

$$\Psi = Q = \vec{D} \cdot A \tag{3.17}$$

and the electric field strength by equation 3.14. This leads to the following equation giving the charge Q, based on the dimensions of the capacitors electrode arrangement:

$$Q = \frac{\varepsilon_0 \cdot A}{s} \cdot U \tag{3.18}$$

where ε_0 is the permittivity of free space $(\varepsilon_0 \approx 8,854 \cdot 10^{-12} \cdot C/(V \cdot m))$, A the area of the conductor plates, s the perpendicular distance of the plates and U the voltage potential between the conductor plates. Finally, the basic equation to calculate the capacitance of a plane parallel plate capacitor is derived by the combination of eq. 3.15 and eq. 3.18 to [49,51]:

$$C = \varepsilon_0 \cdot \frac{A}{s} \tag{3.19}$$

However, capacitance does not appear between two plane parallel conductor plates in a homogeneous manner only. Section 3.2.2 mentioned that an individual charged element entails a electric field surrounding it, thus capacitance appears in many possible shapes and field distributions. The calculations of these appearing inhomogeneous electric fields are handled by numeric simulation tools in this work, thus are not given in more detail here. The capacitance of a capacitor changes by the insertion of a dielectric material into the space between the electrodes. The effect of an inserted dielectric material to the electrical characteristics of the capacitor is explained in the following section 3.2.4.

3.2.4 Dielectric materials and relative permittivity

The increase in capacitance of a plate capacitor, caused by the insertion of a dielectric material into the electric field between the electrodes, is based on the electric field E_P appearing in the inserted dielectric body. E_p depends on the material specific relative permittivity ε_r of the dielectric material, see eq. 3.21. In contrast to conductive materials, which compensate external electric fields by the mobility of the free charge carriers leading to a field free inner volume (see section 3.2.2), dielectric materials belong to the group of insulators featuring no free charge carriers. Therefore, dielectric materials are not able to compensate external fields. Rather, a field E_P occurs, which is oriented opposite to the polarity of the external field E_0. This implies a damping of the initial electric field described by:

$$E = E_0 - E_P \tag{3.20}$$

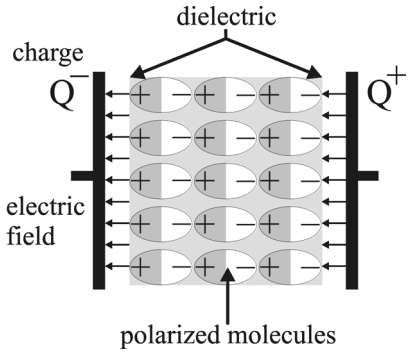

Figure 3.3 Principle of dipole orientation exposed to an external electric field

However, the field strength of E_P depends on the polarisation characteristics (susceptibility χ) of the dielectric material, which first has to be categorized by material specifications into the following three different groups:

i.) Dielectric materials

Materials belonging to the group of dielectric material consist basically of non-polar molecules. The exposure of these materials to an external electric field induces a so called displacement polarisation, where the negative charged electrons follow the electric field orientation and accumulate along the field lines. Therefore, a dipole occurs by the separation of electrons and protons by the electric field. An example for typical dielectric materials, inclusive the corresponding relative permittivity are listed in the following table:

Table 3.1 Dielectric materials incl. corresponding relative permittivity

material	relative permittivity ε_r
air	1.000549
oxygen	1.00049
nitrogen	1.00053
oil	2-4

For dielectric materials, the relative permittivity ε_r does not change with temperature, thus it is temperature independent.

ii.) Paraelectric materials

In contrast to dielectric materials, the materials of the group of paraelectrics consist initially of dipole molecules. Such materials are usually fluids or solid

bodies. Dipole molecules get inversely oriented to the polarity of an applied external electric field along the direction of the field lines. This effect is called orientation polarisation and depicted in figure 3.3. The relative permittivity of materials grouped here, is independent on the field strength but inverse proportional to the temperature T and depends often on the applied field frequency. Materials of these category are for example water featuring a permittivity of $\varepsilon_r = 81$ for frequencies < GHz or ethanol ($\varepsilon_r = 25$) at T = 20 °C.

iii.) Ferroelectric materials

A third group of materials is given by the ferroelectric materials. The relative permittivity of ferroelectric materials is increasingly higher than these of the previously given categories and can reach values up to $\varepsilon_r = 10^4$. Above the curie-temperature ferroelectric materials develop dipoles which get polarised by the exposure to an electric field. The speciality of ferroelectric materials is that they keep the dipole oriented structure after removal of the causative electric field. Ferroelectric materials are e.g. bariumtitanate $\varepsilon_r = 1250$ - 10000 (20°C - 120°C) or titanium dioxide $\varepsilon_r = 86 – 173$ [51]. The material categorisation shows that each material features a specific relative permittivity ε_r regarding the molecule structure of the material. From eq. 3.20 it follows that the initial flux density of an electric field D_0 increases by the insertion of a dielectric body by the factor ε_r to the flux density D. Therefore, the relative permittivity is given by the ratio of D_0 and D at a constant field strength E:

$$\varepsilon_r = \frac{D}{D_0} \tag{3.21}$$

This implies that the presence of a dielectric material entails a change of the analytical equations treating capacitance by the multiplication of the material defined factor ε_r . The basic equation enabling the calculation of the capacitance of an plane parallel plate capacitor by geometrical values eq. (3.16) has to be extended by the factor ε_r to:

$$C = \varepsilon_0 \cdot \varepsilon_r \cdot \frac{A}{s} \tag{3.22}$$

In contrast to the presented dielectric materials, conductive elements consist of free charge carriers, thus the expression ’permittivity’ or ’dielectric’ does not hold for metals and other conductive elements. Since the free charge carriers are able to follow the electric field like described above, the permittivity reaches a theoretical value of $\varepsilon_r \sim \infty$.

3.2.5 Electric influence

Basically, the electric influence describes the separation of free charge in a conductive material exposed to an external electric field. The free charge carriers in the material follow the potential of the external field, thus negative and positive charge carriers become separated on the opposite surfaces of the material like described above. Therefore, the external field becomes compensated, which results in a field free inner volume. This effect can be exemplified in a simple experiment, like shown in figure 3.4. The insertion of two connected conductive plates into an external electric field leads to the mentioned charge separation on the inserted plates (figure 3.4 a) - b)). By increasing the distance in between the plates (figure 3.4 c)), a field-free space appears by the compensation of the external field by the mobile charge carriers. After the removal of the plates from the electric field, a potential can be measured between the plates caused by the still separated charge carriers, which cannot be distributed like initially due to the disconnection of the plates [51]. This effect of charge separation in conductive material caused by the exposure to an external electric field is called electric influence. Compared to the behavior of dielectric (non-conductive) material by the exposure to an electric field, see above, it can be seen, that the term relative permittivity ε_r does not hold in case of conductive material. It more or less changes the geometrical conditions of the capacitor electrode arrangement, thus the change of the equivalent circuit leads to the change in capacitance.

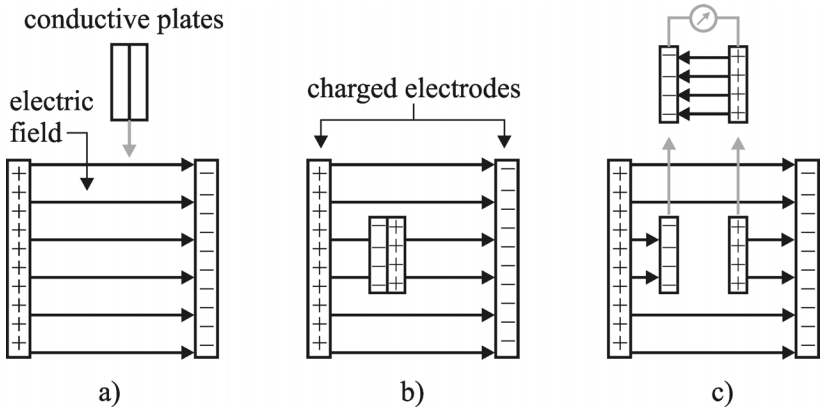

Figure 3.4 Experimental explanation of the effect of electric influence by the insertion of two conductive plates into an electric field.

3.3 Computational Fluid Dynamics (CFD)

One of the focussed sensor concepts in this work is the non-contact detection of dispensed droplets by the change in capacitance of an open plate capacitor. The investigation of the physics at the measurement electrode while a droplet passes the electric field of the capacitor is supported by the application of a CFD simulation tool. Therefore, the basics of the numerical solution provided by CFD simulation are given in the following.

3.3.1 Hydrodynamics

The simulation of hydrodynamic fluid flows using CFD is based on the iterative solution of the discretised Navier Stokes equation (NSE) [52]. The basic set of equations to be calculated using a CFD code consists of the basic physical conservation principles of mass, momentum and energy, which are given like follows. The first equation, the continuity equation, is derived from the mass conservation within infinitesimal fluidic elements by the application of the Gauß- Theorem and given by:

$$\frac{\partial \rho}{\partial t} = -\nabla \cdot \rho v \tag{3.23}$$

which describes that the variation of the fluids density over time is equal to the negative rate of the volume change of the considered element. The second equation is derived from Newton's second law *(F = m·a)*, thus gives the momentum conservation equation.

$$\frac{\partial}{\partial t}\rho u_i + \nabla(\rho u_i v) = -\nabla p + \nabla(\mu \nabla v) + S_M \tag{3.24}$$

Here, the time derivative of the momentum (left → rate of momentum change + force transfer to environment) is equally to the momentum change caused by the flow characteristics like pressure gradient, the viscous shear force and an additional source term like e.g. gravity, surface tension, electrokinetic effects etc. (right → - pressure gradient + viscous loss + source terms). The third equation, the energy conservation equation is based on the first law of thermodynamics.

$$\frac{\partial(\rho i)}{\partial t} + \nabla \cdot (\rho i v) = -\nabla p v + \nabla(k \nabla T) + \Phi + S_i \tag{3.25}$$

It gives the rate of internal energy change to the energy change caused by the liquid flow, which depends on volume changes, diffusive energy transport by

e.g. heat conduction, a dissipation function and source terms like gravity, surface tension, electrokinetic effects etc. For more detailed information about the simulation of fluid dynamics using CFD see [52].

3.3.2 Numerical methods

The simulation of a free flying, dispensed droplet, which is applied to investigate the charge alternation on the measurement electrode, is based on the application of the finite volume method (FVM). The FVM is a numerical method for the solution of partial differential equations that calculates the values of the conserved variables across a considered volume. This so called 'control volume' is defined by the discretisation using a computational mesh. In case of the calculation of fluid flows applied at CFD simulations, the FVM is based on the passive transport equation, derived from the presented conservation principles, given for a scalar quantity ϕ:

$$\frac{\partial(\rho\phi)}{\partial t} + \nabla \cdot (\rho\phi v) = \nabla \cdot (\Gamma \nabla\phi) + S_\phi \tag{3.26}$$

local term		**convective term**		**diffusion term**		**source term**
rate of increase of ϕ of fluid element	+	net rate of flow of ϕ out of fluid element	=	rate of increase of ϕ due to diffusion	+	rate of increase of ϕ due to sources

In case of the NSE, the quantity ϕ is given by the velocity vector $\vec{v}$. A further method, required for the multi-disciplinary simulation of the droplet measurement procedure, is the volume of fluid method (VOF). The VOF method enables the simulation of two phase flows of immiscible fluids (here water and air), which is applied for the simulation of the free flying droplet including the droplet ejection process. This implies the demand for the introduction of an additional field variable, the volume fraction *f*, describing the fluid flow. The volume fraction *f* determines the phase distribution of the two phase flow by a value between 0 and 1 for each individual control volume. A full liquid phase is defined by $f = 1$ whereas the volume fraction for the gas phase (air) is $f = 0$. Since this method determines the phase distribution in terms of the *f* value only, no discrete interfaces between the phases are described. *f* values between 0 and 1 give the ratio of the amount of the two phases *x* in the currently calculated element, thus the mean density, viscosity, etc. x_{mean} are considered, which are averaged according the corresponding *f* value like follows:

$$x_{mean} = (1 - f) \cdot x_{air} + f \cdot x_{water} \tag{3.27}$$

The implementation of the volume fraction f is calculated by the additionally solved passive transport equation 3.28 [53]:

$$\frac{\partial f}{\partial t} + \nabla \cdot \vec{v} f = 0 \tag{3.28}$$

However, using the f value alone does not implement the consideration of the surface tension of the liquid which is required to reflect realistic conditions. Therefore, an interface reconstruction method has to be applied to determine the exact location and shape of the interface between the fluids. Various methods are available featuring different accuracies. For this work the Piecewise Linear Interface Construction (PLIC) of 2nd order was applied. The PLIC scheme holds the assumption that the interface between the fluids is planar and able to take any orientation within the considered control volume [54; 55]. Strictly speaking, it forms the shape of an arbitrary polygonal surface. The orientation of this interface is given by its normal, pointing from one phase to the other. Parallel to the normal, there is a gradient vector of f, which is determined by the local distribution of f in a set of cells, including the considered control volume and its neighbouring cells. The algorithm further calculates the volume of the cell fraction, delimited by the interface, considering the whole control volume size proportioned by the f factor. The PLIC scheme implies a unique interface normal for each individual control volume, which is used to reconstruct the entire surface of the fluid interface. Regarding to the reconstructed interface curvature r it is possible to implement surface tension forces [56], which are based on the pressure difference Δp between the phases and the surface tension σ, given by the Young-Laplace equation:

$$\Delta p = \frac{2 \cdot \sigma}{r} \tag{3.29}$$

3.3.3 Electrostatic formulas

In addition to the fluid dynamics also the electrical field inside the capacitive transducer is modeled by the application of the electric module, provided by the CFD ACE+ tool used for this task [57]. This module enables the calculation of several different electrical effects on basis of the Maxwell

equations [58]. For the investigation of the considered problem, it is sufficient to consider the electrodynamics effects in the electrostatic limit only. The reason for this is that the occurring currents are very small and they occur on a large time scale only compared to the inductivities involved. Thus, electromagnetic effects can be neglected for the description of the charge redistribution on the capacitor electrodes. The electrostatic modelling is based on Gauss' Law which governs the fundamental basics of the topic. It states that the electric flux passing through a closed surface is equal to the charge enclosed by that surface, which can be written in differential form like follows:

$$\nabla \cdot D = q \tag{3.30}$$

where D is the electric displacement flux density, given in (C/m^2) and q is the volume charge density given in (C/m^3). The relation of the electric flux density D and the electric field E is given by eq (3.13). The electric field vector E is irrotational for electrostatic considerations ($\nabla \times E = 0$), thus a scalar electric potential ψ can be defined by:

$$E = -\nabla\psi \tag{3.31}$$

The insertion of equation 3.16 and equation 3.31 in equation 3.30 gives the Poisson's equation for the electrostatic potential:

$$\nabla(\varepsilon_r \varepsilon_0 \nabla\psi) = -q \tag{3.32}$$

The calculation of the total charge on an electrode by the electric module in a discrete manner is implemented by:

$$Q_{\psi_0} = \sum_{i=0}^{face\psi_0} \varepsilon_i E_{ni} A_i \tag{3.33}$$

where $Q_{\psi 0}$ is the sum of charge at each face at a fixed potential ψ_0, $\varepsilon_\iota E_{ni}$ is the electric potential at the boundary and A_i the area of the face [58]. The considered simulation model solves equation 3.33 for each individual control volume by the finite volume method additionally. This implements the calculation of the charge on the capacitor electrodes to the simulation model.

3.4 Droplet ejection

A dispensing process, especially the tear off process of liquid to form single free flying droplets depend on several parameters, which basically can be described by a set of dimensionless numbers. This numbers are used to define the boundaries for the simulation of a droplet dispensing process and are briefly defined in the following.

3.4.1 Weber number

The Weber number *We* is one of the set of dimensionless numbers mentioned above. It is defined by the ratio of the kinetic energy E_{kin} and the surface energy E_{sur} of a fluid. The Weber number is a characteristic number which is used to describe the tear off process of a droplet from a liquid column and calculated by equation 3.34 [59].

$$We \sim \frac{E_{kin}}{E_{sur}} = \frac{(1/2) \cdot m \cdot v^2}{A_T \cdot \sigma} = \frac{1}{12} \cdot \frac{\rho \cdot D \cdot v^2}{\sigma} \tag{3.34}$$

$$\Rightarrow We = \frac{\rho \cdot D \cdot v^2}{\sigma} \tag{3.35}$$

where D is a characteristic length, in this case the nozzle diameter, σ the surface tension of the liquid and A_T the surface of the droplet. In case of droplet ejection, D corresponds to the nozzle diameter whereas v is the velocity of the droplet at the nozzle. For Weber numbers of 12 and above a droplet tear of is feasible.

3.4.2 Reynolds number

A further important dimensionless number, which considers the viscosity of fluids regarding their flow conditions is the Reynolds number *Re*. It gives the ratio of the inertial kinetic energy E_{kin} to the friction energy E_{fric} of a fluid, thus it is consulted for the characterisation of certain flow regimes [60]. The Reynolds number is given as:

$$Re \sim \frac{E_{kin}}{E_{fric}} = \frac{(1/2) \cdot m \cdot v^2}{2 \cdot \eta \cdot v \cdot (V/l)} = \frac{1}{4} \cdot \frac{\rho \cdot v \cdot l}{\eta} \tag{3.36}$$

$$\Rightarrow Re = \frac{\rho \cdot v \cdot l}{\eta} \tag{3.37}$$

where m is the mass, v the velocity, η the dynamic viscosity, V the volume, l

the characteristic length and ρ the density of the fluid.
The Reynolds number enables the classification of flow into three different regimes according to their rheology:

- creeping flow ($Re < 1$)
- intermediate laminar flow ($1 < Re < 2300$)
- turbulent flow ($Re > 2300$)

A Reynolds number of $Re = 2300$ is referred to be the 'critical Reynolds number', which gives the point of inflexion from laminar flow to turbulent flow.

3.4.3 Ohnesorge number

Typically, a droplet ejection process depends on the rheology of the handled liquid, thus the introduced Weber number does hold to describe a droplet ejection process for liquids with low viscosity ($\eta < 10$ mPas) only. Handling liquids featuring higher viscosity, require the consideration of a viscous term, given by the Reynolds number. Therefore, the Ohnesorge number On has to be introduced, which combines the Weber number and the Reynolds number by their ratio:

$$On = \frac{\sqrt{We}}{Re} = \frac{E_{fric}}{\sqrt{E_{kin} \cdot E_{sur}}} = \frac{\eta}{\sqrt{\rho \cdot D \cdot \sigma}} \tag{3.38}$$

The implementation of the Ohnesorge number enables the definition of the critical Weber number We_{crit}, which allows for the handling of high viscous liquids ($\eta > 10$ mPas) regarding droplet tear off behavior [61].

$$We_{crit} = 12 \cdot (1 + 1,077 \cdot On^{1,6}) \tag{3.39}$$

Chapter 4
Dispensing Technology - PipeJet™

The PipeJet™ dispenser is a non-contact, drop-on-demand dispensing system, featuring a variety of adjustable driving parameters to adapt the droplet generation process to a wide range of liquid types. On this note, the droplet volume as well as the droplets velocity can be adjusted by the piezoelectric actuation mechanism [62, 63]. Regarding the fact, that the PipeJet™ technology is used for all experiments throughout this work solely, the following sections in this chapter give a detailed description of the PipeJet™ dispensing process and further details about the current status of the technology.

4.1 Droplet ejection principle

The PipeJet™ dispensing principle is based on direct volume displacement, originating from a fast compression of the dispenser's inner volume. The inner volume as well as the nozzle is defined by an elastic polymer tube, the 'pipe', which is the principal component of the dispensing system.

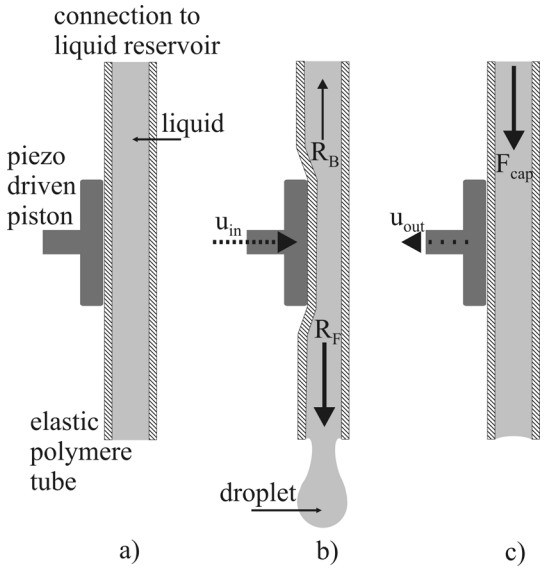

Figure 4.1 Working principle of the PipeJet™ technology. a) initial status - liquid filled 'pipe' and piston on defined initial position; b) reduction of the dosage chamber volume by the piston movement; c) refilling of the pipe by capillary forces

A complete PipeJet™ dispensing cycle is illustrated by figure 4.1 and will be given in detail in the following. In the first state, the pipe is connected to the sample liquid reservoir and filled by capillary forces. The liquid meniscus is held at the nozzle due to capillary interaction. The initiation of a dispensing process is realised by the application of a well defined voltage pulse to a piezo stack actuator, which will be given in detail in section 4.2. This voltage pulse entails a precise extension of the piezo length with a well defined velocity. The fast extension is transferred to the dispensing piston, which squeezes the liquid filled elastic polymer tube, thus causes the reduction of the inner volume of the pipe, see figure 4.1b). This volume reduction forces the surplus liquid to move in direction to the nozzle as well as in direction to the liquid reservoir. Due to the ratio of the fluidic resistance from inlet to outlet ($R_B \gg R_F$) the major part of the displaced liquid is released out of the nozzle. Terminatory, the piezo actuator gets retracted to its initial length, defined by the falling slope of the voltage pulse. Additionally to the retraction, the piston is tracked back by spring forces to its initial position. Thereby, the inner volume of the dosage chamber extends to its initial volume, which implies the refilling of the polymer tube by capillary forces F_{cap}. More details to the PipeJet™ technology can be taken from [63]. A remarkable feature, provided by the PipeJet™ technology is the adjustability of the droplet characteristics. Based on the variable piston movement velocity (downstroke) and extension (stroke) by the adaption of the actuation voltage pulse, the transferred energy to the liquid can be adjusted. This enables the alternation of the Weber number, thus the final droplet size, shape and velocity. Furthermore, different sized PipeJet™ dispensing tubes can be applied which predefine the adjustable volume range individually. A smaller inner diameter of the dispensing tube goes along with a smaller droplet sizes.

4.2 Electronic actuation

The required load to drive the piezo actuator is generated by the so called ’R5’ electronics [30]. The ’R5’ is designed to generate the specific signal characteristics, required for the fast piezo extension, controlled by a MSP430 [64] micro controller. A typical voltage pulse, generating the desired piezo extension behaviour is shown in figure 4.2. The amplitude of the rising slope determines the piezo extension length (stroke), defined by the supplied current. Furthermore, the angle of this slope determines the velocity of the piezo extension (downstroke velocity). The top plateau defines the hold time of the piezo in the extended position, followed by the slow decrease of the pulse, defining the piezo retraction procedure. Each of the mentioned parameters is individually adjustable, thus the piezo movement procedure can be adapted to dispense a wide range of different rheological liquids.

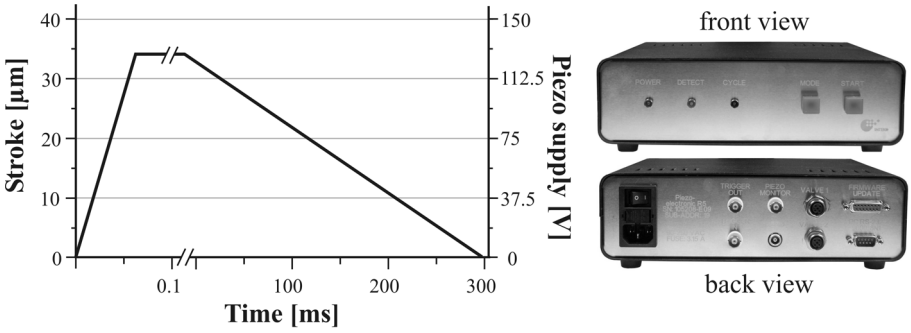

Figure 4.2 Driving pulse for the PipeJet™ dispenser actuation (a), generated by the R5 electronics from BioFluidx GmbH (b)

For more details see [63]. A further essential detail, provided by the 'R5' electronics, is the external trigger, which is synchronized with the driving pulse. It can be used e.g. to start a sample sequence of a sensor or to initiate an image recording sequence for the stroboscopic imaging, like applied for the later experiments. Therefore, a time correlation of droplet images to sensor signals can be realised.

4.3 PipeJet™ family

The complete PipeJet™ family consists of three different dispenser modules (P18, P9, P4.5), all based on the PipeJet^{TM} dispensing technology. Illustration 4.3 shows an image of the three different commercially available modules [30]. For the experimental characterisations throughout this work, only the P9 and the P18 modules were used. The modules differ in their geometry as well as in the adjustable range of droplet volume. The P18 module is the high performance dispenser of the family, featuring a high precision piezo stack actuator embedded in a solid aluminium housing. Furthermore, this actuator can be used as multiple channel dispenser with up to 5 dispenser tubes in parallel at a pitch of p = 2.25 mm. The corpus width of 18mm leads to a nozzle to nozzle pitch of 18 mm at multiple module array applications using a single tube. The P9 module, also fabricated in an aluminium housing, features a 9 mm width housing, thus a 9 mm nozzle to nozzle pitch at multiple module array applications can be realised. The adjustability of droplet characteristics is comparable to the P18 module.

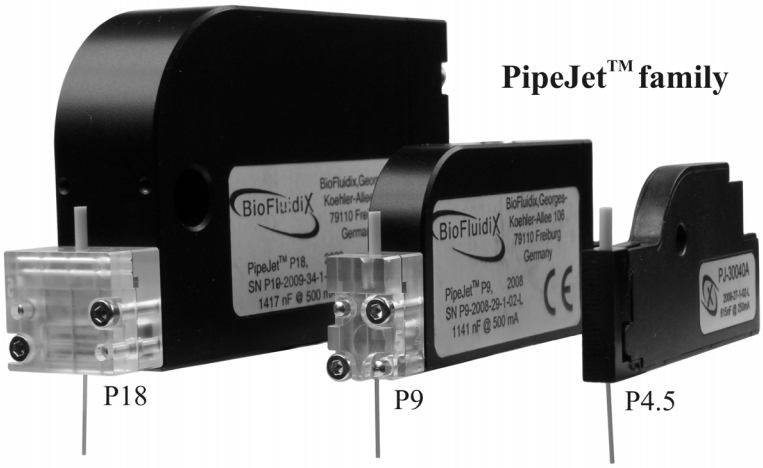

Figure 4.3 PipeJet™ family. Illustration of all commercial available modules, PipeJet^{TM} P18, PipeJet^{TM} P9; and PipeJet^{TM} P4.5.

The P4.5 is designed as constant volume dispenser. It is made fully of plastics applying an injection molding process. The small width of 4.5 mm allows for a nozzle to nozzle pitch of 4.5 mm at module array applications. The most important PipeJet^{TM} module specifications are summarized in the following table.

Table 4.1 Specifications of the different available PipeJet^{TM} modules

Parameter	P18	P9	P4.5 / vario
volume range [nl]	5 - 100	5 - 70	12 nl fixed
piezo extension [µm]	40	36	18
number of tubes	max. 5	1	1
pitch [mm]	18	9	4.5
max. frequency* [Hz]	500	500	1000

* max. frequency which can be produced by the piezo actuator, most liquids are dispensable at much lower frequencies only.

Chapter 5
Optical Droplet Detection

An early investigated principle to record the size distribution of rain drops was reported by Mason and Ramanadham in 1953 [22]. The basic principle of Mason's measurement method to determine the size of rain drops is based on the interaction of the liquid droplets with an emitted light beam. Exploiting this already established method for the design of a novel sensor system, enabling the detection of free flying nanoliter droplets is a feasible procedure to succeed. The following section discusses the development and characterisation of an optical process control system based on Masons basic principle. It enables to observe the properties of liquid droplets without contact to the medium after the droplets' ejection out of a dispenser nozzle. Based on this system, a process could be established to classify the dispensing process of a non- contact dispensing system in a semi-quantitative manner.

5.1 Basic principle

The presented optical droplet detection method is based on the interaction of a free flying droplet with an emitted light beam of a certain frequency in the infra red regime. The light intensity of the emitted measurement beam gets affected by the media of a passing droplet according to the theory of geometrical optics, see chapter 3.1. This theory holds for the present model due to the specific ratio of the measured bodies size, which scatters the light beam (here the droplet), to the wavelength of the measurement light beam. The minimum volume of the considered target measurement range, thus the smallest droplet volume which should be measured is approximately V = 1 nl.

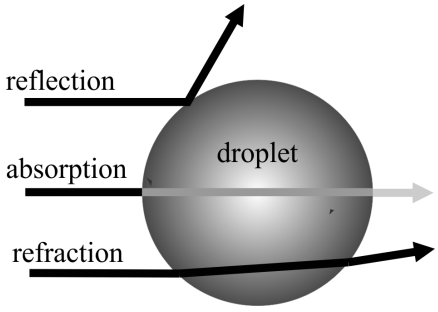

Figure 5.1 Physical interaction of light with a transparent droplet

This volume corresponds to a spheres diameter of d = 150 µm, which is approx. 100 times larger than the applied optical wavelength. An optical measurement of smaller objects featuring sizes in the range of the measurement wave length or smaller would rely on different physical theories, which are the Rayleigh- and the Mie scattering [65, 66]. For the present case, the basic geometrical optic effects can be described by refraction, reflection and absorption, see 3.1 [48].

5.2 Proof of sensor concepts

The implementation of the given requirements to an applicable sensor unit was realised by investigating different approaches by single feasibility experiments. The individual approaches are based on the different scattering effects illustrated in figure 5.1.

5.2.1 Direct light beam method - OS 1

The principle idea of the direct light beam method is to measure the decrease in light intensity caused by a droplet which passes a measurement light beam. Given by the general geometric optical effects the absorption of light is the predominant effect which has to be considered mainly. The absorption of an electromagnetic wave is based on the absorption coefficient of the absorbing medium with respect to the wave's frequency.

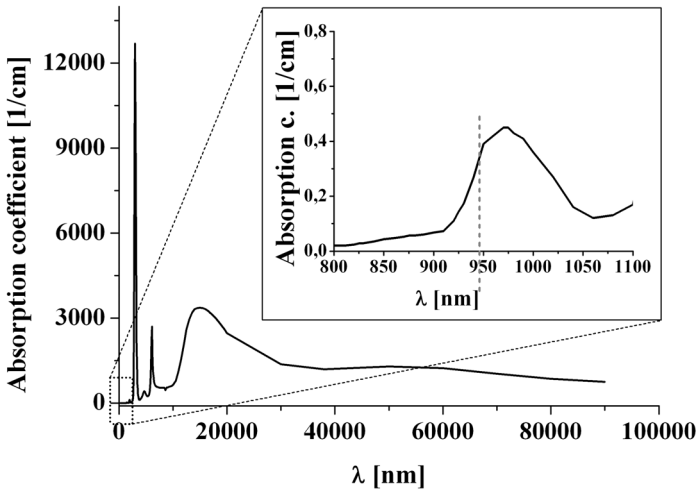

Figure 5.2 Absorption spectra of pure water, with illustration of the local maxima in the near infra red at λ = 980 nm

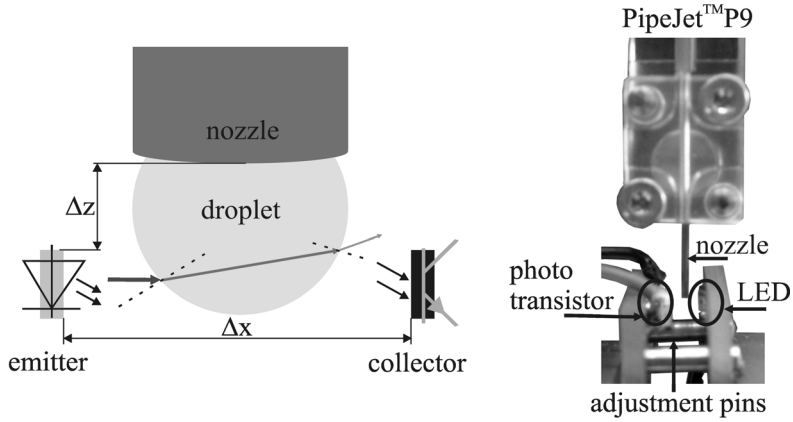

Figure 5.3 a) Principle of the direct light beam method;
b) implementation for the proof of concept

Since the most prominent liquids which commonly used in the field of life science are aqueous solutions, the wave length of the measurement light beam is adapted to the absorption spectrum of water. This exhibits a local maximum in the near infra red (IR) spectrum at $\lambda = 980$ nm, see figure 5.2. To reach a high sensitivity regarding droplet detection, light emitting elements are focussed which exhibits optical wavelengths close to this local maximum. The realisation of the direct light beam method requires the installation of the sensor components below the dispenser nozzle, such that a dispensed droplet passes the active sensor elements after its ejection. The experimental set up for the proof of concept consisted of a light emitting diode (LED) SFH 4010 from Osram [67] and the photo transistor PT 100 MF0MP1 from Sharp [68], installed underneath a PipeJet™ - P9 dispenser [30]. These components were selected due to a comprehensive market research, which considered the wavelength and the geometry of the components as well as the angle of radiation, the influence of ambient light to the performance and the energy consumption. The components were arranged on two separate support PCB's. The direct alignment was realised by a manually adjustable setup which enabled to change the distance between the components Δx. Therefore, the optimum distance between the elements, which resulted in the highest signal change while a water droplet passed the light beam could be investigated, see figure 5.3. The perpendicular incidence of the measurement light beam to the photo sensitive element, was guaranteed by two adjustment pins, which guided the support PCB's. The distance from the dispenser nozzle to the sensor elements (Δz) was manually adjustable by a spindle drive.

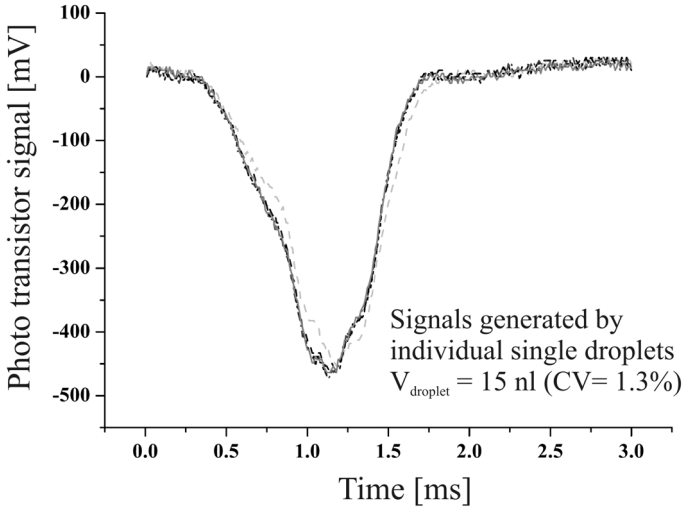

Figure 5.4 Results of proof of concept of OS 1

In a first experiment a series of single droplets with volumes of V = 15 ± 1 nl were dispensed through the sensitive area, whereas the two dimensions Δx and Δz were varied. It was found that the influence of the distance Δz to the generated signals was negligible. The dispenser nozzle could be placed very close to the sensor components ($\Delta z \rightarrow 0$), thus the distance from nozzle to substrate is defined by the sensor components geometry only. The optimum distance between the LED and the phototransistor was experimentally determined to be Δx = 2.65 mm. This gap entailed the most significant output signals, generated by the V = 15 nl droplets, see figure 5.4. The displayed graph shows five overlayed signals generated by five individual sample droplets. The negative peaks of ΔV = 500 mV in relation to the very low noise (approx. V_{noise}= 10 mV) leads to the conclusion, that the direct light beam method is a feasible approach for a successful implementation of a droplet detection sensor.

5.2.2 Surface reflection method - OS 2

The second approach is based on the detection of the reflected light from the surface of a droplet. In this setting a dispensed droplet passes the sidewise installed sensor components after its release out of the dispenser nozzle. The light emitted by the sensor LED is reflected at the surface of the passing droplet and is detected by the photosensitive element, as sketched in figure 5.5.

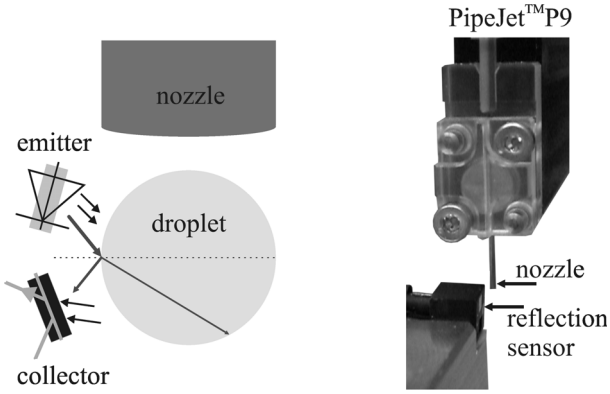

Figure 5.5 a) Principle of surface reflection; b) implementation for the proof of concepts

The major optical effect for the detection method of OS 2 is the surface reflection of light. In contrast to the previously shown approach the sensor component need to be installed on one side of the dispenser nozzle only. However, an additional distance in z-dimension to the substrate cannot be avoided if the components have to be installed underneath the dispenser. The preliminary experiments were done using a commercially available reflective sensor from Honeywell [69], which was installed below the nozzle of the PipeJet™ P9 dispenser, see figure 5.5. Several droplets of different volumes were measured with the described setup in the range from V = 1 - 50 nl. The very low signal to noise ratio (SNR < 1) implied that the surface reflection method was not investigated in more detail.

5.2.3 Inner illumination method - OS 3

The principle of the inner illumination approach is based on the detection of light, diffracted from a luminous droplet. A pending droplet gets illuminated from the inside by a tiny waveguide, which is inserted in the dispenser nozzle like sketched in figure 5.6. The part of light, which is not subjected to total reflection but diffracted in direction to the sensor contributes to the sensors output signal. A photo sensitive element mounted sidewise to the dispenser nozzle detects the diffracted light until the droplet's tear off. Therefore, the droplet generation process can be monitored by generating a positive signal peak whereas the droplet builds up at the nozzle. The extracted signal is supposed to contain information about the droplet formation process and therewith irregularities in the dispensing procedure. The realisation of this

approach was implemented by inserting a waveguide with a diameter d = 125 µm into the polymer tube of the PipeJet^{TM} dispenser to illuminate the sample liquid. Unfortunately, it was not possible to eject any droplets out of the dispenser nozzle with integrated wave guide. Also the corruption of the waveguide by the mechanical stress generated by the dispenser piston is a considerable drawback. Obviously, this led to a significant loss of light intensity and hindered a satisfying illumination of the liquid. In summary the inner illumination method has to be considered as not applicable in practice.

5.2.4 Inner reflection method - OS 4

The last investigated approach is based on the reflection of light at the inner boundary interface of a droplet, based on the law of total reflection. The measurement light will be refracted by a dispensed droplet and bent towards the photo detector. This light is supposed to generate a positive signal peak, allowing the detection of a single droplet in flight. The experimental setup to study this effect consisted of the two sensor components (SFH 4010 by Osram and PT 100 MF0P1 by Sharp) which were aligned sidewise at the orifice level of the PipeJet™ dispenser and facing towards the substrate as shown in figure 5.6 b). A big advantage of this setup would be that no space underneath the nozzle is needed for this arrangement. Relating to geometrical optics, the interaction of a light beam with a liquid droplet can be separated into three different cases; First it can enter the droplet, be reflected inside the droplet and then exit the droplet in direction of the sensor. This describes the ideal mode for this approach. However, it is also possible that the light beam gets reflected more than once at the inside of the droplet. This would lead to a further decrease of light intensity scattered in direction to the detector.

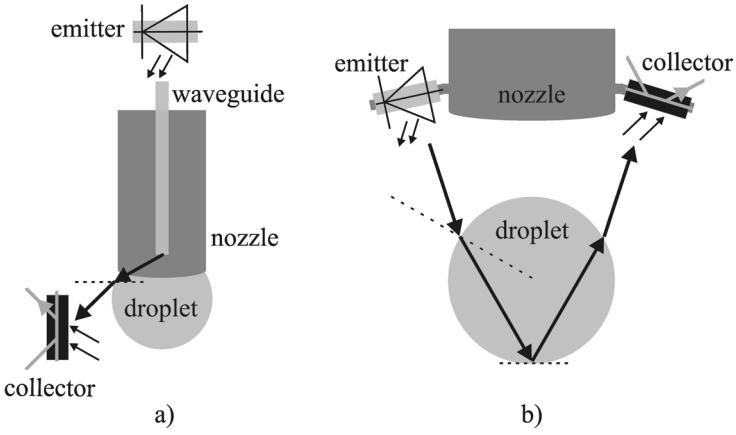

Figure 5.6 a) Principle of inner illumination; b) principle of inner reflection

Also the exit point of the beam can be different and hinder the detection of the reflected light. The third case considers total reflection inside the droplet leading to the so called 'whispering gallery mode'. Here it is impossible that the light beam exits the droplet again. This however is possible for exact spherically shaped bodies only, thus can hardly occur in dispensed droplets. In the following only the first introduced model is considered in detail because it is the most suitable for the droplet detection. However, also in this case one has to deal with a loss of intensity. This loss is caused by reflection and absorption. The chances for detecting a significant signal is generally low, but can be raised by high illumination intensity and a very sensitive detector.The main issue in this context is not the absorption. The absorption of light intensity inside the droplet can be neglected, because assuming that the light beam would cross the droplet twice, the loss of intensity I is only 2% according to equation 5.1 [70]:

$$I = I_0 \cdot e^{-A_b \cdot x} \tag{5.1}$$

With I_0 being the intensity of the entering light beam, A_b being the absorbance of the material and x the thickness of the absorbing material. The main reason for intensity loss within the droplet is given by equation 5.2 showing the balance of the transmitted part of light T and the reflected part R.

$$R + T = 1 \tag{5.2}$$

The reflected part R of the light can be calculated by Fresnel's law [71]. For this calculation a rectangular incidence of the light beam is assumed, where n_1 and n_2 are the indices of refraction for air and water with $n_1 = 1.003$ and $n_2 \sim 1.33$ at a wavelength $\lambda = 950$ nm.

$$R = \left(\frac{\frac{n_2}{n_1} - 1}{\frac{n_2}{n_1} + 1} \right)^2 \tag{5.3}$$

As depicted in figure 5.6 b) the light beam has to transmit 3 boundary layers between water and air. When the light beam hits the droplet at position 1) and enters the droplet its intensity is still 98%, since only a small part of light is getting reflected. However, the big loss of intensity occurs at point 2), where

only 2% of the incoming light is reflected. The transmission at the last boundary layer 3) is again 98%, such that in total 1.92% of the original light intensity can reach the sensor only. In theory, the intensity of the light source and the sensitivity of the photo transducer used for the experiments would not rule out such a small amount of reflected light to be detected. However, this approach did not lead to any significant experimentally detectable droplet signal, despite the fact that angle and position of the LED and photo transistor have been varied.

5.2.5 Selection of the preferred concept

The most significant and satisfying signals were achieved by the direct light beam method - OS 1. It enabled to generate significant analogue voltage signals at a high SNR. Due to this promising results and the good feasibility, this setup was chosen for further evaluation. Based on the results of the proof of concepts, all alternative approaches have to be considered as less feasible for single droplet detection.

5.3 Optimization of the direct light beam method

The development of an optical sensor unit requires the consideration of several boundary conditions. Beside the technical specifications of the used sensor components, which are the wavelength of the emitted light of the LED and the working range of the photo transistor, also geometrical factors have to be comprised. The geometrical requirements to the sensor size can be separated in the outline geometry and the geometry of the active sensor area. The outline geometry specifies the size of the sensor (length x width x height). A fundamental requirement to the final sensor size is to match the used dispenser's lateral geometry. At array applications, which means that several dispensers are stacked in a row to generate spatially well defined droplet patterns, e.g. for the production of micro arrays, the distance between two adjacent nozzles is defined by the thickness of the dispenser unit. If the sensor would be wider than the dispenser, this would lead to a non-acceptable increase in the nozzle pitch. Therefore, a maximal sensor width of $w = 9$ mm is acceptable, defined by the used PipeJet™ P9 module. Particularly the thickness of the sensor is an important parameter for most applications. The direct light beam method requires to install the sensitive components underneath the sensor nozzle to detect the dispensed droplets after their ejection out of the nozzle, which implies an additional distance defined by the sensor thickness. Experiments have shown that the sensor signals are best reproduced if the vertical distance of the sensor components to the orifice of the PipeJet™ dispenser is set to $\Delta z = 0.3$ mm. This distance is added to the maximal height of the components of $h = 1.6$ mm, leading to a satisfying

minimal distance from nozzle to substrate of 1.9 mm. The geometry of the active sensor area is defined by the space in between the sensitive components. A dispensed droplet becomes exposed to the measurement light beam while it passes this area. Obviously, this gap has to be larger than the maximal expected diameter of a single droplet. Furthermore, malfunctions in the dispensing process, like the splitting of satellites or deviations in a droplet's flight path have to be considered. The experimentally determined value is identified to be 7.5 times the maximum droplet diameter. This guarantees enough space to prevent the components from wet contamination.

5.3.1 Sensor hardware

The sensor board was fabricated by the application of standard printed circuit board technology (PCB). To guarantee an accurate geometry of the active sensor area, a forked sensor front was designed. This front consists of vertical solder pads, enabling to mount the sensor components at the inner edges of the fork, see figure 5.7a). To realize the vertical pads standard through connections (vias) were placed at the desired position at the forked front. A successive milling procedure was applied to open the vias. This enabled to use the metallized surface as vertical soldering pads. Furthermore, distance for the sensor components can be adjusted by the milling step [72]. The outline dimensions of the assembled sensor board was 8.5 x 55 x 2.6 mm, including the complete electronic analogue read out circuit and components.

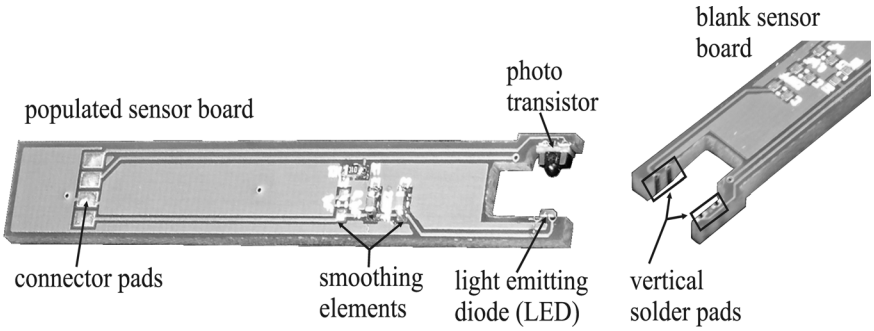

Figure 5.7 Sensor PCB including the fork structure, featuring the vertical solder pads.

5.3.2 Sensor housing

The major functionality of the sensor housing is to align the active sensor area relative to the dispenser nozzle. A symmetrical alignment of the nozzle to the sensor components entails the best sensor performance. The prototype housing was fabricated by a stereo lithography process [73] with an outline geometry of 65.5 mm x 9 mm x 3.4 mm.

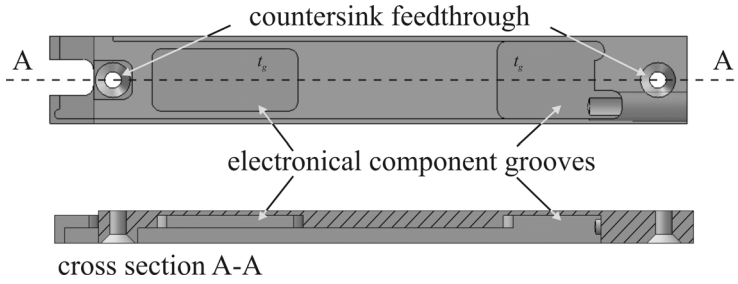

Figure 5.8 Design of the sensor housing prototype.

This matches the lateral geometry of the used PipeJet™ P9 dispenser exactly. The axial alignment of the sensor and the fixation to the PipeJet™-module is realized with two countersink screws (M1.6 VA2). The chassis does also provide a forked front side and follows the contour of the sensor board. Thus, the flight path of the dispensed droplets is not affected by the sensor. The sensor-board is glued up side down into the housing, thus all the electrical components are embedded in the sensor housing, hence sealed and protected from short cuts caused by contamination due to unintentional wetting by sample liquid, see figure 5.8 b).

5.3.3 Electronic read out circuit

To enable a reliable and reproducible sensor performance, a stable sensor supply voltage has to be assured to prevent fluctuations in the emitted light intensity. Furthermore, the sensor output voltage has to be considered to match the common requirements given by the A/D conversion application of standard micro controllers (µC). Thus, the output voltage has to be limited to U_{max}= 2.5V. To cope with the given requirements an electronic driving board was designed, which includes an active current regulation circuit to enable a highly constant illumination by the LED.

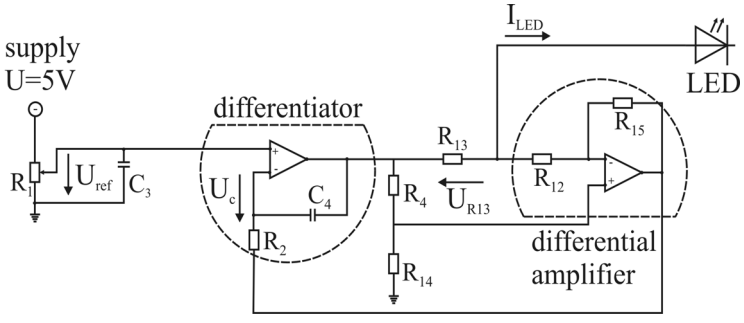

Figure 5.9 Electronic circuit of the applied current regulator

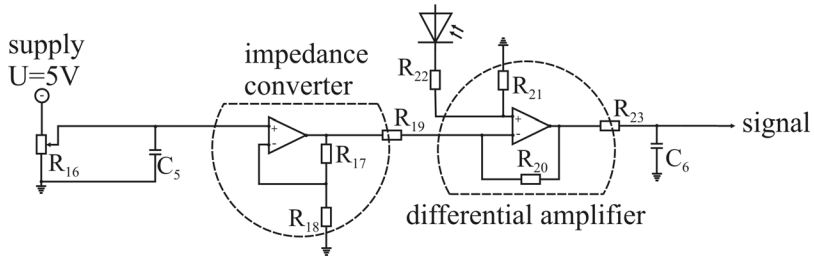

Figure 5.10 Electronic circuit of the applied offset regulation

The output voltage of the sensor can be adjusted by an adapted offset regulation circuit which is a further constituent of the driving board. A detailed block diagram of the current regulation circuit is given in figure 5.9. The functionality of the current regulator circuit is based on a voltage difference between the inverting and the non-inverting inputs of a differential amplifier, which leads to a voltage $U_c \neq 0$. An applied voltage $U_{ref} > U_c$ implies an increase of the differentiators output until $U_c = U_{ref}$. Therefore, a current I_{LED} flows towards the LED which entails a voltage drop U_{13} over the resistive element R_{13}. Finally, the circuit stabilizes this current at its defined value. The capacitor C_4 along with the resistor R_2 inhibits overshoots or fast current changes due to the defined time constant $\tau = R_2 \cdot C_4$. The applicable voltages, which can be supplied to the A/D converter input of the used µC (e.g. MSP430) can be maximal $U_{thresh} = 2.5$ V due to the internal reference voltage limits of the controller. For this reason an offset regulation has to be applied to decrease the maximum sensor output ($U_{max} = 5$ V) to prevent the µC of damages caused by overshoot voltages. The electronic circuit of the offset regulation is shown in figure 5.10. This offset-regulation enables the subtraction of a defined voltage from the photo diode output voltage without of influence to the sensor performance. An adjustable voltage is subtracted by a differential amplifier from the photo diode output, which compares the voltages on the inverting and the non-inverting input. For identical resistors $R_{19} = R_{22}$ and $R_{21} = R_{20}$ the output-voltage is equivalent to the difference of the input-voltages. The finally designed electronic supply board including the explained circuitries was fabricated in standard PCB technology. A constant voltage supply to drive the photo transistor was assured by the use of a commercially available voltage regulator IC. The implementation of the four operational amplifier steps, shown in the block diagrams of the circuits was realised by a four channel opamp TS 914 from ST Microelectronics. The final board inclusive the chassis is shown in figure 5.11.

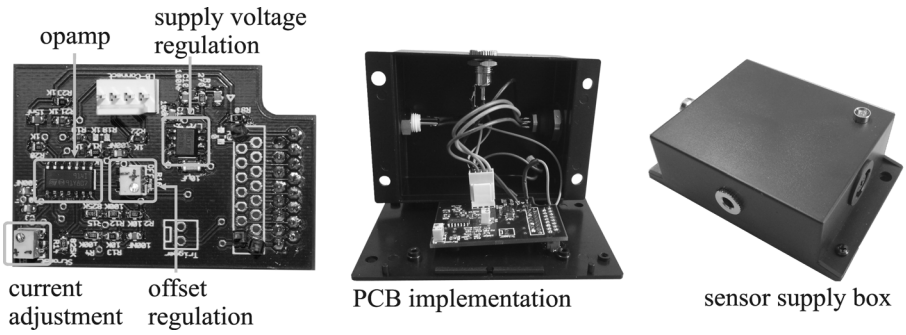

Figure 5.11 electronic supply board integration and housing

5.4 Characterisation - single droplet detection

The following section presents the characterisation of the optical droplet sensor prototype based on the direct light beam method . The generated signals are analyzed with respect to the influence of different droplet parameters like droplet volume, velocity and malfunctions.

5.4.1 Experimental setup

The characterisation of the optical droplet sensor requires a measurement setup which enables to correlate the sensor generated signals with different droplet properties. These are mainly the droplet's volume, shape and velocity. A high precision balance was installed below the dispenser unit to weight the mass of the dispensed droplets as reference value. The used balance (Satorius SC2) features a resolution of $\Delta m = 100$ ng ($\rightarrow$ 100 pl for pure water) at a measurement range of 2.1 g. The measurement procedure is given in detail in chapter 2.1 together with the applied error assessment. The dispensing unit used for the sensor characterisation was the PipeJet™ P9 module.

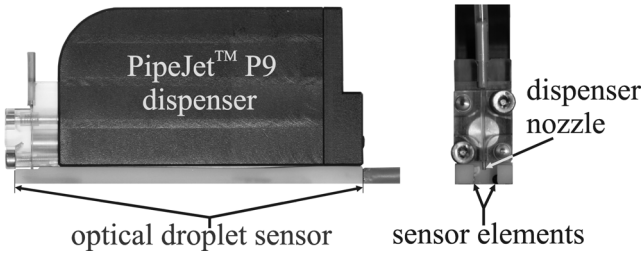

Figure 5.12 PipeJet™ P9 with mounted sensor unit underneath

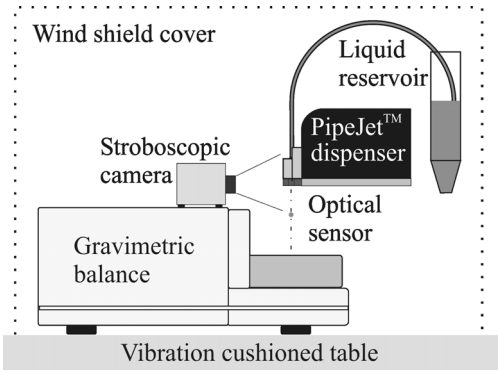

Figure 5.13 Principle sketch of the used experimental setup for the sensor characterisation.

The sensor was mounted underneath the dispenser using the mentioned housing to ensure the defined distance from dispenser nozzle to the sensor components and the symmetrical alignment of the nozzle, see figure 5.12. To monitor the single droplets during their flight visually a stroboscopic camera was installed in front of the sensor. Using the initial voltage raise of the dispenser's electronic drive to trigger the camera's release enabled to set software defined time delays after the initial dispenser actuation to record the droplets at different time defined positions. A sketch of the measurement setup is given in figure 5.13. The complete setup was installed on a vibration cushioned table and protected by a windshield cover to shield the measurement from environmental influence like airstreams or vibrations. The sampling of the sensor signals was realised by a standard A/D converter board from Meilhaus driven by an adapted measurement software. This software was programmed to store all acquired data in comma separated value (.csv) files for further evaluation.

5.4.2 Signal characteristics

The evaluation of the sensor was realised by the measurement of pure water droplets, generated at constant PipeJet^{TM} dispenser parameters. Thus, droplets of identical volume and velocity were dispensed through the active area of the sensor. An example for the sensor generated signals is given in figure 5.14. It correlates the shape of a standard sensor signal to three significant droplet positions, recorded by the stroboscopic camera. It can be seen that the initial sensor output voltage at $t < t_0$ is at a potential of approximately U_{out}= 1.13 V, which is the sensor output at full light exposure. This value might differ for certain measurements later in this work, based on improved initial adjustment.

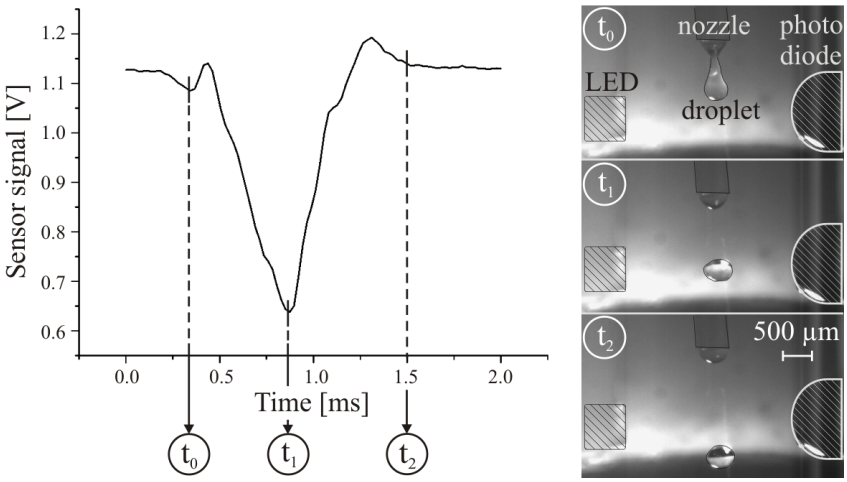

Figure 5.14 Typical sensor signal generated by a single water droplet, correlated to specific, time dependent vertical droplet positions relative to the sensor components.

The voltage drop after t_0 occurs from light intensity decrease based on effects of geometrical optics, explained in chapter 3. A droplet minimizes the light intensity at the photo sensitive element by passing the measurement light beam. The voltage decreases until the minimum at t_1 is reached. This is the point of lowest light intensity where the droplet reached the central position in between the sensor components. The exit behaviour of the droplet is described by the successive increase of the signal until the initial voltage is recovered. Theoretically, an absolut spherical shaped droplet with a constant velocity entails an absolut symmetric signal characteristics.

Further sensor evaluation was focussed on the influence of variable droplet volume. Therefore, various droplets of different volumes were dispensed through the sensor's active area. Figure 5.15 shows three sample signals generated by droplets of three different volumes (V = 13, 28 and 47 nl). Obviously, higher droplet volumes lead to larger voltage drops. This can be directly attributed to the higher absorption caused by the bigger droplets. Comparing the signal width for the 13 nl and 47 nl signals, it turns out that the signal generated by the droplet at lower volume leads to a wider shape of the signal. This effect is explained by the different droplet velocities, which occur from different dispensing parameters, necessary to generate different sized droplets. Slower droplets need a longer time to pass the emitted light beam, thus the width of the negative peak increases.

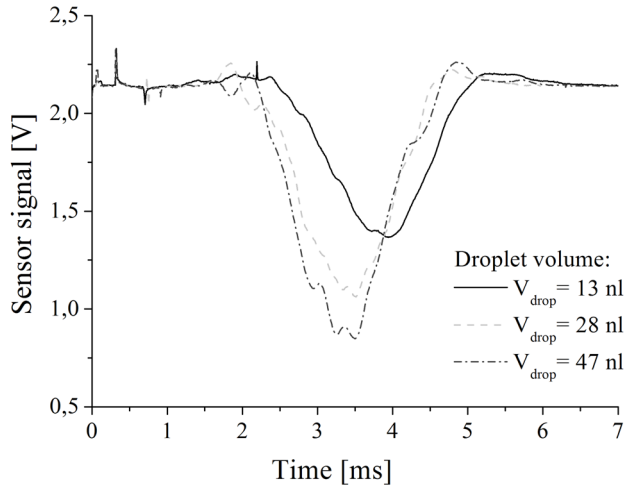

Figure 5.15 Individual sensor signals, generated by single droplets of different volumes.

Furthermore, it can be seen that each specific droplet volume and velocity entails a characteristic sensor signal. This can be interpreted as specific 'fingerprint' signal. A 'fingerprint' signal encodes all droplet parameters like droplet volume, velocity and the droplet shape in dependence on the liquid type. It is obvious that the interpretation of a certain signal at unknown liquid type, volume and velocity is hardly implementable to get the droplet characteristics. It would require to invert the dynamics of the light - droplet interaction in full detail which is not applicable in practice. However, a droplet sequence, dispensed at the same parameters using one liquid should lead to identical signals. Thus, any change in the successive signals identifies a change of a droplet property or dispensing parameter. Therefore, a semi-quantitative process control can be realised by the comparison of the individual senor signals. To quantify the sensor performance the sensitivity regarding small volume variations was determined. Therefore, single droplets with small variations in their volumes were generated. The droplet volumes were in the range from 42 to 47 nl. The resulted signals are shown in figure 5.16. It can be seen that the sensor enables to detect volume variations down to $\Delta V = 2$ nl of a liquid droplet of 45 nl volume by a significant change in the output signal. Taking the negative peak value as quantitative measure leads to a sensitivity of the sensor regarding the droplet volume of $S_i = 62.5$ mV/nl.

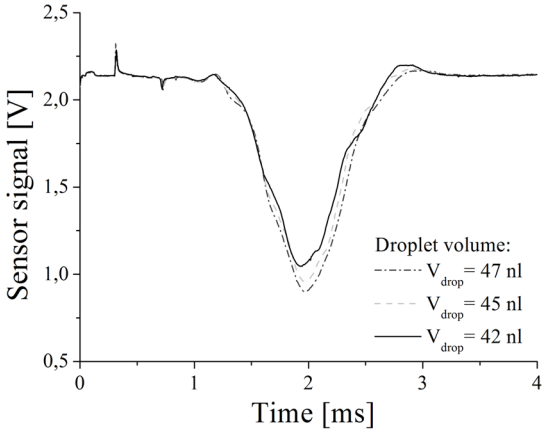

Figure 5.16 Individual sensor signals, generated by single droplets featuring very small volume variation.

However, quantifying the volume sensitivity of this sensor can hardly be implemented. Commonly known, the radius of a sphere influences the sphere's volume by the power of three, thus in a non - linear manner. Based on the Beer - Lambert law, the light absorbance of a certain body depends on the light transited length, thus the bodies geometry. Hence, the absorbance of a droplet will follow in a non - linear manner as well, which is true for spherically shaped droplets, see equation 3.7. Furthermore, this implies the dependency of the sensor signal on the shape of the dispensed droplets. Since droplets appear of arbitrary shape mostly, dependent on the dispensing parameters and liquid rheology, a volume calibration of this sensor is not feasible. Therefore, further investigations of the sensor sensitivity to droplet volumes were not realised.

Another considerable property for the sensor characterisation is the determination of the sensor resolution. This is the measure for the smallest detectable droplet. Theoretically, the droplet volume should have been decreased until the signal to noise ratio (SNR) falls below a reasonable value. This experiment was performed until the lower dispensing limit of the used PipeJet™ dispenser was reached resulting in a minimum droplet volume of V_{min}= 1.5 nl. Here, the sensor still featured negative voltage peaks of U_{peak}= 65 mV, see figure 5.17. This value in relation to the maximum noise of the sensor U_{noise}= 15 mV led to a SNR of 4.33. Considering a feasible SNR of 3, most likely even smaller droplets could be reliably detected by the presented optical sensor.

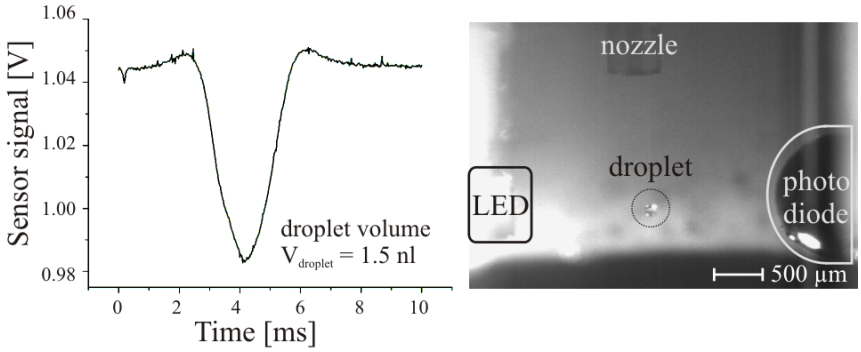

Figure 5.17 Sensor signal, generated by a droplet of V = 1.5 nl, defining the sensor resolution.

These measurements have shown that the negative signal amplitude strongly depends on the droplet volume. However, directly retrieving a quantitative value for the droplet volume was not possible. The sensor allows for the detection of a change in the droplet volume of $\Delta V = 2$ nl for a 45 nl droplet. It does not serve with quantitative information on the droplet volume since the voltage output does not depend on the droplet volume only. Further, the signal width shows a dependency on the droplet velocity. Due to the longer exposure time to the photodiode, slow droplets leads to an increase in the signal width. The influence of droplet velocity and shape to the signal will be explained in more detaile in the following section. To investigate the influence of droplet velocity, droplets were generated with the PipeJet™ dispenser at higher downstroke velocities. This entails a noticeable increase in the droplet velocity. The data acquisition as well as the image recording were triggered by the dispenser actuation at $t = 0$. The resulting signals of three droplets of different velocity are shown in figure 5.18. The individual vertical droplet positions after $\Delta t = 2$ ms are given by the stroboscopic images. Obviously, increasing droplet velocity leads to a time shift of the signal, caused by the faster approach of the droplet to the sensor, thus the earlier entrance into the sensitive sensor area. Furthermore, the signal width decreases for faster droplets, while steeper slopes of the signal peak can be observed. Figure 5.18 also highlights the effect of droplet shape on the sensor signal. The stroboscopic image of the droplet featuring a velocity of $u_{drop} = 1.4$ m/s (determined from a recorded stroboscopic image sequence) shows a dispensed droplet which splits into several single droplets (satellite formation). This can clearly be seen in the corresponding sensor signal. It shows two negative peaks which arise from the separated droplet.

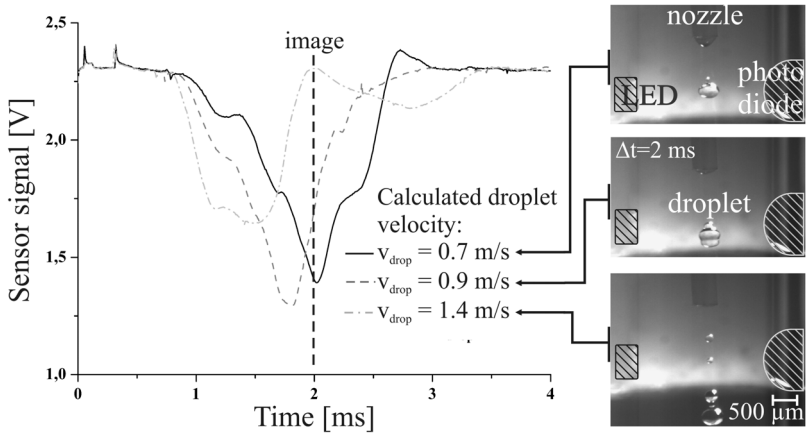

Figure 5.18 Evaluation of the droplet head velocity due to specific signal characteristics. Illustration of the droplet position at Δt = 2 ms, relative to the sensor components, of three individual droplets with different head velocity.

The first signal peak is generated by the main droplet and is comparable to standard droplet signals. The successive peak shows a much smaller negative amplitude and a wider shape, caused by a small and slow satellite droplet. This specific signal shape indicates for a malfunction in the dispensing process, which is clearly detectable by the signal interpretation. Obviously, the sensor is able to detect irregularities in a dispensing process like satellite formation. Also the droplet velocity is one of the major influence parameters defining the signal shape. The correct interpretation of the presented results suggests the possibility to estimate the droplet velocity directly from the generated signals. The droplet velocity can be calculated by the ratio of the moved distance of a droplet and the corresponding time interval. The distance from the entrance of the droplet to the position of lowest light intensity at the most negative signal peak was determined to be $\Delta x = 510$ µm. Assuming that the most negative signal peak is always generated at this particular position, the droplet velocity u_{drop} can be estimated by calculating the slope between droplet entrance and minimum sensor output:

$$u_{drop} \approx \frac{\Delta x}{t_{min}} \tag{5.4}$$

With Δx is the moved distance, t_{min} the time elapsed from its entrance until the signal has reached its minimum value.

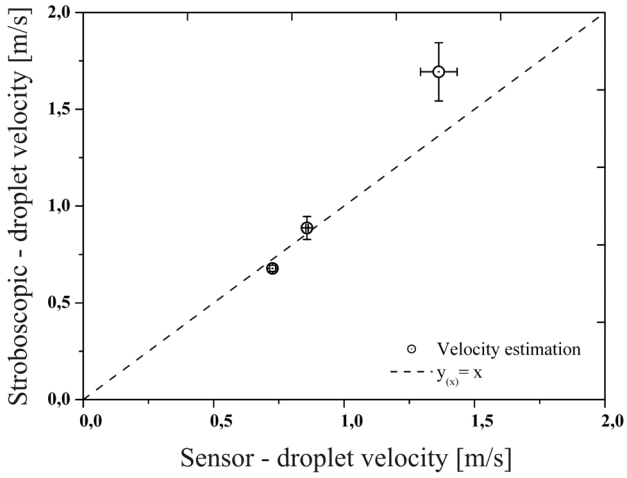

Figure 5.19 Correlation of the sensor determined droplet head velocity to the stroboscopic reference measurement

The droplet entrance is set to the point at which the recorded signal falls below the average sensor output. The velocity estimated by this method is compared to the stroboscopically determined value in figure 5.19. For a droplet velocity of 1.35 m/s it entails a maximal error in accuracy of $\Delta u_{ac} = \pm 0.3$ m/s and a deviation in precision of $\Delta u_{pr} = 0.3$ m/s, taken from the shown measurement.

5.5 Characterisation - liquid jet detection

Beside the detection of single droplets, the sensor is also applicable to monitor the dispensing process for liquid jet dispensing devices, e.g. dispensing valves or jet dispensing pipettes. In contrast to the detection of a single droplet, a liquid jet can not be comprised in its full volume at once by the light beam. A jet has to be sampled partially due to its length which exceeds the active area of the sensor. The detection of a liquid jet is rather comparable to a temporal scan of the ejected liquid quantity as it passes the sensor. Therefore, a separate characterisation study was done to investigate the sensor performance on this specific application.

5.5.1 Measurement setup

The measurement setup for the evaluation of the liquid jets' volume was identical with the previously described method. The difference was in the applied dispensing device.

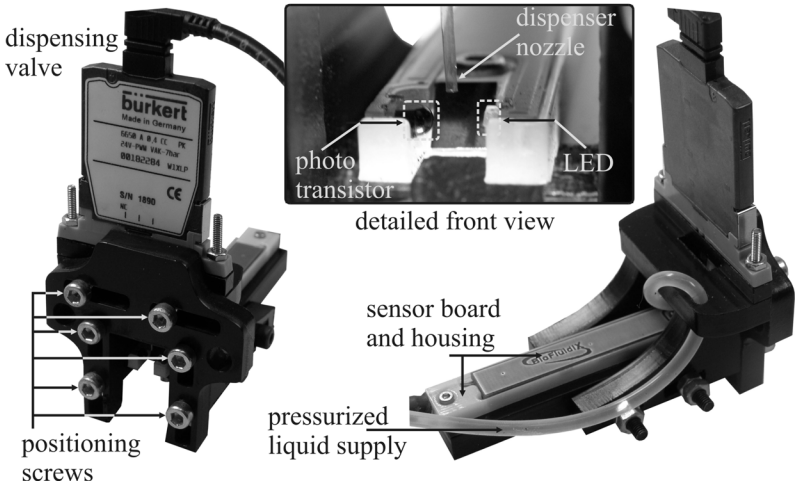

Figure 5.20 Experimental setup applied for the liquid jet detection experiments.

Instead of a PipeJet™ dispenser, a dispensing valve from Bürkert (Typ 6650 - 4,5 mm Flipper-Magnetventil) with a 500 µm nozzle was combined with the optical sensor. An adjustable support was fabricated which enabled the alignment of the nozzle to the sensor components in x-, y- and z- dimension. An illustration of the valve configuration is shown in figure 5.20. A disatvantage of the support was the bulk material surrounding the nozzle. This hindered to realise a satisfying illumination for recording of stroboscopic images of the ejected jets. To realize a correlation of the sensor generated signals to time defined images of an ejected liquid jet a further jet ejection device was used. The full automatic jet ejection pipette 'HandyStep™' from Brand enabled to realise satisfying illumination due to the free space at the nozzle. Hence, all depicted signal generation processes, featuring stroboscopic images are accomplished by the use of the HandyStep™ pipette. The HandyStep™ is an electronic driven handheld pipette, which enables the ejection of liquid jets in the µl range. All of the shown experiments were done by dispensing pure water as sample liquid.

5.5.2 Signal characteristics and evaluation

The theoretical background of the liquid jet detection is comparable to the single droplet detection and based on the same geometrical optics effects. Figure 5.21 shows a typical signal generated by a liquid jet. It shows the entrance behaviour ending at t = 75 ms. The HandyStep^{TM} pipette generates liquid jets, forming big droplets at their heads.

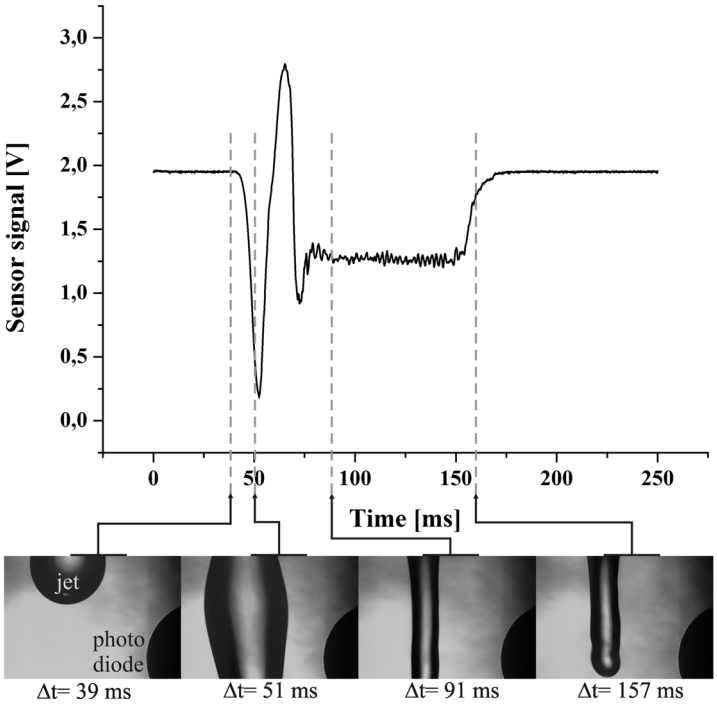

Figure 5.21 Correlation of a sensor signal, generated by the detection of a liquid jet, produced with the handy step pipette, to the corresponding stroboscopic image sequence.

Thus, the sensor generated signal at the entrance of this foregoing droplet is similar to the characteristics of a single droplet generated signal. After approximately t = 75 ms the jet forms a stable cylindrical shape and lead to the generation of a mostly constant sensor signal. The final slope depends on the driving mechanism of the dispensing device and reflects the retraction of the jet.

From now, all presented data in this section was acquired using the setup shown in figure 5.20. At a first experiment the liquid jets were generated at a supply pressure of 1 bar and variable valve opening times (c.f. figure 5.22), defined by the electronic actuation pulse. Typical sensor signals, generated by the use of the Bürkert dispensing valve are given in figure 5.22. It can be seen that the entrance behavior differs from the previously presented, generated with the HandyStep™ pipette. This can be deduced from a more constant, cylindrically shaped jet over the complete dispense time. Hence, the liquid jet does not form a leading droplet.

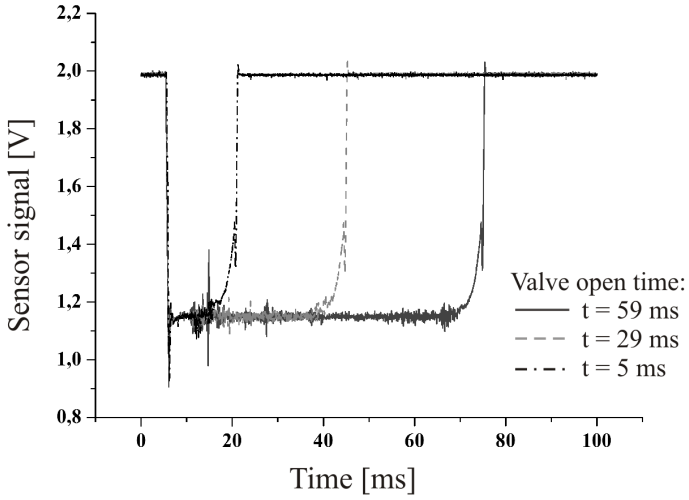

Figure 5.22 Typical signals generated by the detection of liquid jets dispensed at different valve open times.

The signals generated by a fractional scan of a dispensed jet enable to quantify the results with respect to the dispensed volume. This is based on the relation of the signal duration to the actually dispensed jet length. The constant signal plateau indicates for a stable jet shape, thus the liquid can be approximated as a cylindrical pillar. The integration of the generated signals over time lead to a quantitative value representing the volume of the measured jet. A correlation of the signal integral values and the corresponding dispensed volumes are shown in figure 5.23. The three data sets were recorded at different actuation pressures ($p = \{0.5, 1.0, 1.5$ bar$\}$) respectively. Higher pressures lead to an increase in the liquid flow, thus the liquid jet velocity. Therefore, high actuation pressures lead to the ejection of more liquid than low actuation pressures at identical actuation times. This explains the different slopes of the linear fits for the certain measurements in figure 5.23. To enable an accurate volume determination, the sensor has to be calibrated to the individual liquid jet velocity. But this requires the knowledge of the jet velocity which stays unknown here. It might go along with the actuation pressure for a given setup, but this was not investigated in this work in more detail. However, the signal integral to volume correlation led to a very good correlation coefficient for each individual measurement series ($r_{(x;y)} = 0.999$), thus an accurate quantitative calibration of the sensor to the liquid jet's volume is feasible.

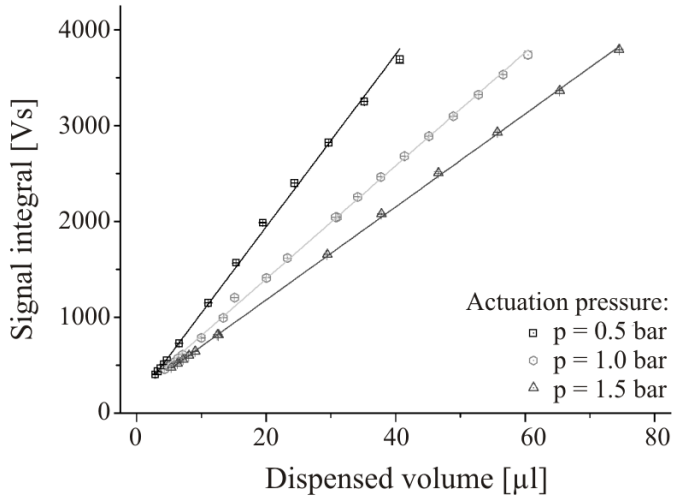

Figure 5.23 Correlation of the calculated integral of the recorded sensor signals to the corresponding volume of the liquid jets.

5.6 Application example

A first application of the optical droplet sensor was to observe the imprinting process of test lines to produce lateral flow assay test stripes using a PipeJet™ dispenser. It was aspired to realise a novel quality controlled imprint method for the fabrication of lateral flow assays in a batch mode [74]. The line printing process is based on the application of single droplets to the nitro cellulose (NC) membrane of the test stripe. The well defined distance from droplet to droplet to create homogeneous lines was controlled by the use of a BioSpot workstation from BioFluidix GmbH. Beside the determination of the single droplets absence/ presence, to confirm the individual quality of each line, the sensor was used to record the performance and reproducibility of the complete imprinting process semi-quantitatively, based on the correlation of the specific droplet 'fingerprint' signals.

5.6.1 Process control for the production of lateral flow assay test stripes

To realise an online process control using the presented optical droplet sensor, the acquisition of the analogue sensor signals was performed by a A/D converter board from Meilhaus electronics (ME 4610). The applied board features a maximum sampling rate of 400000 samples per second

(f_{sample} = 400 kHz). The provided dynamic link library (.dll) enabled the implementation of the A/D conversion to a specifically programmed read out software using visual basic.net. A screenshot of the established graphical user interface (GUI) is shown in figure 5.24. The illustration of the GUI is split into the single subdivisions. thereby, the signal display area is downsized. Information which is entered in the 'user information input box area' is used to generate the header for the measurement documentation. This allows for the allocation of the measurement data to the corresponding test stripe batch. The 'signal display' shows the droplet generated signals individually during a dispensing process. It enables a brief visual inspection of the successively dispensed droplets to estimate the process stability by the operator. The desired A/D conversion parameters (sampling rate and -duration, etc.) can be prompt in text boxes provided by the 'A/D parameter & status information'. The software features a status information, which automatically counts the successfully dispensed droplets and indicates for absent ones. A droplet is defined to be present by a specific threshold ('defect out') value, defining the voltage level which has to be exceeded by the sensor signal. By the application of this procedure, missing droplets can be identified and defect test stripes containing incomplete sample lines can be disposed or repaired.

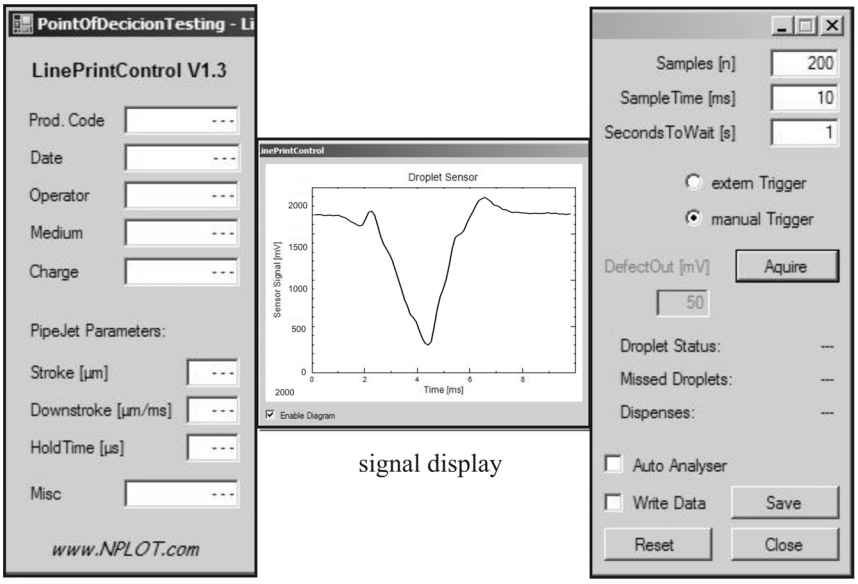

Figure 5.24 Graphical User Interface (GUI) of the process control read out software developed for the process control of imprint series of lateral flow assays.

The application of this procedure is an considerable improvement for the fabrication of lateral flow assays in a batch process. Commonly applied batch processes can not be controlled in an affordable manner according to the state of the art [75].

Beyond this qualitative process control a semi - quantitative evaluation of the reproducibility of an imprinting process can be implemented by the use of the optical sensor. The applied method will be given in the following. A well performing test stripe, providing quantitative results, e.g. the contingent of drugs in urine or saliva, requires to consist of highly homogeneous imprinted test lines. This allows for the simplification of the automated quantitative read out at high precision [12]. The realisation of the required performance by single droplet application implies the neccessity of highly reproducible droplet volumes. To verify the consistency of the printed droplets the signals generated by the optical sensor have to reflect this consistency by reproducible 'fingerprint' signals. To realise a semi - quantitative process control the individual sensor signals are correlated to a reference signal successively. Deviations in the signals indicate for alternations in the droplet properties. The required quantity reflecting signal deviations as quantitative value is given by Pearson's r correlation. It identifies the similarity by a value in the range from 1 to -1 [76]. Whereas $r_{(x;y)} = 1$ indicates for identical signals, $r_{(x;y)} = -1$ describes an inverse correlation. A value of $r_{(x;y)} = 0$ indicates for an absolute difference between the compared signals. Usually Pearson's r correlation is used to determine the linear correlation of two measurement sequences, e.g. the correlation of the voltage $U_{(x)}$ and the current $I_{(y)}$ regarding a resistance R characterisation. An absolute linear resistance characteristic would be indicated by $r_{(x;y)} = r_{(U;I)} = 1$. Taking the time dependent values of the reference signal as y-values and the actual measured data points as x-values, or vice versa, enables to apply Pearson's r correlation as quantitativ measure:

$$r_{x,y} = \frac{\sum_{i=1}^{n} (x_i - \bar{x}) \cdot (y_i - \bar{y})}{(n-1) \cdot s_x \cdot s_y} \tag{5.5}$$

where x_i is the actual considered value of the sampled sequence, $\bar{x}$ is the arithmetic mean of the entire smoothed data set, n the number of samples and s_x the standard deviation of the data set. The y values represent the reference values and hold the identical definitions. The mean values and the standard deviations are calculated by mathematical standard routines like follows:

arithmetic mean $\bar{x}$:

$$\bar{x} = \frac{1}{n}\sum_{i=1}^{n} x_i \tag{5.6}$$

standard deviation s_n:

$$s_n = \sqrt{\frac{1}{n}\sum_{i=1}^{n} (x_i - \bar{x})^2} \tag{5.7}$$

An example for an applied process control for the imprinting process of a lateral flow assay is given in figure 5.25. It shows n = 100 overlayed individual signals, recorded during the imprinting process. The reference value in this case is defined by the mean value of the entire signal sequences. To yield the quatitative results each individual signal was correlated to this reference by the explained procedure. The shown example resulted in correlation coefficients in the range from $r_{(x,y)}$ = {0.986 to 0.999}, which reflects the high consistency of the PipeJet™ dispensing process known from the gravimetrical measurements.

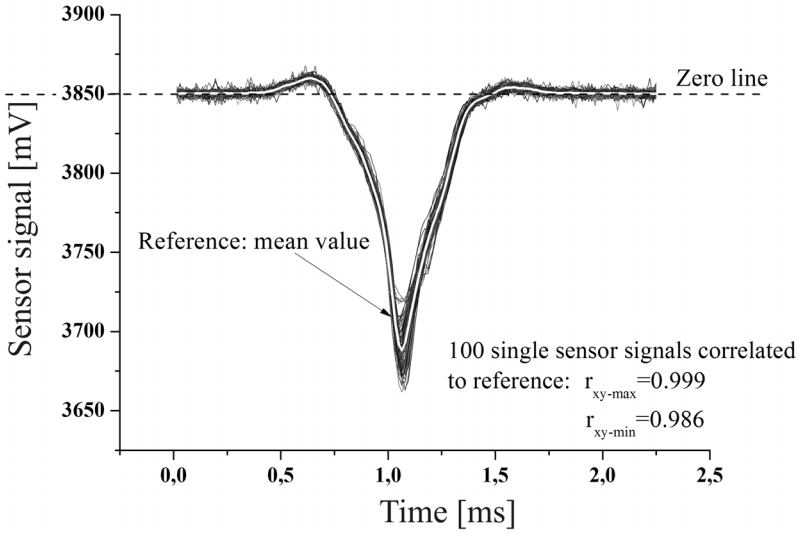

Figure 5.25 Signals of a sequence of n = 100 single droplets generated at one line printing process

However, an industrial application of this process requires a previously definition of a proper reference signal which might be generated by a calibration experiment. Furthermore, a threshold value depicting the r-coefficient boundary has to be defined to realise inadmissible deviations of the droplet properties to identify defective imprinting processes.

In conclusion the developed optical sensor unit can be taken as a smart integratable alternative to the presented state of the art systems. Beyond simple droplet detection, defined as priority 1 in chapter 1, the sensor allows for a semi quantitative process control for non-contact dispensing devices in the nanoliter range. The correlation of the sensor generated fingerprint signals enable the quantification of the reproducibility of an imprinting process. Therefore, priority 2 is successfully implemented. In case of liquid jet detection the sensor enables a dispensed volume quantification. However, a calibration to the liquid jet velocity is mandatory to get reasonable results. Priority 3 is achieved for known jet velocity, only.

Due to the clear dependency of the measurement principle on the liquid properties, influencing the effect of geometrical optics, a media independent measurement procedure could not be implemented and was not further studied. To realise an advanced sensor performance regarding the non-contact determination of the volume of free flying single droplets, another measurement principle, based on capacitive interaction, was evaluated and studied in detail, which will be given in the following chapters 6 and 7.

Chapter 6
Capacitive droplet detection - theory and simulation

The method to detect free flying liquid droplets by the change in capacitance of an open plate capacitor, consistent of two plane parallel electrodes, was already published by William P. Winn in 1968 [24]. His work deals with the detection of rain drops (r = 1.6 mm) by the change in capacitance. A major result is the definition of the basic function for the numerical calculation of the change in capacitance caused by a spherical body introduced between two parallel capacitor plates given by [77]:

$$\Delta C = 4 \cdot \pi \cdot \varepsilon_0 \cdot \frac{r^3}{s^2} \cdot \frac{\varepsilon_r - 1}{\varepsilon_r + 2} \tag{6.1}$$

, where ΔC is the change in capacitance, ε_0 the permittivity of the vacuum, r the radius of the spherical body, s the distance of the capacitors electrodes and ε_r the relative permittivity of the sphere's material. However, the experiments for the determination of the rain drops' size, have been accomplished by Winn in a contact manner only. The droplets need to get in contact with one of the capacitor electrodes, thus imply a significantly higher change in capacitance in comparison to the situation described by equation 6.1. Furthermore, contact of the measured droplets to the sensor's surface entails contamination or even loss of the measured liquid, which would not be acceptable for the application considered in this work. Therefore, a droplet has to be analysed while it passes the electric field of a capacitor without contact to any solid material.

The following chapter deals with the comprehensive study of the measurement principle briefly reflected by equation 6.1. The thorough assessment provided in this thesis includes a numerical study of the physical fundamentals by the application of a computational fluid dynamics (CFD) simulation tool. Furthermore, the design, fabrication and characterisation of two sensor types, featuring two different analogue read out circuits are given in detail in chapter 7.

Based on the developed sensor technology a novel technique for the quantitative online observation of a dispensing process of single liquid droplets in the nanoliter range is presented.

6.1 Capacitive measurement principle

Early applications of capacitive sensors have been typically based on geometrical variations of the capacitor electrodes relative to each other in several conceivable dimensions. Applying such method allowed for the developement of pressure-, proximity- or acceleration sensors [78-82]. Due to the variation of the electrodes distance, overlap, surface etc. the capacitance of the transducer changes as a function of the causative quantity according to the theory given in chapter 3.2. For example the first capacitive pressure sensor was developed by Sander in 1980 [83]. But also alternations in the characteristics of a specific dielectric inserted into the electric field of a capacitor lead to changes in capacitance, thus being applied in industry e.g. for humidity measurements [84]. The basic principle of the sensor studied in this work is based on the change in capacitance caused by the presence of a dispensed liquid droplet in between two charged electrodes. It passes the electric field of an open plate capacitor on its way from dispenser nozzle to the target substrate. The basic principle is illustrated in figure 6.1

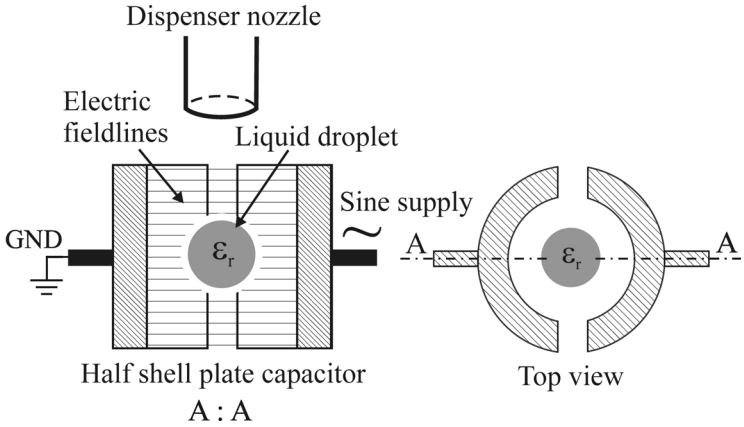

Figure 6.1 Sketch of the capacitive droplet detection method

An open plate capacitor is installed below the dispenser orifice in a defined distance to enable a droplet to pass through, whereas it affects the electric field in between the electrodes. The influence to the electric field entails a change in the charge distribution on the electrodes, thus implies the change in capacity. For the purpose of droplet measurement by an open plate capacitor the space in between the electrodes has to be adapted to the size of the droplets in the target volume range, such that the plates are prevented from wet contamination by the measured droplets. Also malfunctions of a dispensing process, like the ejection of satellite droplets or deviations in the flight path of the droplets have to be considered and contribute to the distance between the

capacitor plates. Due to the non - contact measurement principle of the presented capacitive method, a liquid droplet can be considered as a dielectric material with a relative permittivity $\varepsilon_r > 1$. A droplet fills the space in between the measurement electrodes partly and must not touch any of the electrodes. Therefore, eq. 6.1 holds for the calculation of the change in capacitance, if a perfectly spherical shaped droplet passes a parallel plate capacitor. However, droplets which are dynamically ejected from a dispenser orifice mostly do not appear as spherically shaped bodies. More often the liquid forms liquid jets and fluctuates during its flight. Thus, equation 6.1 can be seen as a first estimation only. The limits of the expected changes in capacitance for pure water droplets with a relative permittivity of $\varepsilon_r = 81$ were calculated according to eq. 6.1. The considered droplet size was in the range from $V_{drop} = \{5 \text{ to } 120 \text{ nl}\}$ (corresponding radius range $r_{drop} = \{106 \text{ to } 306 \text{ µm}\}$). The distance of the electrodes was defined to be $s = 1$ mm in first instance. These first calculations resulted in changes in capacitance for the considered geometry in the range from $\Delta C = 0.1 \cdot 10^{-15}$ to $3 \cdot 10^{-15}$ F. The major challenge in this work was to realise a sensor unit which enables to transform such small changes in capacitance to a readable magnitude in a cost efficient manner. A smart implementation of the complete readout circuit close to the sensor unit, avoiding the use of external amplifiers, is one of the basic requirements for the practical application of this concept.

6.2 Analytical model

For a first theoretical examination of the capacitive sensor concept, an analytical model was derived according to equation 6.1. The model was adapted to a half shell shape of the capacitor electrodes, like used for an early experimental proof of principle described in [85].

6.2.1 Capacitance of a half shell electrode capacitor

A fundamental value required for the design of the droplet sensor is the initial capacitance of the measurement capacitor. Based on previous experiments [85] a half shell shape of the capacitor electrodes is considered in first instance. To enable accurate results by the analytical model, equation 3.15, which is based on geometrical conditions of a capacitor, was adapted to the specific half shell geometry. Figure 6.2 shows the considered electrode geometry set to the origin of a coordinate system to support the derivation of the corresponding equation. The dimensions of the capacitor's geometry are provided in the illustration. In contrast to plane parallel plates, the distance y of the capacitor plates changes as a function of x.

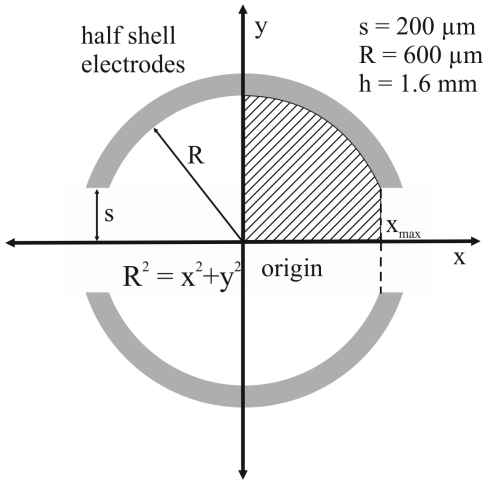

Figure 6.2 Sketch of the capacitor geometry for the calculation of the capacitance of an empty half shell capacitor.

Therefore, a definite integral is required for the calculation, which is based on the circular coordinate equation $(x-x_O)^2+(y-y_O)^2 = r^2$ leading to following equation 6.2:

$$C_0 = 2 \cdot \varepsilon_0 \cdot h \int_0^{\sqrt{(R^2-s^2)}} \frac{1}{2 \cdot \sqrt{R^2-x^2}} dx \qquad (6.2)$$

where h is the height of the electrodes, s is the half width of the capacitor trench and R the inner radius of the half shell electrodes. By negligence of the actually inhomogeneity of the electric field in between the curved electrodes, the application of the geometrical dimensions given in figure 6.2, leads to an initial capacitance of the half shell capacitor of $C_0 = 17.4 * 10^{-15}$ F = 17.4 fF.

6.2.2 Change in capacitance caused by a spherical droplet

The analytical model based on equation 6.1, which gives the change in capacitance of a plane parallel plate capacitor caused by an spherical shaped droplet, can be readily extended to the half shell geometry. To meet the given geometry, the constant distance s defined by the parallelism of the plates was eliminated by substitution with the equivalent term $s = E/U$ based on eq. 3.11. This substitution follows the derivation given in [24], which also deals with further details.

Thus, equation 6.3 is straight forward established, which enables the calculation of the change in capacity caused by a spherically shaped body with the specific relative permittivity ε_r by the consideration of the electric field E_d in the region of the spherical droplet only:

$$\Delta C = 4 \cdot \pi \cdot \varepsilon_0 \cdot \frac{E_d^{\,2} \cdot r^3}{U^2} \cdot \frac{\varepsilon_r - 1}{\varepsilon_r + 2} \tag{6.3}$$

The electric field affected by a droplet changes with the droplet size at constant electrode geometry. The non - constant distance of the curved electrodes (considering x - dimension; c.f. figure 6.2) contributes to this effect. To incorporate these detail a further equation was derived which enables the calculation of the electric field for variable droplet size considering the distance of the electrodes in dependence on variable x - dimension. Equation 6.4 is deduced according to the basic equation describing the electric field between two charged elements, see eq. 3.14. Assuming a homogeneous electric field it gives the electric field strength in the area of the droplet and is written as follows:

$$E_d = \frac{U}{r} \cdot \int_0^r \frac{1}{2 \cdot \sqrt{R^2 - x^2}} dx \tag{6.4}$$

Here r is the radius of the droplet and R is the radius of the half shell capacitor's incircle. Inserting eq. 6.4 into eq. 6.3 leads to equation 6.5 which enables to determine the change in capacitance of a half shell electrode capacitor, caused by a spherically shaped droplet:

$$\Delta C = \pi \cdot \varepsilon_0 \cdot r \cdot \operatorname{asin}\left(\frac{r}{R}\right)^2 \cdot \frac{\varepsilon_r - 1}{\varepsilon_r + 2} \tag{6.5}$$

Figure 6.3 shows the correlation of the change in capacity to the radii of the corresponding droplets, calculated according to eq. 6.5. It can be seen that a droplet with a radius of r_{drop}= 287 µm, corresponding to a droplet volume of V_{drop}= 100 nl, entails a change in capacity of ΔC = 1.9 fF only. As a further theoretical examination the influence of variations in the capacitor's diameter was studied by the analytical model eq. 6.5. Therefore, half shell electrode capacitors were considered featuring incircle diameters in the range from ID = {600 to 2000 µm}. The droplet volumes were varied from V = 25, 50 and 100 nl which corresponds with droplet radii of r = 181, 229 and 287 µm.

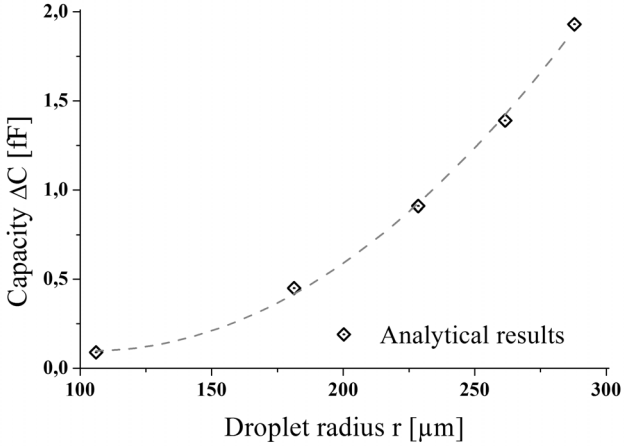

Figure 6.3 Change in capacitance according to the analytical model (equation 6.5) in correlation with the corresponding droplet radius

The results are given in figure 6.4. It can be seen that a decreasing capacitor diameter improves the sensitivity to droplet volume of the considered measurement method enormously. A decrease of the capacitor diameter e.g. from 1200 µm to 600 µm improves the volume sensitivity, given by the change in capacity, by the factor 6, considering a droplet volume of 100 nl.

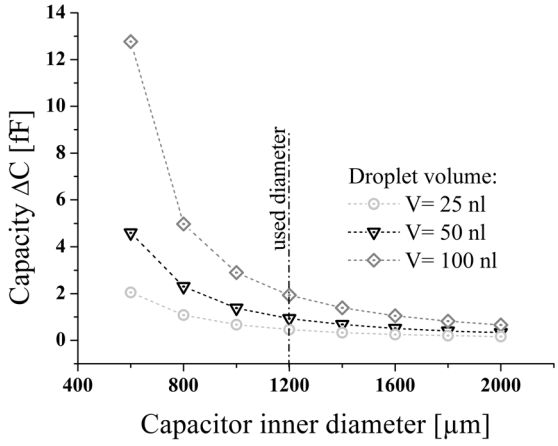

Figure 6.4 Analytical calculation of the influence of different capacitor diameters to the change in capacity caused by droplets of different volumes for the given geometry.

6.3 Numerical simulation

To improve the theoretical considerations regarding the realistic influence of dispensed droplets to the electric field of a capacitor a numerical simulation study was accomplished. This study considered beside the electic field calculations also the droplet ejection process. Therefore, the influence of droplet deformation, droplet velocity as well as different droplet volumes on the electric field could be evaluated. The established multi - physics model was realised using the commercially available software tool CFD ACE+ (computational fluid dynamics) from the ESI - group [57] and is given in the following.

6.3.1 System description - equivalent electrical circuit

A dispensing process comprises two distinct phases which are the droplet's growth until its tear - off from the dispenser nozzle and the free flight of the droplet after it has detached from the nozzle. It turned out that these two situations result in different boundary conditions for the electrical problem of the charged capacitor. Both situations can be described by two different electrical equivalent circuits like follows: In first consideration, a growing droplet is connected to the liquid inside the nozzle, which stays in contact to the aluminium housing of the used dispenser unit via the dispensing piston, like described in detail in [62]. The housing is electrically connected to the ground potential (GND = 0 V) of the electric read out circuit due to guarding reasons, to avoid the induction of external stray fields, caused by the PipeJet^{TM} dispenser actuation. More information about sensor guarding can be taken from section 7.1.2. The liquid is guided through the non - conductive PipeJet^{TM} polyimide tube, thus it has to be supposed that the electrical potential of the liquid inside the nozzle is coupled to the housing potential via a capacitive network. This network can be considered to consist of a capacitor series connection given by C_{liquid}, C_{Wall} and C_{Solid} like shown in figure 6.5. This effect is referred in the following as ’capacitive coupling’ and is essential for the specific signal characteristics. The signal recording starts when the dispenser is actuated and subsequently a growing droplet is established. The charge on the positive electrode is compensated by negative free charge carriers, distributed on the measurement capacitor's negative electrode as well as on the increasing surface of the growing droplet. The increasing surface of the growing droplet leads to a shift from charge carriers from the negative electrode to the droplet surface and thus to an overall decrease of the charge on the negative electrode, implying a decrease of the average capacity. The appearing charge separation on the droplet's surface can be explained by the existence of free charge carriers, which are found even in de-ionized water

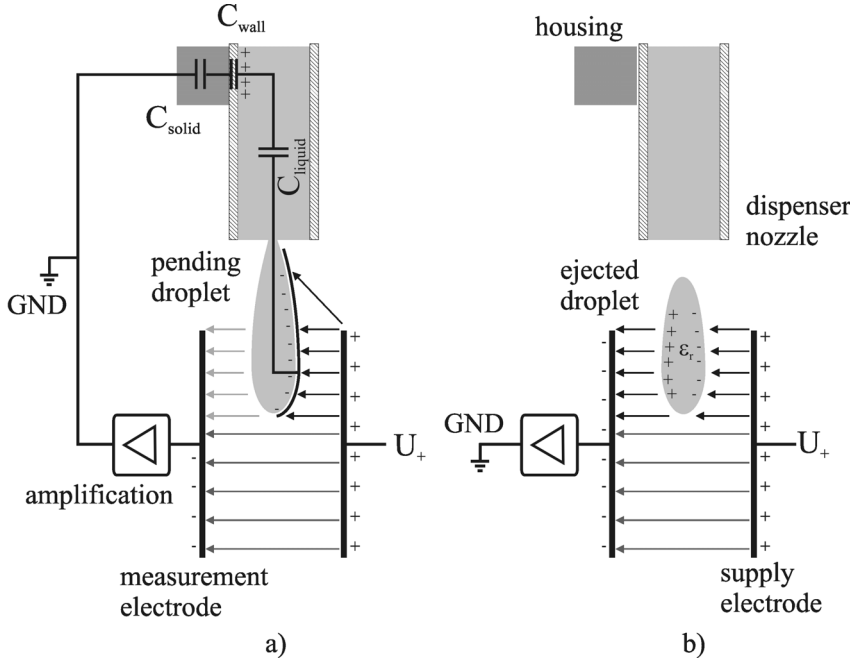

Figure 6.5 Two basic conditions of the equivalent model. a) Pending droplet is connected to the electronic system by capacitive coupling; b) droplet after tear off acts as dielectric.

based on auto ionization of liquid water [86]. It implies that beside the orientation polarization of the liquid molecule dipoles (considering water), initiated by the electric field, also a charge separation occurs. This compensates the applied electric field partly with regard to the GND potential. After the droplet's tear off from the nozzle the situation changes. The detached droplet is disconnected from the GND potential and acts as dielectric body only (c.f. figure 6.5 b)). A dielectric material changes the capacitance of a capacitor according to its size and relative permittivity and leads to an increase of the charge on the measurement electrode.

6.3.2 Simulation process and computational domain

The realisation of the numerical model is based on a structured 3D grid consistent of the droplet generator and the capacitor electrodes. The computational domain, shown in figure 6.6, consists mainly of half shell shaped cylindrical electrodes and some air space above and below the capacitor. The liquid column at the top side of the domain represents the liquid phase inside the nozzle of the droplet generator.

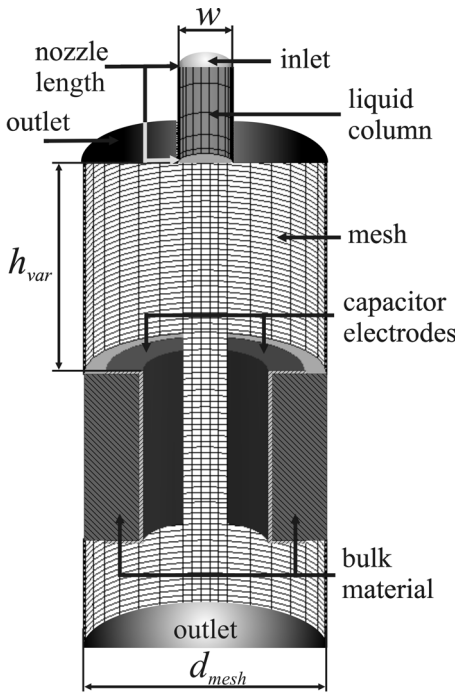

Figure 6.6 Computational domain of the 3D setup applied at the CFD simulation

This enables to implement the simulation of a droplet ejection process. The nozzle diameter is w = 500 µm corresponding to the experimentally used PipeJet^{TM} dispensing system. The adjustable nozzle length enables to study the effect of capacitive coupling in detail and was initially set to l = 500 µm. The capacitor electrodes are centred underneath the nozzle with an adjustable distance h_{var} (initial distance h_{var} = 2 mm). The geometry of the capacitor featured an inner diameter of d = 1.2 mm and a trench width of s = 400 µm, separating the electrodes. The electrodes height is also varied in this work to study its influence to the measurement method. The default height is set to z = 1.6 mm. The electrodes are embedded in bulk material made of FR4. In order to save computation time the symmetry of the model has been exploited, thus only half of the spatial geometry was modelled as shown in figure 6.6.

6.3.3 Initial conditions and boundary conditions

The numerical study of the capacitive measurement method for free flying droplets requires the implementation of a droplet ejection process to the model. This process should lead to droplets with realistic properties in terms

of shape, volume and velocity. To keep the focus on the essential part of the study, the electrostatic interaction itself, a simple droplet ejection model was realised, based on a liquid flow boundary condition. Therefore, a liquid flow of a constant velocity of $v_{flow} = 2.5$ m/s was set as boundary condition at the top inlet of the cylindrical liquid column (c.f. figure 6.6). The flow was active for t = 70 µs and stopped instantly to initiate the droplet tear off. The applied parameters led to a droplet ejection process like shown in figure 6.7. It reflects realistic and representative droplet properties like volume (V = 33 nl), shape and velocity (u = 1.4 m/s). The wetting conditions for the walls surrounding the nozzle were set to a wetting angle of $\alpha_{water} = 68°$ for pure water. Furthermore, an outlet is defined at the lower end of the model to enable a balance of occurring pressure in the domain, caused by the droplet ejection. The wetting conditions at the electrodes are set to a 'no wetting' boundary condition ($\alpha_{water} = 180°$) to avoid falsification of the results due to wet contamination of the electrodes. The boundary condition for the electric field inside the capacitor is given by constant electrical potentials on the two opposite electrodes. The electrode on the left side, see figure 6.6, is defined to be the measurement electrode and features an initial potential of $U_{GND} = 0$ V, whereas the electrode on the right side is set to a constant potential of U = 10 V. The implementation of the capacitive coupling effect, like described in section 6.3.1, is realised by an electrical boundary condition at the top of the liquid column (inlet; c.f. figure 6.6) which is set to GND potential $U_{GND} = 0$ V. The liquid column's height represents the average capacitance of the capacitive network consisting of C_{liquid}, C_{Wall} and C_{Solid} in section 6.3.2. To obtain quantitative results the charge alternation on the measurement electrode is monitored during the simulations and extracted for further evaluation.

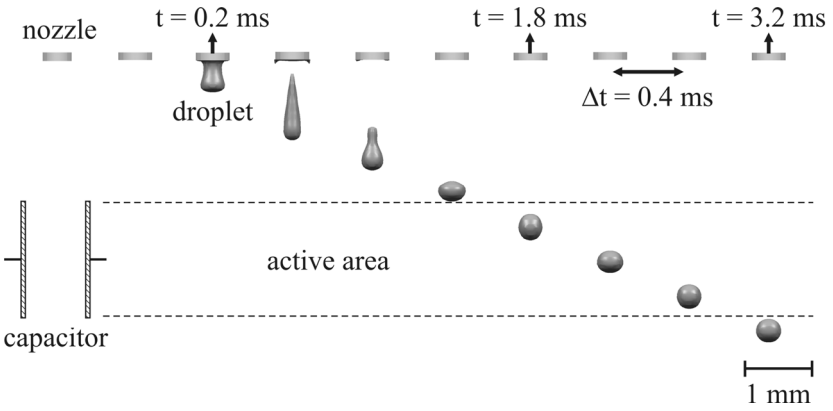

Figure 6.7 Visualisation of the simulated droplet ejection process at different time delays.

The properties of the used fluids are taken from the material database, provided by CFD ACE+ and are listed in table 6.1.

Table 6.1 Applied parameter settings for the CFD simulation of the corresponding computational domain, see figure 6.6.

	space	**electrodes**	**bulk**	**liquid**
material	air	copper	FR4	water
dynamic viscosity [mPas]	0.0185	n/a	n/a	1.0
density [kg/m^3]	1.161	8920	1400	1000
surface tension [N/m]	n/a	n/a	n/a	0.0725
permittivity	1	18.1	5	80.1
conductivity [S/m]	$0.3 \cdot 10^{-14}$	$59.6 \cdot 10^{6}$	n/a	$5.5 \cdot 10^{-6}$

A more detailed overview about the used simulation settings, including solver options can be taken from [87].

6.3.4 Solution technique and grid refinement study

The applied solution technique to solve the partial differential equations in the computational domain follows the finite volume method, like described in chapter 3.3. The whole domain consists of 540,000 cells whereas the area along the flight path of the droplet consists of a grid of smaller cells in comparison to the surrounding cells (cell size ~ 3:1). The geometry of the considered setup enabled to set a symmetry boundary, which allowed for the calculation of only half of the real geometry. The simulation required transient conditions at a defined time step of t = 1 µs and a convergence criteria of 0.0001. To evaluate the accuracy of the numerical calculations a brief grid refinement study was accomplished to investigate the influence of the cell size. To estimate the discretisation error the side length of all cells was decreased in all dimensions by the factor 2 and 4 and increased by the factor 2 respectively. Simulations were performed with the different grids by stationary simulation of an empty capacitor as well as for a capacitor with a 50 nl droplet introduced in the middle of the electrodes. The value of interest here was the change of the charge on the measurement electrode for the empty capacitor compared to the droplet filled one. The results are given in figure 6.8 for the various grids. It can be seen that the charge, depicted on the y - axis, declines for smaller grids, equaling a higher grid scaling number n (x-axis). The polynomial fit converges to a value of about $Q = 1$ fC representing the 'real' physical condition.

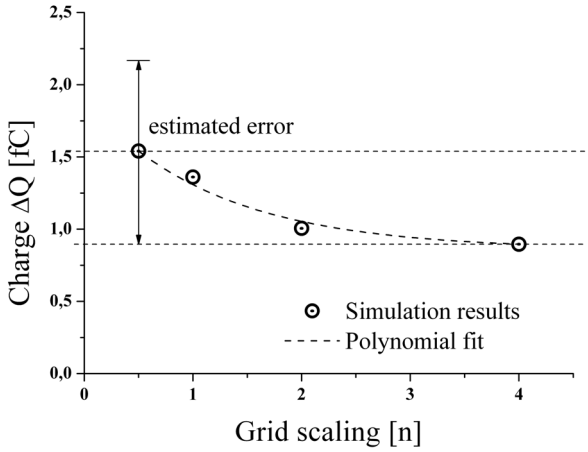

Figure 6.8 Simulation results of the grid refinement study

Based on this grid study the error of the transient simulations presented in the following was estimated to be about + 29% at the application of a grid scaling of 1. This error is quite considerable, because a grid scaling of 1 was used for all further studies. The application of increasing grid scaling numbers exceeded the reasonable computational time. Obviously, the presented grid study exhibits a convergence to smaller values for higher grid scaling numbers. However, in the general case it cannot be assumed that this is the case for any initial or boundary condition. Therefore, the estimated error is assumed to be symmetric about the simulated values.

6.3.5 Influence of droplet presence to the electric field

In first instance the presented computational model was used in a simplified setup to investigate the feasibility of solving the multi disciplinary problem with the used simulation tool at all. Therefore, first simulations were performed with defined spherical droplets of various volumes (V = {5 to 100 nl}) instead of the application of the droplets ejection process given in section 6.3.3. The droplets were defined as initial conditions in the model, passing the capacitor with a constant shape and a defined velocity of u = 1 m/s. The value of interest was the charge on the measurement electrode, which was extracted as a function of time. The charge characteristics resulting from the individual simulations are shown in figure 6.9. The almost symmetric change in charge reflects the flight of a droplet through the capacitor. The maximum change in charge is reached when the droplet approaches the horizontal centre line of the capacitor, like shown in figure 6.9 (t = 2.6 ms @ V = 50 nl).

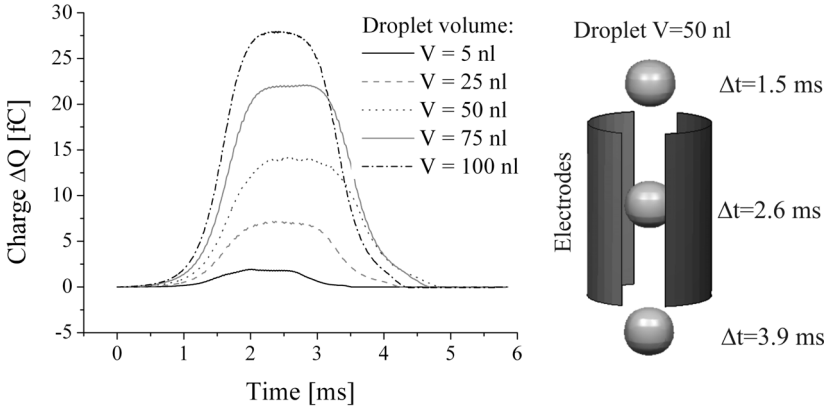

Figure 6.9 Change in charge as a function of time caused by spherically shaped droplets of different volumes passing the capacitor as shown in the illustration for a spherical droplet of V = 50 nl at three specific points in time

Like expected, the maximum charge alternation increases with higher droplet volumes, thus the feasibility to apply the sensor for volume measurements is confirmed. However, the full model of the dispensing process has to be considered to include the droplet tear off process as well as the effect of capacitive coupling.

6.3.6 Electric field characteristics

The implementation of the droplet generation model considering the GND boundary on top of the domain (inlet) entailed a different signal characteristics. Following the explanation given in section 6.3.1 two separate situations can be distinguished, like given in figure 6.10. The image shows a complete sequence of the simulated measurement process. Seven time discrete phases are illustrated to visualize a simulation procedure. It can be seen that the electric field gets increasingly attracted by the growing droplet from image 1. - 3. This implies a decrease of the charge on the measurement electrode which can be seen in figure 6.11. It depicts the corresponding signal characteristics to this simulation. After the droplet's tear off (image 4 and following), the droplet acts as dielectric body, increasing the charge on the electrode due to its specific permittivity and volume. Some of the field lines still keep attracted by the nozzle, which is always connected to GND potential. This field is constant over time, hence it does not influence the absolute value of the measurement.

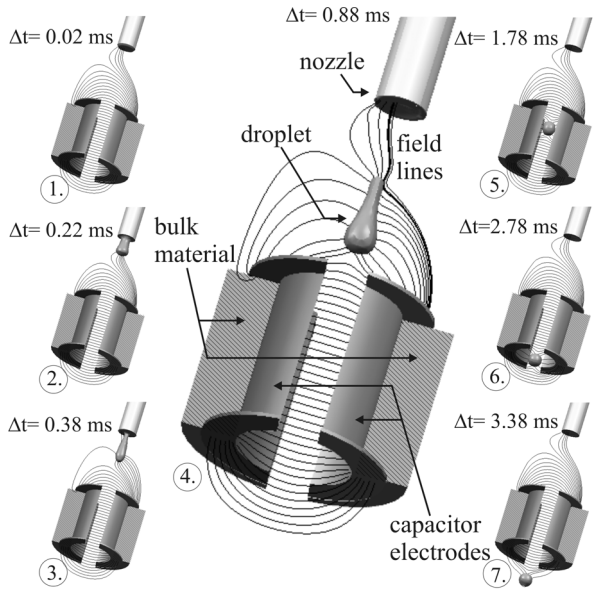

Figure 6.10 Simulated droplet ejection process, including the measurement electrode of the capacitor featuring the electric field lines. The time delay between the single images is given in the figure respectively.

Movement of the liquid meniscus at the nozzle might entail additional fluctuations to the signal which could not be observed for the settings studied so far. The corresponding change of charge over time on the measurement electrode is shown in figure 6.11 ii). A noticable detail is the initial negative signal peak, which occurs from the phase before the droplet tears off from the nozzle. Afterwards, the signal raises to a maximum, dependent on the droplet size and liquid properties.

Further details which can be taken from figure 6.10 are the different surfaces developing the field lines. It can be seen that the upper and lower part of the electric field originates from the top- and bottom-face of the capacitor, (denotations of the surfaces can be taken from figure 6.11). To study the surface dependent constitution of a complete signal, the measurement capacitor was analyzed with respect to the percental contribution of the different surfaces of the model. The most important surfaces, which are mainly contributing to the specific signal characteristics are reviewed in figure 6.11 i) and are indicated by a) to d). All other contributing surfaces, which define the capacitor geometry, like the edges or inner surfaces are not specified individually here. The lower diagram in figure 6.11 ii) shows the percentual contribution of all individual surfaces to the signal generation.

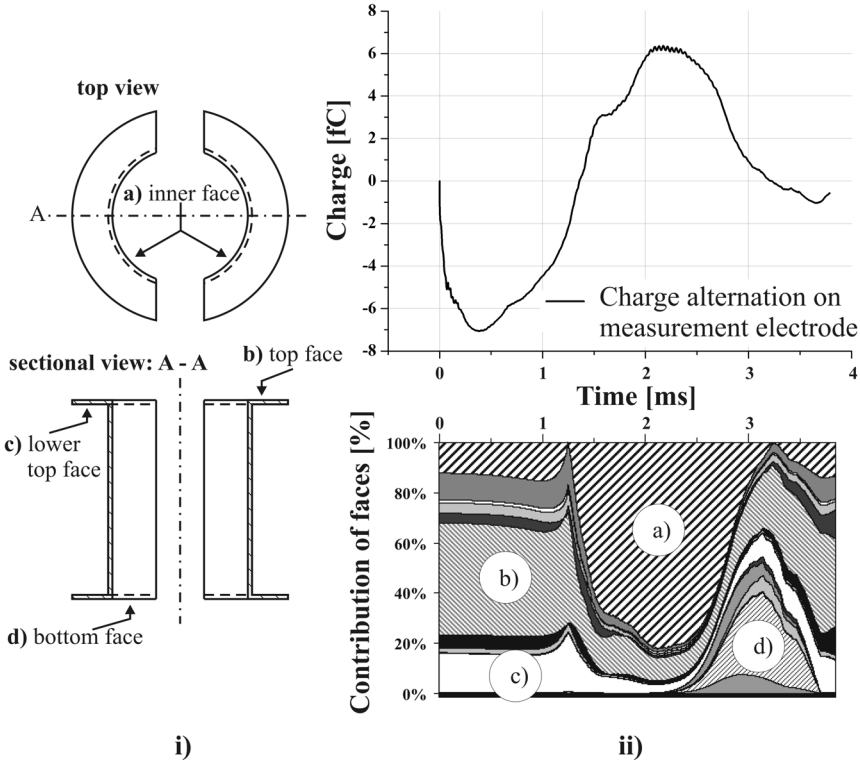

Figure 6.11 Contribution of the different surfaces to the total charge alternation. Definition of the important surfaces by the different views of the electrodes. All less important faces are not given in detail.

The specific contributions of the main surfaces over time are indicated by a) to d) again. It can be seen that the initial negative peak, based on the capacitive coupling effect, is mainly caused by the ’top face’ b). The positive peak is mostly generated by the alternations at the inside (inner face a)) of the capacitor. The exit of the droplet after t = 3 ms is monitored by the ’bottom face’ d) including a big contingent of the ’top face’ b). The surface contribution study is of special interest considering the results of the analytical calculations shown in section 6.2. The shown analytical model considers the ’inner face’ only. Figure 6.11 confirms that the ’inner face’ contributes mainly to the maximum positive charge alternation, caused by a droplet positioned in between the electrodes (cf. figure 6.10 at t = 2.2 ms). This enables to conclude that small deviations from the alalytical calculations to the results of the numerical simulation might derive from the analytically neglected surface contribution.

6.3.7 Capacitive coupling effect

A quantitative study of the influence of the capacitive coupling effect to the droplet detection method is given in the following. To vary the influence of this effect the average capacitance of the capacitive network, C_{liquid}, C_{Wall} and C_{Solid} (c.f. section 6.3.1; figure 6.5) has to be changed. To implement such changes into the simulation model, the height of the liquid column was changed. An increased height corresponds to a decrease of the average capacitance of the capacitive network. The focus here was on the change of the negative signal drop, generated before the droplet tears off. Especially the influence to the overall maximum change in charge was of interest. The study was performed by the simulation of droplets of identical parameters. Figure 6.12 shows that an increase of the liquid column height leads to a reduction of the negative signal drop. The maximum signal peak value however stays mostly constant. Changes of the height of the liquid column changes the fluidic impedance from the inlet boundary to the nozzle outlet. Therefore slightly different droplets are produced which might be the reason for the different maximum signal peak values. The simulation of an electrically insulated column represented by a height of $h = \infty$, results in the elimination of the negative dip as expected. The minimum value of the negative signal drop is attained at $t = 0.4$ ms for all cases. This is the moment in time when the droplet tears off from the nozzle.

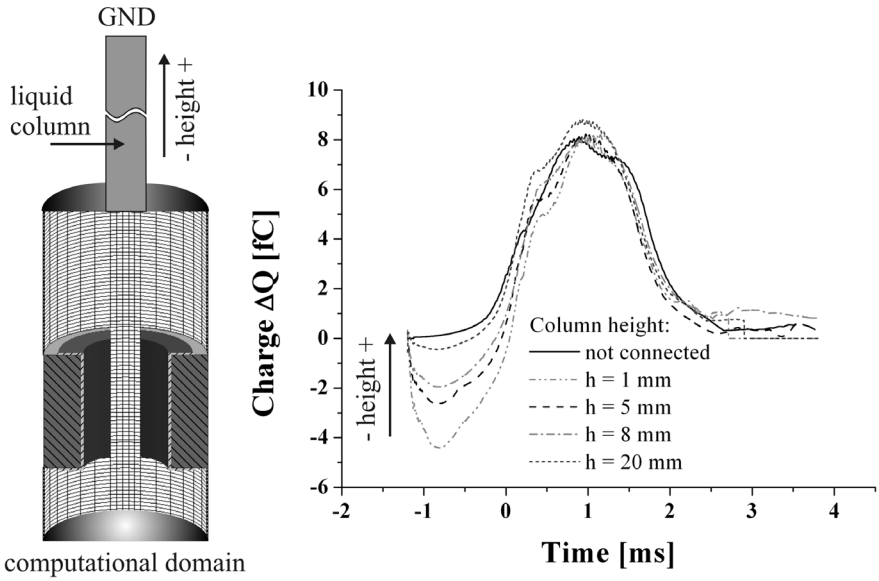

Figure 6.12 Investigation of the influence of the capacitive coupling effect by variations of the liquid column height

6.3.8 Nozzle distance to measurement capacitor

Further investigations regarding the capacitive coupling effect were done by the variation of the distance from nozzle to the measurement capacitor h_{var}. Variations of h_{var} entail different signal characteristics generated by droplets at identical conditions. This can be explained by the fact that droplets dispensed at very large distances tear off from the nozzle before they are exposed to the electric field, whereas droplets at very small distances are exposed to the electric field while they are still connected to the nozzle. As a result, $h_{var} = 0$ can be expected to lead to an increased effect of capacitive coupling, hence larger negative signal dips. To study the effect of variable distance to the nozzle, the computational domain was changed with respect to h_{var}. To increase the said distance multiple layers of cells at constant size were added to the existing domain. Figure 6.13 shows the results of these simulations. A decreasing distance goes along with an more prominent negative peak whereas a minimized positive charge alternation can be observed. A distance of $h_{var} = 250$ µm vanishes the positive signal peak nearly completely, whereas an increased fluctuation of the signal can be observed. Probably, a closer distance exposes the meniscus at the nozzle to an initially stronger electric stray field. Thus, movements of the meniscus might affect the signal more significant than the detached droplet. Again, the identical droplet ejection process, applied for the individual conditions of h_{var} led to an identical moment in time for droplet tear-off, which is the same as before (t = 0.4 ms).

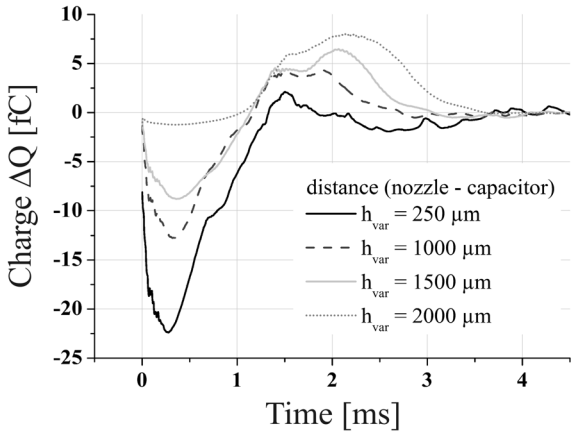

Figure 6.13 Investigation of the influence of the distance from the nozzle to the capacitor

6.3.9 Variations of capacitor geometry

To find the most suitable electrode geometry for the realisation of a droplet sensor different shaped capacitor electrodes were studied by simulation. Therefore, the change of charge could be investigated quantitatively with respect to the specific geometry. The individual geometries were designed with focus on a simple and cost effective fabrication. The considered geometries are depicted in figure 6.14. Whereas geometry a), the 'half shell electrode' arrangement, was used for all previously simulations, the geometries b) 'planar ring electrodes' and c) 'parallel plate electrodes' provide feasible alternatives. While a) and c) differ in the electrode shape only, b) features a different orientation of the electric field which is directed in flight direction of the droplet. In the latter case the droplet influences the stray field only, which distributes into the centre of the ring. Therefore, a low charge alternation is expected. However, this approach presents the simplest alternative regarding the final sensor fabrication. The individual simulations were realised using identical boundary conditions, thus a direct correlation of the maximum change of the charge allows for a quantitative conclusion. The results achieved by this study are given in figure 6.15. From this it can be seen that the geometry of the electrodes is an essential aspect regarding the sensitivity for droplet detection.

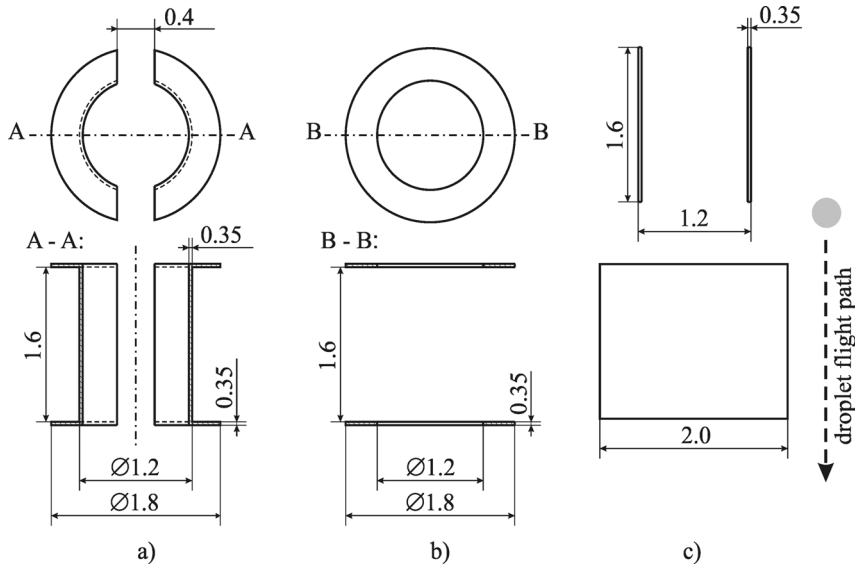

Figure 6.14 Three different studied geometrical electrode arrangements; a) circular shaped half shell electrodes; b) parallel ring electrodes; c) plane parallel electrodes

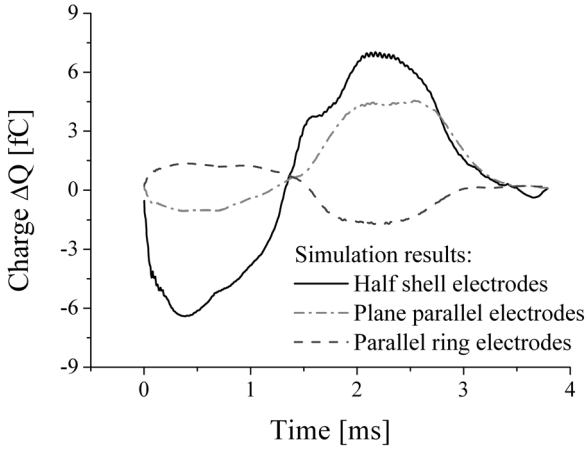

Figure 6.15 Charge alternation caused by a droplet of 33nl volume for the three geometries given in figure 6.14

The half shell geometry led to a maximum change of charge of $Q = 7.1$ fC, whereas the planar plate electrodes entail a maximum charge alternation of $Q = 4.5$ fC. The expected small change for the planar ring electrodes was confirmed to yield $Q = 1.6$ fC only, featuring an inverted signal characteristics. Considering a droplet volume of $V_{drop} = 33$ nl (see section 6.3.3) these results imply sensitivities of: $S_{ia} = 0.22$ fC/nl; $S_{ib} = 0.05$ fC/nl and $S_{ic} = 0.14$ fC/nl respectively. Due to the best sensitivity the half shell electrode arrangement was used for further study.

6.3.10 Variations of the half shell electrode geometry

Further variations of the capacitor geometry were realised considering the electrode's height as well as the position and the width of the electrode separating trench. Variations in the geometrical trench position and width will theoretically entail a change in the electric field which is affected by a passing droplet. Three different trenches were defined to be simulated like shown in figure 6.16. Beside a decrease of a symmetrically set trench's width (a), also the lateral position of the trench was varied (b, c), creating an asymmetric capacitor. This aspect is important for fabrication reasons considering the precision of the milling step to separate the two capacitor electrodes. The extracted charge alternations are given in figure 6.17 by the individual signals. Obviously the asymmetric trenches did not lead to satisfying results. This arises from a shift of the electric field, having the maximal field density shifted towards the measurement electrode.

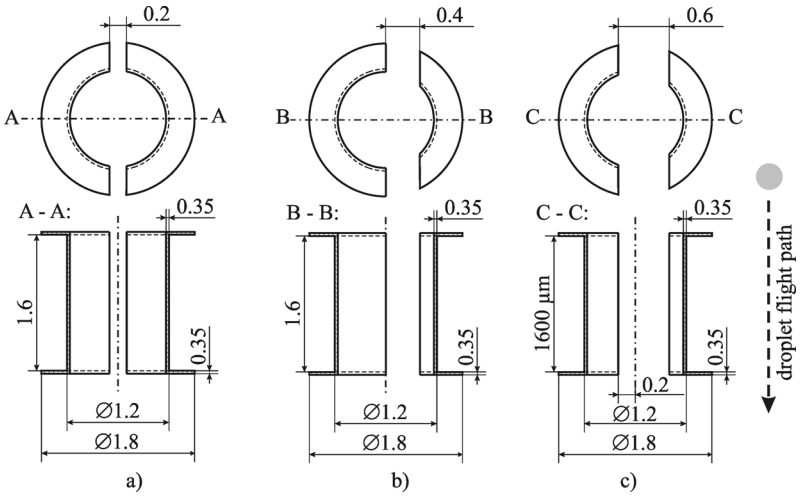

Figure 6.16 Different geometries of the trench, separating the capacitors electrodes, studied by simulation

The droplet does not pass through the area of highest field density, thus lead to lower charge alternation. Also a smaller trench width does not increase the volume sensitivity of the 'half shell electrode' arrangement. The smaller trench did increase the field strength in the area surrounding the trench only. The electric field in the center of the capacitor stays constant compared to the wider trench, thus the effect is not important for the present measurement principle.

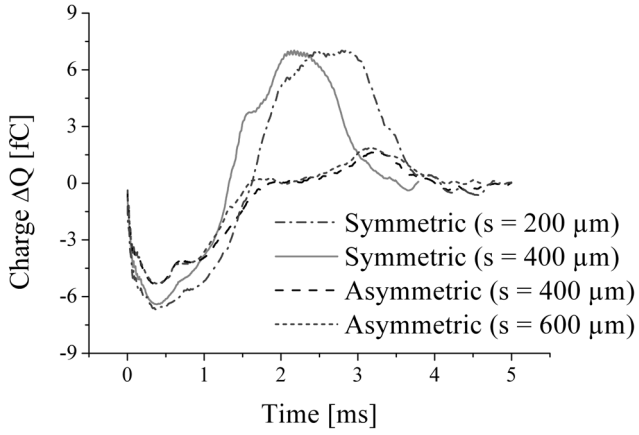

Figure 6.17 Simulation results by the variation of the geometry of the trench, separating the electrodes of the measurement capacitor, cf. figure 6.16.

Due to this results, the ’half shell electrode’ geometry, given in figure 6.14 a), can be taken as favoured geometry for the sensor implementation.

Another considerable geometrical factor, affecting the measurement significance, is the height of the capacitor plates. Therefore, the established computational domain, featuring an initial height of h = 1.6 mm, was changed to a height of h = 3.2 mm and h = 0.6 mm respectively. To realise the geometrical variations, cells of constant size were added to the domain to extend the electrodes height or deleted to decrease it. Figure 6.18 shows that an increased height does not lead to an advanced sensitivity compared to the default value of h = 1.6 mm. It can be seen that the maximum change in charge does not increase beyond the point obtained for h = 1.6 mm. The signal rather builds a plateau due to the longer exposure time of the droplet to the electric field caused by the increased height. A first conclusion allows for the statement that the simulated droplet, including the set boundary and volume conditions reaches the possible maximum change in charge of $Q = 8.4$ fC using the default setup, which cannot be improved by an increase of the capacitors height or increased exposure time through lower droplet velocity. However, shorter electrodes lead to a loss of information and sensitivity by a decrease of the maximum signal peak. Due to smaller electrodes the sensitive area declines as well, thus the droplet is not long enough exposed to the electric field to lead to the maximum change in charge. Considering the simulated droplet velocity of $u_{drop} = 1.4$ m/s as realistic maximum velocity condition, an electrode height of h = 1.6 mm is considered as sufficient for the sensor realisation.

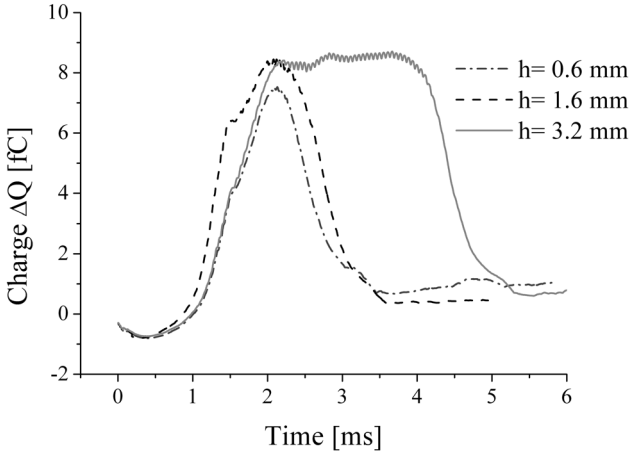

Figure 6.18 Simulation results by the variation of the capacitor height influenced by identical droplets

6.3.11 Influence of droplet volume

The following simulation study is focussed on the effect of variable droplet volume on the charge alternation on the measurement electrode. A first proof of this influence was given in section 6.3.5, figure 6.9. However, the shown results were generated by spherically shaped droplets at constant velocity and shape. The dispensing process as well as the effect of capacitive coupling were not considered. To study the influence of variable droplet volumes including all side-effects, the dispensing process was adapted to enable the generation of droplets of different volumes and velocities. Therefore, the actuation time and velocity of the simulated inlet flow (i.e. the actuation parameter) was varied to create different droplet ejection conditions (cf. section 6.3.3). The individual actuation parameters and the entailed droplet parameters are given in table 6.2.

Table 6.2 Droplet dispensing parameters and resulting droplet properties

actuation parameters		**droplet properties**	
pulse duration [µs]	**flow velocity [m/s]**	**volume [nl]**	**droplet velocity [m/s]**
70	**2.8**	**33**	**1.4**
70	**2.5**	**29**	**1.2**
70	**2.2**	**22**	**1.1**
50	**2.5**	**17**	**0.9**

The change of the charge, caused by droplets which are generated by the application of the listed parameters, are shown in figure 6.19.

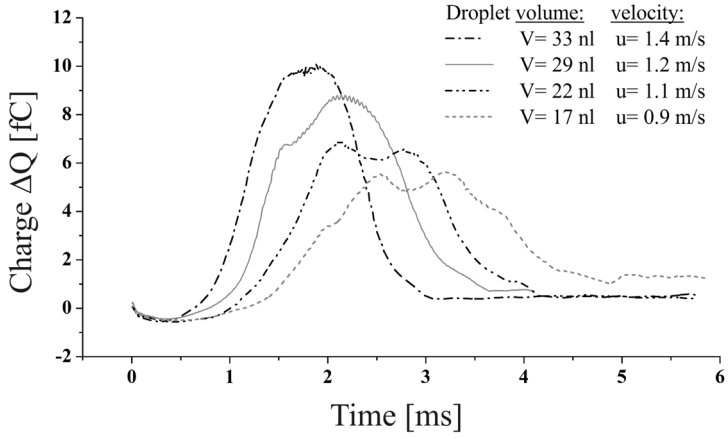

Figure 6.19 Charge alternation induced by dispensed droplets

Obviously, the maximum change in charge decreases with lower droplet volumes like known from the simulations in section 6.3.5. A noticeable detail here is the specific signal characteristics exhibited by the signals generated especially by smaller droplets (V = 22 nl and V = 17 nl). Two signal maxima can be observed, which occur from droplet deformation during the flight through the capacitor. Figure 6.20 shows a dispensed droplet at four time dependent vertical positions. Each position exhibits a specific droplet deformation based on the applied dispensing parameters. Positions 2 and 4 show lateral deformations of the droplet towards the electrodes, entailing an increase of the charge on the measurement electrode. In contrast to this, a longitudinal deformation (position 3) leads to a local decrease of the charge. Thus, movements of the droplet's shape lead to the observed double peak signal characteristics. This behaviour is deducible from Maxwell's first law. The occurrence of multiple signal maxima implies the need for further signal analyses. A value has to be defined which represents the state of a spherical shaped droplet. In fact, a droplet has to assume an almost spherical shape while switching from maximal lateral to maximal longitudinal deformation. Therefore, a good estimate for the required value is given by the mean value of the maximal signal peak and its neighbouring minima.

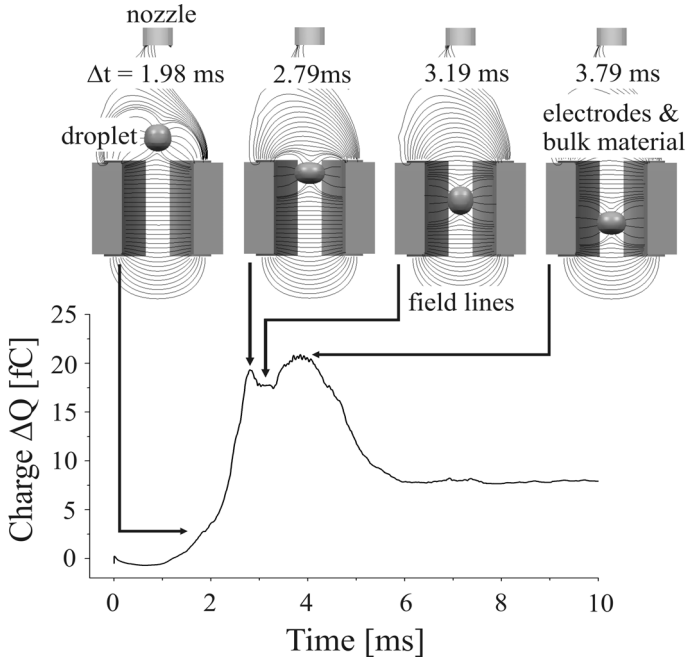

Figure 6.20 Influence of droplet deformation to the resulting charge alternation

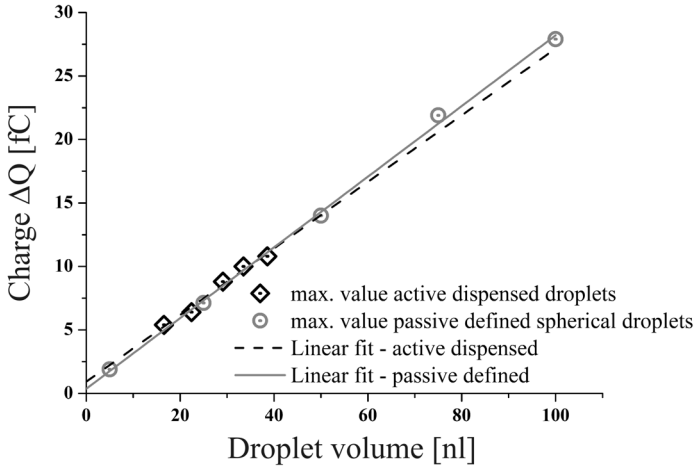

Figure 6.21 Correlation of droplet volume to the corresponding maximum change in charge for the spherical droplets as well as for the dispensed droplets

The quantitative evaluation of the effect of different droplet volumes, velocities and shapes on the maximum change in charge was realised by the correlation of the droplet volumes to the results gained from the simulation of dispensed droplets, see figure 6.21. Furthermore, these results were compared to the change in charge caused by the spherical droplets, shown in section 6.3.5. The results displayed in figure 6.21 show that the droplet volumes correlate in a linear manner with the change in charge. The comparison of the results gained by dispensed droplets, exhibiting deformations in the shape as well as different velocities and those caused by ideal spherical droplets lead to almost identical linear regressions. This enables to conclude that the influence of effects like droplet deformation or capacitive coupling on the droplet volume evaluation based on the capacitive measurement principle are mostly negligible. It can also be seen that variable droplet velocity does not influence the maximum change in charge for the considered geometry and velocity range (u_{drop}< 1.4 m/s).

Comparing the results achieved by the CFD simulation with the analytically calculated capacitance changes led to the results shown in figure 6.22. Therefore, the numerically simulated changes in charge Q had to be transformed to the corresponding capacitance C. The charge values had to be divided by the voltage applied in the simulations $U = 10\ V$ ($C=Q/U$). The values of the analytical calculations and the numerical simulations exhibited significant deviations at first consideration. The simulations do overestimate

the capacity by about 30% compared to the analytical model. However, taking the presented grid refinement study into account (cf. section 6.3.4), the off-set can be attributed to the coarse grid (grid 1) used for the simulations. Assuming a systematic deviation of 29% implied a rescale of the simulated data by a factor of 0.71. The remaining small deviations, which are still present, might occur due to the inhomogeneity of the electric field based on the curved electrodes as well as on the neglection of the effect of the surface electrodes, see chapter 6.3.6, which are not considered applying the analytical model.

The good correlation of the analytically calculated capacity changes and the numerical simulation results suggests that the analytical model as well as the simulation model, including the grid refinement study are consistently describing the considered problem.

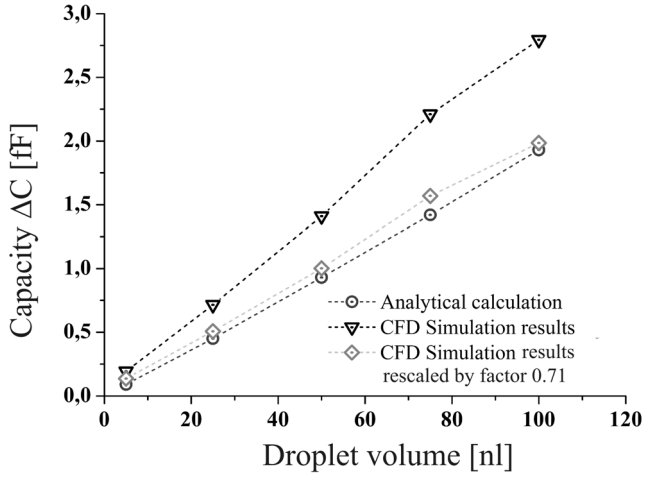

Figure 6.22 Change in capacitance according to the analytical model (equation 6.5) in correlation with the CFD simulated results

Chapter 7
Capacitive droplet detection - implementation and characterisation

The following chapter comprises the design, the fabrication and the characterisation of the capacitive droplet sensor. The sensor implementation is realised by two individual electronic circuitries, differing basically in their front end impedance. Both sensors are realised in printed circuit board technology (PCB) and termed in the following as CS 1 and CS 2. The sensors are characterised with focus on the specific signal characteristics, generated by single droplets which pass through the measurement capacitor.

7.1 Sensor electronics

The content of the following section provides the detailed description of the electronic read out circuitries of the capacitive sensors CS 1 and CS 2. The influence of the front - end impedance is introduced to state the difference of the individual sensor concepts.

7.1.1 Front - end impedance

The electronic transformation of the small changes in capacitance ($\Delta C < 3 * 10^{-15}$ F) to a readable voltage level can basically be realised by several different electronic circuitries. A crucial issue here is the electronic front - end circuitry (front - end), which enables to buffer the low signal currents. The most commonly applied technology is based on high impedance front - ends [89]. Such front - ends consist mostly of voltage follower- or non - inverting amplifier circuits, providing very high input- and low output impedance. Therefore, very low bias currents are realised, enabling the realisation of highly sensitive amplification circuits to very small signal currents. However, the realisation of high impedance front - end circuitries requires the use of high performance components, increasing the fabrication costs. Another critical issue is the required implementation of a 'driven guard ring' to shield the capacitive transducer from environmental influence. Closer explanation on this is given in section 7.1.2. Furthermore, these front - ends suffer from major disadvantages like temperature dependency and high noise. A different design for the read out circuit is based on the application of a low impedance front - end. Low impedance front - ends can be realised applying an inverting amplifier used as input buffer. A considerable advantage for the application of an inverting amplifier is the virtual connection to ground potential, which simplifies the shielding of the transducing unit enourmously

[90], see also section 7.1.2. Furthermore, low impedance front - ends reduce parasitic capacitances, which are often in the order of magnitude of the capacitance of the measurement capacitor [91]. Low impedance front - ends can be realised by the use of cheap standard components. This implies a feasible realisation of low cost sensor devices.

As consequence of pro's and con's, two different read out circuitries are established to investigate the advantages and disadvantages of a low- respectively a high impedance front - end. An essential detail, which has to be considered for both approaches, is the shielding of the capacitive transducer to reduce environmental influence on the sensor performance.

7.1.2 Guardring technology

The transformation of very small changes in capacitance, which implies the handling of very small signal generating currents, requires obviously high sensitive read out circuitries. These circuitries are sensitive to the desired input signals as well as highly susceptible to external influences like leakage currents and parasitic capacitances. To interrupt such external failure sources a shielding of the capacitive transducer has to be implemented realised by a so called guard ring. A guard ring is realised by a conductive ring or area surrounding the transducing unit (here the measurement capacitor), acting as a third electrode. The guard ring has to be connected to a specific low impedance section of the circuitry, which is at the same potential as the input signal [92]. Bulk or surface leakage currents are absorbed by the guard ring, thus they can not affect the measurement. The guard ring connection to the circuit differs for individual front end principles and has to be adapted to the applied measurement method. The required guard ring circuit block diagrams for the applied front - end principles in this work are given in figure 7.1.

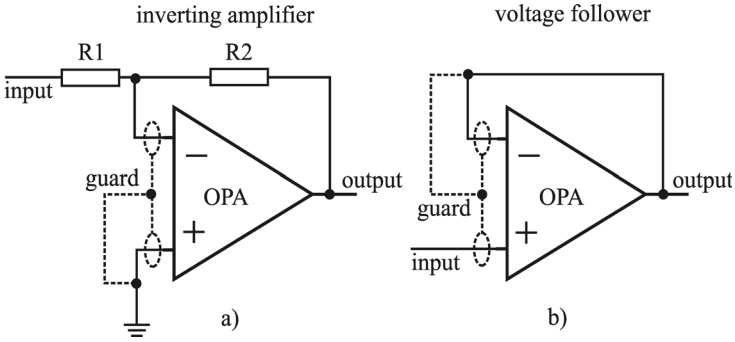

Figure 7.1 Different guarding principles. a) guarding of a low impedance front end; b) guarding principle for high impedance front end

One of the presented sensor read out circuits features an inverting amplifier as low impedance front end, thus the necessary guard ring can be simply connected to ground potential (figure 7.1 a). A more complex guard ring technique is required in terms of the used high impedance front end, consisting of a voltage follower as input buffer. Here, the guard ring has to be realised as a so called 'driven shield', connected to the output potential of the buffer which changes with respect to the input signal, see figure 7.1 b) [92].

7.1.3 Sensor supply electronics

The capacitive measurement principles are based on the AC modulation of the measurement capacitor by an alternating voltage. Therefore, an analogue sine wave has to be generated, which is realised by the monolithic function generator XR2206 SOIC from EXAR [93]. The supply frequency of f_{supply} = 160 kHz was identified by the experimental determination of the circuit's resonance frequency. The generated sinewave is post amplified by a standard inverting amplifier circuit, consisting of a TL081 OPA to the supply voltage amplitude of U_{pp} = 20 V. Furthermore, the positive and negative supply voltage required for the functionality of the active sensor components are generated by a DC/DC converter type NMA4815 from C&D Technologies [94]. A summing amplifier circuit enables an offset regulation of the sensor signal by the addition of an adjustable DC voltage to the signal. The sensor supply board is the only external device which is required to drive the sensors.

The following sections (7.1.4 and 7.1.5) present the block diagrams of the established electronic read out circuitries. The different sensor approaches will be termed 'capacitive sensor type 1 (CS 1)' and 'capacitive sensor type 2 (CS 2)' throughout this work.

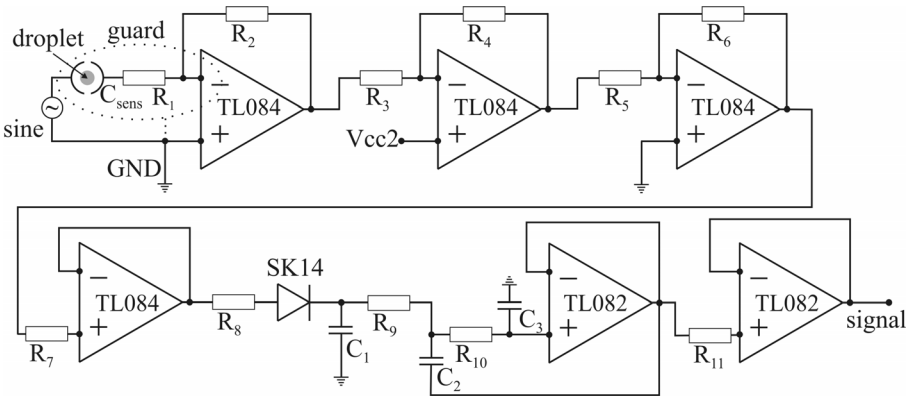

Figure 7.2 Complete electronic sensor read out circuit of CS 1, featuring a low impedance front end.

7.1.4 Electronic read out circuit - CS 1

The first sensor approach is based on the idea to realise a very simple, straight forward amplification circuit, to investigate the feasibility of extracting very low input changes at low cost. The realisation is focussed on reduction of the number of electrical components and the use of cheap standard electronic parts.

The front - end of the electronic amplification circuit of the capacitive sensor type 1 (CS 1), shown in figure 7.2, consists of an active high pass filter circuitry, featuring a low impedance inverting amplification front - end. Therefore, an easy guarding to ground potential can be realised (c.f. figure 7.1). The measurement principle of CS 1 is based on the gain response of the active high pass filter circuit, which includes the measurement capacitor as consistent component. A change of the measurement capacitance entails a shift in the gain-response of the filter, thus the magnitude of the passing sine amplitude changes in relation to the change in capacity C_{sens}. The transfer function of an inverting high pass filter is given by equation 7.1 [95]:

$$F_{(s)} = \frac{-\frac{R_2}{R_1}}{1 + \frac{1}{\omega_g \cdot R_1 \cdot C_{Sens}} \cdot \frac{1}{s}} \tag{7.1}$$

Further, the amplitude changes are post amplified with respect to V_{cc2} (c.f. figure 7.2), which enables the implementation of a DC offset to the sensor signal. The necessary high total amplification is separated into three successive amplification steps to work in the range of the given gain-bandwidth product of the used OPA (TL084 - unity gain bandwidth 3 MHz). Thereafter, the signal is rectified by a simple diode rectification using a standard diode SK14 from Taiwan Semiconductor and finalised by an active low pass filter, featuring a cut off frequency of f_g = 1 kHz to delete the noise overlaying the rectified signal. The generated analogue signals are digitised by an external A/D converter board from Meilhaus (ME-Jekyll ME-4610) for further signal analyses [96].

The performance of the electronic circuit of CS 1 was investigated by a numerical simulation study using the computational network simulation tool Saber from Synopsis [97]. The simulation was realised applying an amplitude of U_{max} = 10 V at a sine frequency of f = 160 kHz. The active component supply was U_{sup} = ± 12 V, whereas the offset voltage was Vcc2 = 39 mV. A guardring was not considered for simulation. The focus of the simulation was on the amplification of the very small changes in capacity taken from the

numerical and analytical studies. The initial capacitance was set to C_{sens} = 17 fF and varied in the range from C_{sens} = 17 - 20 fF by variation steps of ΔC = 0.5 fF. As a result of the simulation study, the sensitivity of the readout circuit, regarding the generated voltage change induced by changes in the measurement capacitor C_{sense} could be identified to be S_i = 178.7 mV/fF.

The component values applied for the simulation study as well as for the realisation of CS 1 are given in the following table:

Table 7.1 Component details - sensor CS 1

Index	Value	Index	Value	Index	Value
R_1	100 kΩ	R_6	6.8kΩ	R_{11}	1 kΩ
R_2	330 kΩ	R_7	1 kΩ	C_1	10nF
R_3	1 kΩ	R_8	1 kΩ	C_2	22 pF
R_4	10 kΩ	R_9	1 MΩ	C_3	47 pF
R_5	1 kΩ	R_{10}	3.3 MΩ		

7.1.5 Electronic read out circuit - CS 2

The second sensor approach features a high impedance front end, implemented by a voltage follower which acts as input buffer (c.f. figure 7.3, ①).

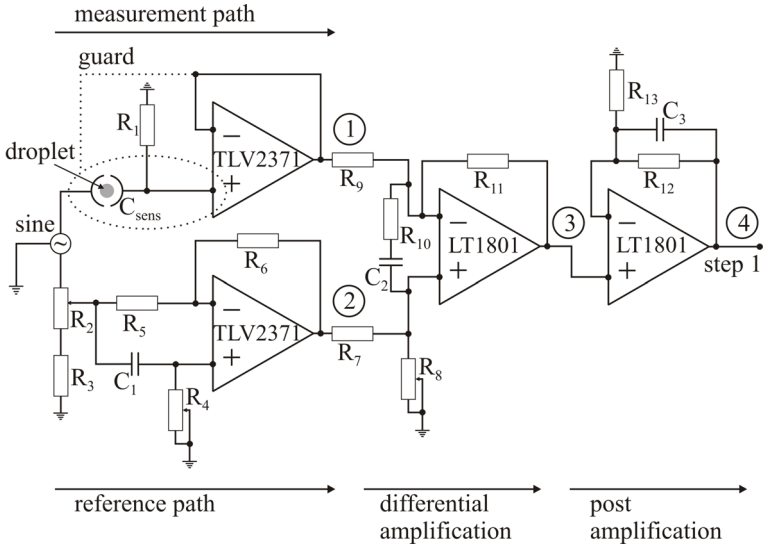

Figure 7.3 Electronic read out circuit of CS 2 - step 1 - measurement and reference path, differential amplification and post amplification.

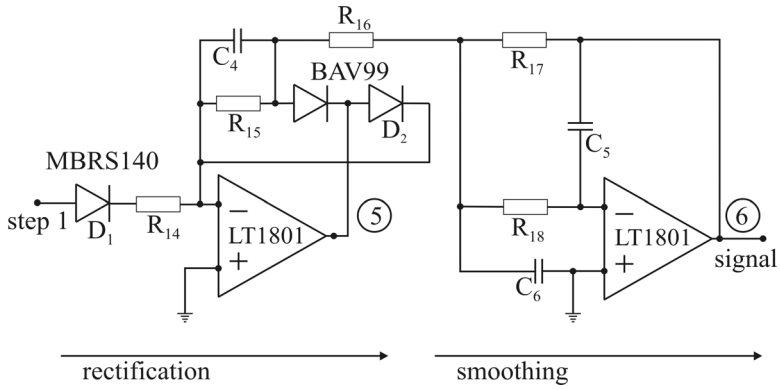

Figure 7.4 Electronic read out circuit CS 2 - step 2 - rectification and smoothing.

The measurement method applied for the realisation of CS 2 is based on a capacitive measurement bridge [98]. Basically, a measurement bridge is sensitive to changes of a measurement signal compared to a defined reference signal. A crucial requirement is the initial analogy of these signals to neglect a systematic offset (zero offset) of the measurement system. In the present case the two signals are fed to an differential amplifier at position ① and ②, see figure 7.3. These signals result from the measurement path and the reference path shown in the block diagram. The measurement path consists of the measurement capacitor C_{sens} and the voltage follower representing the high impedance front - end. The reference path is realised by the combination of an analogue adjustable voltage divider and an all-pass filter. This circuit enables to modulate the signal at ② in phase and amplitude to replicate the initial signal of the measurement path at ①. Therefore, a zero offset, thus a calibration of the sensor can be realised by the regulation of the resisitve potentiometers R_2 and R_4 (c.f. figure 7.3). The following differential amplification step amplifies differences in the signals at ① and ②. Therefore, changes in the measurement signal, caused by the presence of a droplet in the measurement capacitor, are extracted to generate the sensor signal (pos. ③). The post amplification enlarges the signal's amplitudes to a readable voltage level. The resulting signal (pos. ④) is processed by the rectification and smoothing circuit shown in figure 7.4. A high performance full wave rectification featuring two diodes is combined with an active low pass filter circuit with multiplexed degenerative feedback. The performance of CS 2 was evaluated by a Saber network simulation considering exactly the shown circuit. The simulation was realised, applying variable capacities for C_{Sense} (C_{Sense} = {17 to 25 fF @ ΔC = 0.5 fF}), a supply amplitude of U_{max} = 10 V at a sine frequency of f = 160 kHz. The active component were supplied by U_{sup} = ± 5 V. The

applied conditions resulted in a circuit sensitivity to changes in the measurement capacitance of C_{sense} S_i = 1858.15 mV/fF.

The detailed component values used for the simulation study as well as for the sensor implementation are given in the following table:

Table 7.2 Details of the electrical component details used for sensor CS 2

Index	Value	Index	Value	Index	Value
R_1	1 MΩ	R_6	680 Ω	R_{11}	4.7 kΩ
R_2	0 - 5 kΩ	R_7	1.6 kΩ	R_{12}	4.7 kΩ
R_3	180 Ω	R_8	0 - 5 kΩ	R_{13}	1 kΩ
R_4	0 - 1 kΩ	R_9	1.6 kΩ	R_{14}	1 kΩ
R_5	680 Ω	R_{10}	233 kΩ	R_{15}	4.7 kΩ
R_{16}	4.7 kΩ	C_1	10 nF	C_4	168 pF
R_{17}	11.3 kΩ	C_2	276 pF	C_5	100 pF
R_{18}	37.4 kΩ	C_3	168 pF	C_6	390 pF

7.2 Sensor fabrication

The capacitive droplet detection method requires an open measurement capacitor which allows a droplet to pass through without of contact to the electrodes. A crucial issue is the implementation of such a capacitor. The most efficient capacitor shape with respect to the measurement of liquid droplets is a cylindrical half shell electrode arrangement, which was a result of the CFD simulation study. A similar geometry was applied in [88], were the growth of a pending droplet introduced in between two electrodes was measured to evaluate the liquid flow supplying the droplet. To avoid high costs and complex fabrication steps for the manufacturing of vertical half shell electrodes a feature of the printed circuit board technology was used to fabricate the measurement capacitor: A simple through connection (via) is symmetrically separated by a standard mechanical milling process to create the two opposite half shell electrodes, see figure 7.5. The electrodes are connected to the electronic circuit, which is implemented on the same PCB, by standard strip lines. PCB vias can be placed on at any position, in any size without additional costs. The diameter of the capacitor is adapted to the size of the defined maximal measurable droplet volume of V_{max} = 100 nl, which corresponds to a droplet diameter of d_{max} = 576 µm. To prevent the capacitor plates from wet contamination by malfunctions in the dispensing process, like

splitting of the droplets into several satellites or deviations in the droplets flight path, a safety margin of 200% is considered, thus the final capacitor diameter was defined to be $d_{cap} \approx 1.2$ mm. The trench width, separating the electrodes, was defined to be $w = 400$ µm, due to the availability of milling tools. The electrodes height was defined by the thickness of a standard PCB of $s = 1.6$ mm in addition of the thickness of the conductive copper layers ($s_{copper} = 35$ µm), forming the via on top and bottom of the PCB, thus the electrodes height was $h = 1.67$ mm. The realized geometry of the measurement capacitor like shown in figure 7.5, complies well with the preferred geometry identified by CFD simulation (c.f. figure 6.14 a)). The monolithic implementation of the complete sensor circuitry using PCB technology allows for a very easy, flexible, robust and cost effective realisation of the entire sensor. It also facilitates an easy adaption of the sensor unit to any kind of non contact dispensing system by simple adaption of the sensor PCB's geometry. The different sensor circuits (CS 1 and CS 2) are adapted to different types of the PipeJet™ dispenser family, see chapter 4. Whereas CS 1 is adapted to a PipeJet™ P18 module, CS 2 is fabricated for the application with a PipeJet™ P9 module. This yields different outline geometries for the different sensors (c.f. figure 7.5). This purpose is based on historical background of the dispenser development. The prototype of CS 1 was developed and fabricated before the availability of the PipeJet™ P9 module. Thus CS 1 is adapted to the PipeJet™ P18 module which was the only available dispenser featuring the high adjustability.

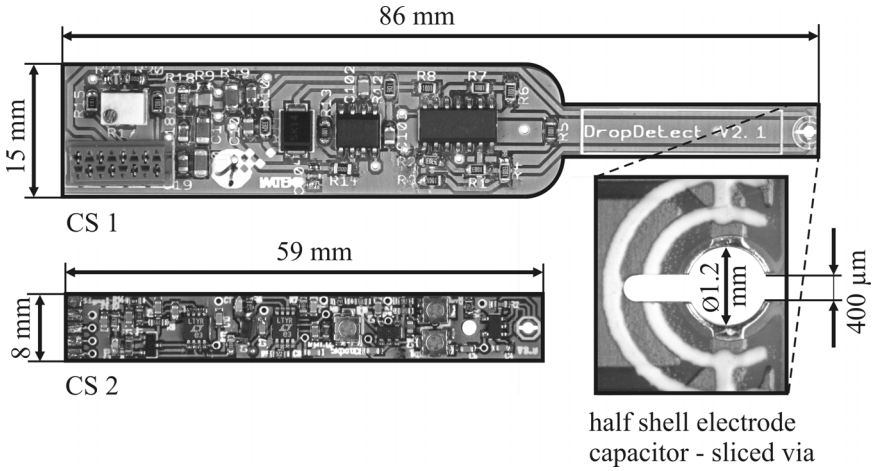

Figure 7.5 Populated sensor circuit boards (PCB) CS 1 and CS 2, drawn to scale and enlarged measurement capacitor made of a standard through connection (via) sliced by mechanical milling.

Since the release of the PipeJet™ P9 module by BioFluidix GmbH in 2008, the development of CS 2 was focussed on this latest module. This implied further miniaturization of the sensor due to the smaller outline of the PipeJet™ P9 module. The developed sensor PCBs are shown in figure 7.5. The figure includes an enlarged sectional view of the half shell electrode measurement capacitor manufactured by the separation of a standard through connection. The layout of the sensor PCBs are designed using the TARGET 3001! V13 professional software [99] and are fabricated by PCB-Pool [72]. The separation of the through connection required an additional fabrication step, since the small trench width could not be realized during the PCB fabrication. The separation process was performed by a subcontractor applying standard mechanical milling [101]. The final population of the sensor PCBs was accomplished in the lab of the IMTEK manually by conventional SMD reflow soldering.

7.3 Cost considerations

The following section provides an insight into the cost structure for the sensor fabrication and the components to emphasize the phrase 'low cost' to the sensor development in contrast to the introduced state-of-the-art techniques. The cost calculation, including the costs for all external work and electrical components, is given for the different sensors types respectively in table 7.3 (CS 1) and table 7.4 (CS 2). Here, the internal lab work at IMTEK is seen as research effort and is not considered for the cost calculation.

Table 7.3 Calculation of the external costs for one sensor PCB type 1

Part	**Component**	**Number**	**Price**	**Sum**
TL084	SOIC 14	1	0.53€	0.53€
TL 082	SOIC 8	1	0.35€	0.35€
Resistor	0805	11	0.09€	0.99€
Capacitor	0805	7	0.06€	0.44€
Diode	SK14 SMB	1	0.18€	0.18€
Fabrication	**Who**	**Number**	**Price**	**Sum**
Sensor-PCB	PCB-Pool	1	~10.00€	10€
Separation	Behrendt	1	3.9.€	3.9€
			Final costs*: 15.70€	***without assembly costs**

Table 7.4 s

Part	Component	Number	Price	Sum
TLV2371	SOT23-5	2	1.27€	2.54€
LT1801	MSOP8	2	4.62€	9.24€
Resistor	0603	12	0.04€	0.48€
R-Poti	3203	3	1.05€	3.15€
Capacitor	0603	10	0.02€	0.20€
Diode	BAV99	1	0.15€	0.15€
Diode	MBRS140	1	0.24€	0.24€
Fabrication	**Who**	**Number**	**Price**	**Sum**
Sensor-PCB	PCB-Pool	1	~8.00€	8.00€
Separation	Behrendt	1	3.90€	5.00€
			Final costs*: 27.90€	***without assembly costs**

These cost calculations led to a ratio of 0.56 comparing the fabrication costs of CS 1 and CS 2. Concerning the electronic parts, CS 1 can be fabricated at approximately the half costs of CS 2. However, the costs for the individual parts depend on the number of units, hence the given ratio is an estimate for a single sensor fabrication only [100].

7.4 Characterisation of sensor CS 1

The experimental characterisation of the capacitive droplet sensors was realised by the measurement of dispensed droplets of variable volume, velocity, shape and liquid properties. To extract and quantify the results, a measurement set up is required, which enables to correlate the volumes of the individually dispensed droplets to the sensor generated data. This was realised by the application of a high precision balance to determine the volume of the dispensed droplets as reference value. A stroboscopic camera enabled to record the droplets at defined, time dependent vertical positions relative to the sensor electrodes. The focus of the sensor characterisation is dedicated to quantitative droplet property measurements like the evaluation of droplet volume or velocity. Furthermore, the influence of the relative permittivity of the sample media as well as the effect of variable lateral droplet position in between the electrodes are studied.

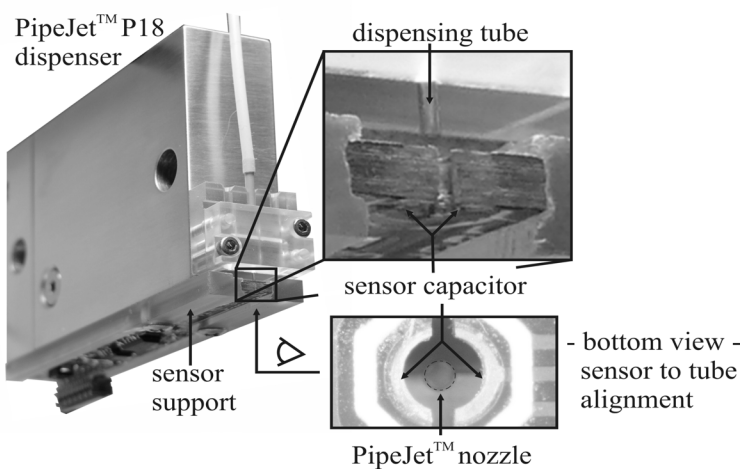

Figure 7.6 PipeJet™ P18 module with sensor underneath, including enlarged sectional view of the dispensing tube to sensor alignments.

To perform the characterisation experiments the sensor CS 1 was mounted underneath a PipeJet™ P18 module using a specific sensor holder which was designed to align the dispenser nozzle centrically to the measurement capacitor (c.f. figure 7.6). The holder was screwed to the lower surface of the sensor and allowed for an easy assembly of the sensor PCB to the dispenser. This setup led to a distance from the dispenser nozzle to the measurement capacitor of d = 1.4 mm. Another issue, which has to be considered by the assembly is the shielding of the sensor electric circuit, see section 7.1.2. Beyond the guard ring implemented on the sensor PCB, the complete aluminium dispenser housing was connected to the guard potential (at CS 1 a connection to GND = 0 V is required). This technique enabled to discharge induced parasitic electric fields caused by the high voltage actuation of the piezo electric dispenser.

7.4.1 Investigations on typical signal characteristics

In first instance typical sensor generated signals were correlated to several corresponding, time dependent vertical positions of the droplets. An example is given in figure 7.7. It illustrates a sensor signal, generated by a pure water droplet which passed the measurement capacitor. The signal is correlated to three characteristic droplet positions during the flight through the sensor. These positions define significant characteristics of the signal, indicated by the points in time t_0, t_1 and t_2. The initial negative peak at the beginning of the

signal (t_0 to t_1) indicates for an approaching droplet described by the capacitive coupling effect. The droplet is still connected to the dispenser nozzle (c.f. the first image in figure 7.7) until the most negative peak U_{min} is reached. This is the moment when the droplet tears off from the nozzle like studied in section 6.3.7. Considering the given conditions, this point t_1 can be taken as entrance of the droplet in the measurement capacitor. The magnitude of the negative amplitude U_{min} depends on geometrical parameters like distance of the nozzle to the measurement capacitor in combination with the applied dispensing parameters. The generation of the negative signal peak was studied in section 6.3.7 by the use of the CFD model. Further experimental evaluations on this were not accomplished. The following signal raise is caused by a droplet which detached from the nozzel and passed the capacitor as free flying droplet (t_1 to t_2). In this phase the droplet can be seen as a dielectric body which leads to an increase of the average capacitance of the measurement capacitor. This implies an increase of the sensor voltage signal to U_{max}. The maximum amplitude U_{max} is reached when the droplet is about to leave the measurement capacitor (c.f. figure 7.7 - t_2). The magnitude of the voltage increase to U_{max} depends on several parameters like droplet volume, droplet velocity and liquid type, which is studied in the following in more detail. The time interval from t_1 to t_2 can be taken as the time of flight (ToF) of a droplet through the measurement capacitor. At time $t > t_2$ the signal decays to its initial value with a certain time constant, defined by the specific amplification circuit of CS 1 and is not affected by any droplet parameters.

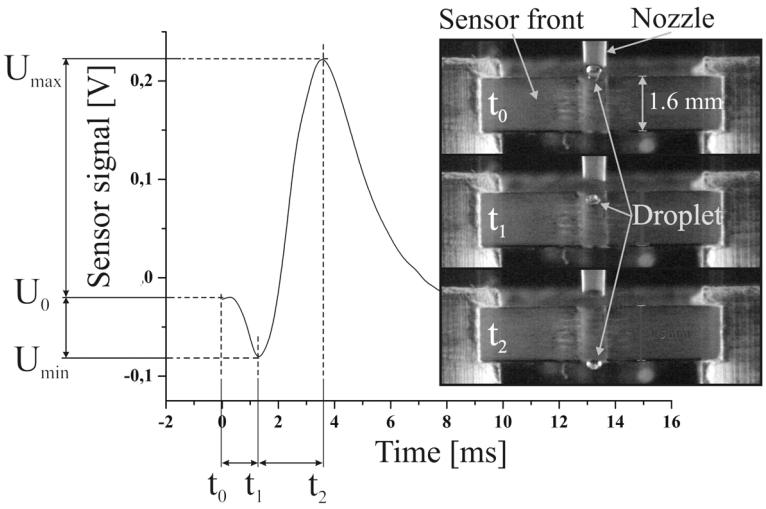

Figure 7.7 Typical analogue sensor signal correlated to specific, time dependent droplet positions illustrated in the stroboscopic images.

7.4.2 Influence of droplet volume at constant velocity

The study of the influence of the droplet volume to the sensor performance was realised by the measurement of several pure water (DI/ de-ionized) droplets of variable volume. The droplets were generated by the PipeJet™ P18 dispenser and shot through the measurement capacitor. The dispenser actuation parameters were adjusted to vary the droplet volumes at constant droplet velocity, see chapter 4. Five measurement series of 100 single droplets each, at target volumes of V_{drop} =25, 35, 45, 55 and 60 nl were performed to study the influence of the variable droplet volumes to the sensor generated signals. Figure 7.8 shows four sensor signals generated by droplets of V_{drop} = 34, 42, 56 and 70 nl representing the gained results. It can be seen that the fundamental signal shape stays constant. The signal peak value changes with different droplet volumes only. Obviously, there is a significant correlation between the maximum signal peak values and the corresponding droplet volumes. The signal peak value of each recorded signal was determined and correlated to the volume of the corresponding signal generating droplet. Figure 7.9 displayes the signal peak value as function of the droplet volume. The linear fit was calculated based on the recorded data and can be seen as a first calibration for the sensor. It quantifies the correlation of signal peak value to droplet volume at constant droplet velocity and led to a coefficient of determination of $R^2 = 0.993$. For the determination of the predictive accuracy of the fit, an error assessment was performed by statistical interval estimation. The boundaries of the calculated prognosis interval featuring an error probability of 5% are illustrated in figure 7.9 as grey, dashed lines. This interval signifies that 95% of all droplets of a given size will entail the generation of peak values within the indicated limits.

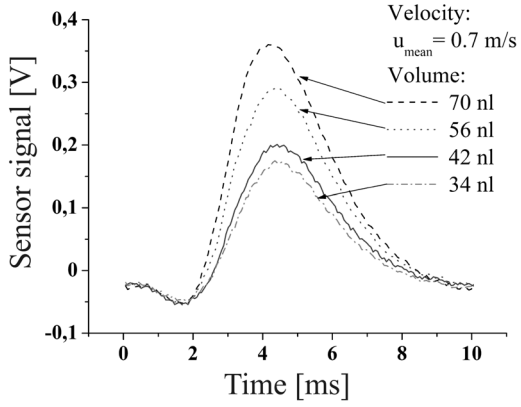

Figure 7.8 Sensor signals generated by droplets of different volumes dispensed at constant velocity.

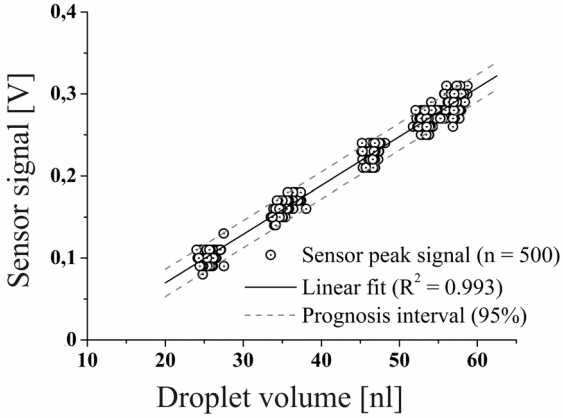

Figure 7.9 Correlation of the signal peak values generated by droplets of variable volumes and constant velocity to the corresponding droplet volume measured by a balance.

This first quantitative evaluation enables the determination of the volume of single dispensed droplets in the volume range V_{drop} = {25 to 60 nl} with an accuracy of $\Delta V = \pm 2$ nl for water droplets of constant velocity. The droplet velocity for this measurement was estimated by the application of a stroboscopic camera and identified to be $u_{drop} \approx 0.7$ m/s.

7.4.3 Influence of variable droplet velocity

Further investigations on the sensor performance were focussed on variable droplet velocity. It turned out that the droplet velocity has a significant impact on the measurement results. Therefore, the influence of variable droplet velocity was studied in detail like given below.

The examination of sensor signals generated by droplets of equal volumes ($\Delta V_{max} = \pm 5$ nl) at different velocities $u_{droplet}$ = {0.5 to 1.5 m/s} has shown that the signal peak values decrease with increasing velocity [102]. This impact was examined by further experimental studies. A considerable detail is the influence of droplet deformation on the change in capacity, known from the simulation study in section 6.3.11. To avoid falsifying influence on the signals, it was aspired to study the velocity impact by the application of identically shaped droplets at equal volumes and variable velocity. The PipeJet™ dispenser, used to generate the droplets enables to adjust the velocity and volume of the droplets by variation of the driving parameters. Nevertheless, it entails an arbitrary deformation of the droplets which increases especially for higher droplet velocity.

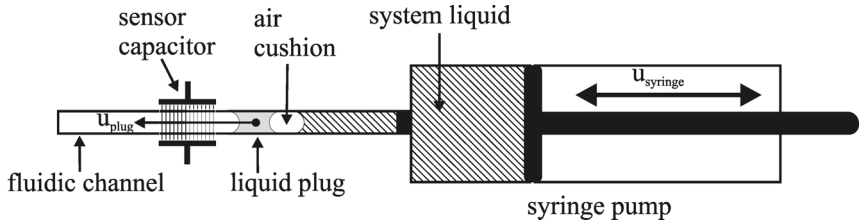

Figure 7.10 Principle sketch of the experimental set up for the evaluation of the velocity impact to the sensor performance

To cope with the requirements for the planned experiments a different experimental setup was assembled, enabling the measurement of a liquid plug of constant volume and shape at variable velocity. Figure 7.10 shows a sketch of the applied measurement setup. A micro fluidic channel with an inner diameter of ID = 500 µm was inserted in between the electrodes of the measurement capacitor of CS 1. A liquid plug consistent of pure water (V_{plug} ~ 200 nl) was introduced in the channel and moved through the measurement capacitor's electric field. This setup guarantees a constant shape of the liquid plug while moving through the channel. Small, but negligible deformations are expected caused by contact angle hysteresis. This entails deformations of the menisci of the liquid plug caused by pinning at the side walls of the channels. This effect was minimized by a hydrophobic coating of the inner walls of the channel using a PTFE solution [103].

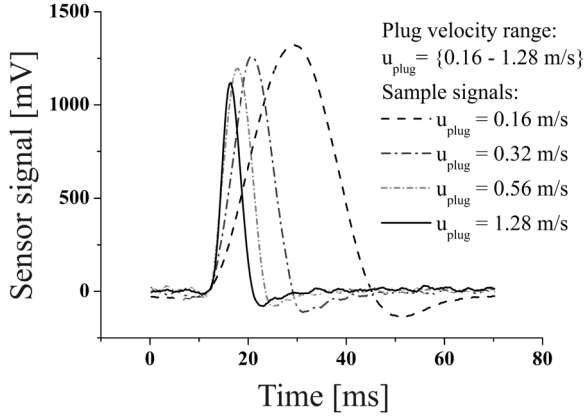

Figure 7.11 Evaluation of the velocity impact on the sensor performance of CS 1; Four sample signals, generated by one liquid plug at different velocities (liquid volume V ~ 200 nl).

The initial signal offset caused by the inserted channel material (polyimide (PI)) into the measurement capacitor could be leveled by the provided offset regulation. Therefore, the channel material did not affect the absolute signal change. The liquid plug was moved by a high precision syringe pump [104], which enabled a highly precise adjustment of the liquid plug velocity. To avoid uncontrollable bucking movement of the plug caused by compression/ decompression effects inside the syringe system, a non compressible fluid (H_2O) was used to act as system liquid. For the investigation of the velocity impact the liquid plug was moved at variable velocity u_{plug} = {0.16 to 1.46 m/ s} through the sensor. Figure 7.11 illustrates four individual sample signals, representing the complete measurement series. It can be seen that the signal characteristics change in shape and amplitude with variable velocity at constant volume. The results were quantified by the correlation of the signal peak values and the corresponding plug velocity, like shown in figure 7.12. Obviously, the velocity influence to the performance of CS 1 exhibits a linear behaviour, which is numerically retained by the linear fit based on the experimentally determined values. The relation of velocity and sensor peak value at constant droplet volume is represented by the velocity factor f_{vel} = -0.18 Vs/m, gained from the slope of the linear fit. Further studies on the droplet velocity impact have shown that liquid quantities of different volumes in the considered range led to the same velocity factor f_{vel}, see [102].

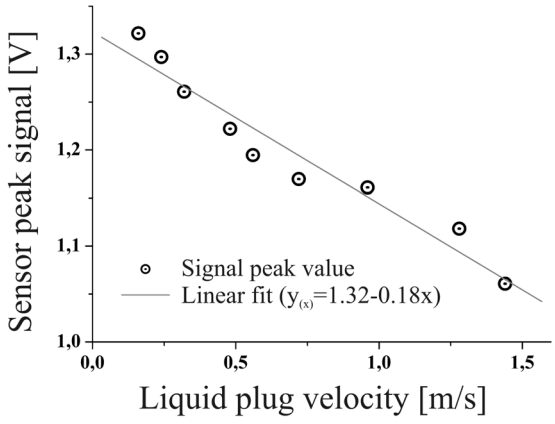

Figure 7.12 Evaluation of the velocity impact on the sensor performance; Correlation of the signal peak values to the corresponding plug velocity, generated at constant volume (liquid volume V ~ 200 nl);.

Based on this result an equation could be deduced which enables to compensate the velocity influence by extrapolation to an imaginary zero velocity u_{drop} = 0 m/s, considering the specific factor $f_{vel:}$

$$U_{u_0} = U_{max} + f_{vel} \cdot u_{drop} \tag{7.2}$$

The shown linear behaviour with respect to U_{max} and u_{drop} lead to the conclusion that wide band measurement which includes droplets of variable volume as well as unknown velocity can be realised considering both values in a three dimensional, linear calibration function like follows:

$$V_{droplet} = C_1 \cdot U_{max} + C_2 \cdot u_{drop} + C_3 \tag{7.3}$$

where U_{max} is the signal peak value, u_{drop} the droplet velocity and the factors C_1 to C_3 are the required calibration values.

7.4.4 Determination of the droplet velocity

The application of the calibration function equation 7.3 implies to know the velocity of each measured droplet. Therefore, a proper online velocity determination method for each single droplet is required. To avoid external measurement equipment it is prefered to determine the velocity by the capacitive sensor as well. Contemplating figure 7.7 it is obvious that an estimate for the droplet velocity can be taken from each generated sensor signal individually. This can be implemented analysing the negative signal peak at t_1 which is an approximation for the droplet entrance in the measurement capacitor and the signal peak value at t_2 which defines the droplet's exit of the sensor capacitor. The well known capacitor thickness (s = 1.675 mm) enables the calculation of the average velocity u_{drop} considering the time of flight given by the two signal extrema at t_1 and t_2:

$$u_{drop} \approx \frac{s}{(t_2 - t_1)} \tag{7.4}$$

To proof the applicability of equation 7.4 for the implementation of the calibration equation 7.3, a validation study was performed to identify the accuracy of the established velocity estimation method. Several droplet velocities calculated according to equation 7.4 were correlated to the corresponding reference velocities determined by the evaluation of individually recorded stroboscopic image sequences. The measurement of the droplet velocity using an image series taken by a stroboscopic camera, is realized by the determination of the distance which is covered by the

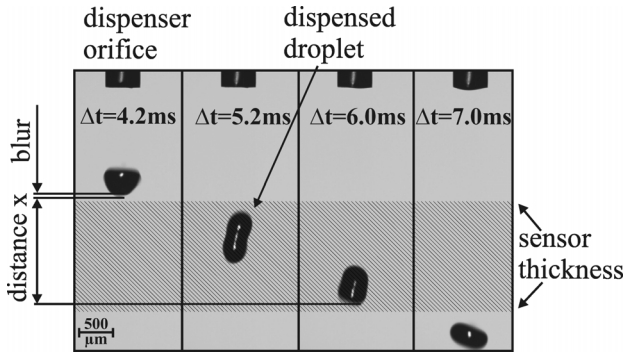

Figure 7.13 Illustration of the stroboscopic droplet velocity determination method. The hatched area indicates for the area of the measurement capacitor.

monitored droplet's leading edge related to the time it needed to traverse this distance. An example for the stroboscopic velocity determination is given in figure 7.13. The distance x, which the droplet passed in the illustrated time interval ($\Delta t = 1.8$ ms) gives an accurate value for the droplet's head velocity ($u_{strobo} = x/\Delta t$). The error for this measurement can be estimated by the size of the blur surrounding the droplet image. Additionally, an error of $t_{err} = 0.1$ ms is considered as measurement uncertainty due to the shutter time of the used camera [105]. Furthermore, figure 7.13 depicts the deformation of a droplet during it's flight, which contributes to the measurement error. The droplet deformation increases for higher droplet velocity caused by the required high velocity of the piezo extension to generate fast droplets.

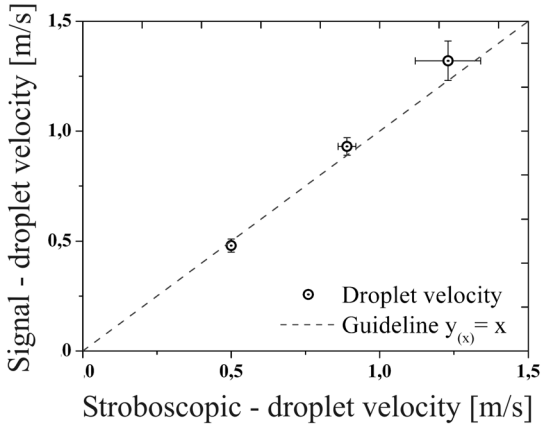

Figure 7.14 Droplet velocity estimation; Correlation of the sensor estimated droplet velocity according to equation 7.4 to the corresponding stroboscopic measured droplet velocity

Hence, the velocity error implied by the measurement of fast droplets increases.

The results achieved by the velocity estimation experiment are shown in figure 7.14. The dashed line represents an ideal correlation based on the function $y_{(x)} = x$ acting as a guideline to the eye. It supports the reader to intensify the correlation accuracy of the droplet velocity estimation which led to a coefficient of determination of $R^2 = 0.99$. Obviously equation 7.4 provides a quite accurate estimate of the droplet velocity in the range $u_{droplet} < 1.3$ m/s with an error in accuracy of typically less than 0.1 m/s and a deviation in precision of $\Delta u_{max} = \pm 0.1$ m/s.

7.4.5 Determination of droplet volume at variable velocity

In order to study the sensor performance with respect to droplet volume at variable droplet velocity 230 single droplets of individual volumes (volume range V = {26 to 82 nl}) and velocities (velocity range u = {0.17 to 0.96 m/s}) were measured by the sensor CS 1. It was intended to constitute the achieved experimental results to derive the calibration factors (C_1 - C_3) which are essential for the application of the calibration equation 7.3.

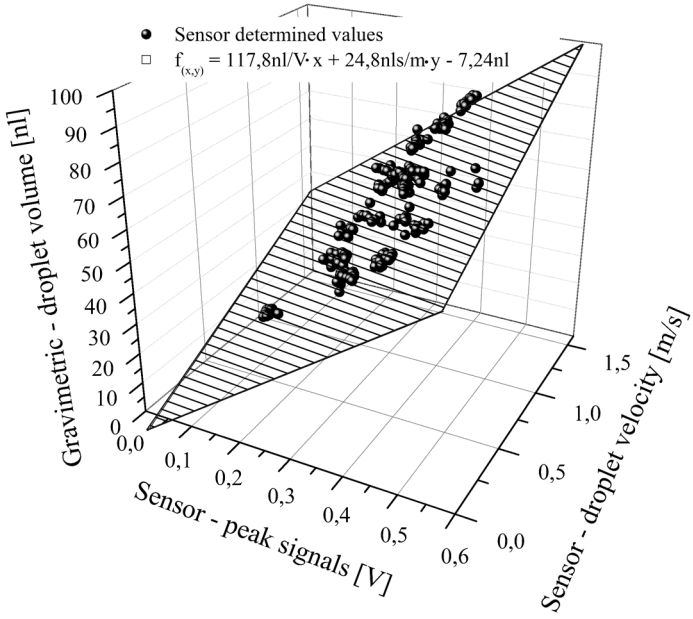

Figure 7.15 Three-dimensional illustration of the relation of the sensor determined droplet velocity, the sensor peak signal and the gravimetric determined droplet volume, including the calibration function as planar fit

Each individual sensor signal was analysed according to equation 7.4 to estimate the droplet velocity. Furthermore, a software supported peak detection method was applied to determine the signal peak values. The corresponding droplet volumes were taken from the gravimetric balance as reference. Figure 7.15 shows the combination of the generated data in a three dimensional plot. The signal peak values are drawn to the x-axis, the droplet velocity on the y-axis and the gravimetric determined droplet volumes are shown on the z-axis. The single data points are indicated by the black balls. The planar fit arises from the sensor generated data and represents the calibration function for the sensor CS 1. The calibration factors C_1 to C_3 were calculated by the application of standard multiple regression estimation [28] and are identified to be C_1 = 117.8 nl/V, C_2 = 29.8 nl·s/m and C_3 = -7.2 nl.

7.4.6 Determination of the sensor accuracy

The definition of the calibration parameters enabled to apply the calibration function to the generated data. This enabled to correlate the sensor determined volumes to the corresponding gravimetrically determined reference volumes to quantify the sensor's accuracy with respect to droplet volume determination. Figure 7.16 shows the gravimetrically determined droplet volume on the x-axis and the corresponding sensor determined volumes on the y-axis. The grey line indicates for an ideal correlation describing the function $y_{(x)} = x$ as guideline to the eye and is not the linear fit.

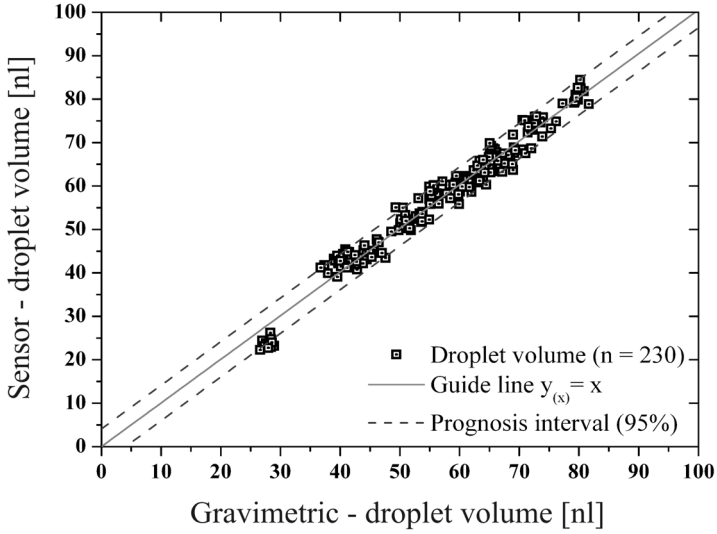

Figure 7.16 Correlation of the sensor determined droplet volumes to the gravimetrically measured droplet volumes. The volume accuracy is determined by the calculated prognosis interval.

The dashed lines are the boundaries of the calculated prognosis interval to estimate the error in volume accuracy of the sensor performance. The prognosis interval was calculated following standard interval estimation techniques [28] and implements an error probability of 5 %. This implies that each future droplet measured by the sensor settles its volume in between this interval boundaries. Based on the applied prognosis interval estimation, the volume accuracy of the sensor CS 1 turns out to be $\Delta V = \pm 3$ nl over the complete measurement range. The multiple regression estimation led to a standard deviation of $\sigma = 2.2$ nl and a coefficient of determination of $R^2 = 0.99$.

7.4.7 Determination of the sensor precision

The basic requirements to identify the precision of the sensor were defined to be a consistent shape of the measured body, a constant volume, a constant movement velocity and a central passage of the measured body through the sensor capacitor. The experiments were implemented by the measurement of one individual spherical wax bead with a diameter of $d_{bead} = 658$ µm. The same bead was pushed through the sensor to be measured 100 times successively. This guaranteed a constant volume at a constant shape. The bead was guided by an $l = 60$ mm long tube with an inner diameter of $ID_{tube} = 750$ µm which was inserted into the measurement capacitor. This enabled a static passage through the measurement capacitor. The bead velocity was assumed to be constant due to the identical conditions for the individual measurements.

The quantitative measure for determination of the sensor precision was the reproducibility of the signal peak values. Neglecting the small but possible position error due to the larger inner diameter of the tube compared to the bead diameter (see later in this chapter), the results of the 100 single measurements led to a peak value range from $U_{max} = \{356 - 380$ mV$\}$ featuring a standard deviation of $\sigma = 6.2$ mV. This yields a precision of the sensor of $\zeta = 0.7$ nl calculated by equation 7.3. The droplet velocity was considered to be constantly at $u_{drop} = 1.0$ m/s.

7.4.8 Determination of the sensor resolution

The sensor resolution is defined by the volume of the smallest detectable water droplet. To generate small droplets, the used PipeJet^{TM} dispenser was equipped with dispensing tubes featuring smaller inner diameters ($ID_{tube} = 200$ µm, see chapter 4). This enables to generate droplets in the range from $V = \{1$ to 25 nl$\}$. The generated droplets were measured by the capacitve sensor, whereas the signal peak values were taken as quantitative measure. Thereby, the PipeJet^{TM} dispenser driving parameters were adjusted to

decrease the volumes of the generated droplets from run to run. This experiment was accomplished until the signal peak value exeeded the region of an evaluable signal to noise ratio. The signal to noise ratio (SNR) describes the ratio of the maximal signal amplitude to the sensor inherent noise. A signal amplitude which is approximately three times the average noise of the signal is considered to be evaluable. Hence, the sensor resolution was identified at a SNR of three. Figure 7.17 shows a signal which was generated by the measurement of a V = 1.5 nl droplet. It features an amplitude of U_{max} = 27 mV at a signal noise of U_{noise} = 8 mV. The resultant signal to noise ratio is SNR = 3.38. The droplet velocity was u_{drop}= 0.6 m/s, taken from the results.

As result of these experiments the sensor resolution was identified to be V_{min} = 1.5 nl. Significantly smaller droplets would lead to signal peak values which can not be analysed reliably. Therefore, a proper volume determination by the sensor would not be guaranteed.

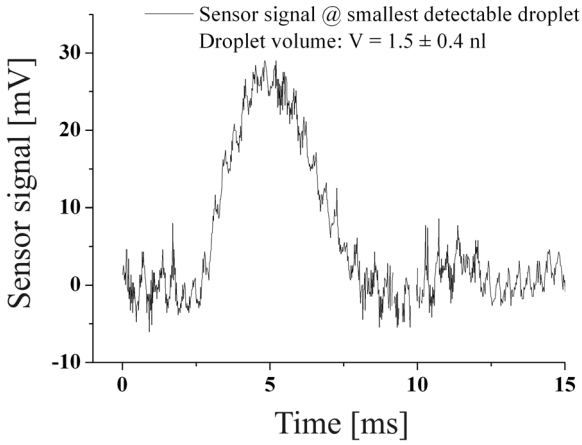

Figure 7.17 Sensor signal generated by a single droplet of V = 1.5 nl defining the sensor resolution. (SNR = 3)

7.4.9 Determination of the sensor sensitivity

The sensor's sensitivity regarding the change in the output signal with respect to the causative droplet volume was determined based on the experiments shown in section 7.4.6. The gained results were analysed applying equation 7.2 to compensate the droplet velocity influence on the signal amplitude. The correlation of the calculated data with the causative droplet volume enabled to evaluate the sensor CS 1 sensitivity by the slope of the linear regression. The sensitivity was identified to be S_i = 5.3 mV/nl.

The evaluated performance enables the sensor CS 1 to be applied for the quantitative non-contact, online measurement of dispensed nanoliter droplets. However, the shown performance might be affected by a variety of influence parameters, which are studied in the following.

7.4.10 Influence of the media relative permittivity

A considerable influence parameter for the application of the presented capacitive measurement method is the influence of the liquid's relative permittivity ε_r.

Equation 6.1 was introduced to provide the theoretical backgroud to calculate the change in capacitance caused by a dispensed droplet. This equation implements the influence of the relative permittivity of a liquid droplet to the change in capacitance by the Clausius-Mossotti factor $f_{\varepsilon r}$ (considering air as surrounding medium) like follows [106]:

$$f_{\varepsilon r} = \left(\frac{\varepsilon_r - 1}{\varepsilon_r + 2} \right) \tag{7.5}$$

Figure 7.18 depicts the factor $f_{\varepsilon r}$ as a function of the relative permittivity ε_r. It can be seen that the influence of small variations in ε_r is almost negligible for liquids with a relative permittivity $\varepsilon_r > 40$ ($\varepsilon_r \approx 40 \rightarrow f_{\varepsilon r} \approx 0.9$). Liquid with very low relative permittivity, e.g. non - polar liquids like oil, imply significantly smaller changes in the measurement capacitance than droplets of liquids featuring relatively high ε_r, e.g. water based on equation 7.5.

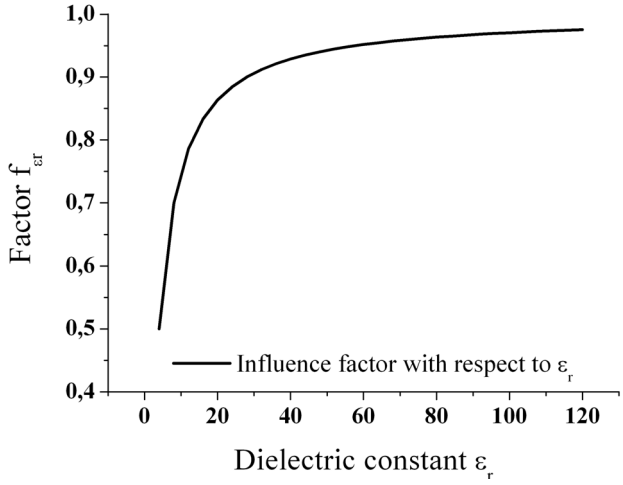

Figure 7.18 Influence of Clausius-Mossotti factor $f_{\varepsilon r}$ versus the droplet media dielectric constant ε_r calculated according to equation 7.5

The experimental validation of the theoretical influence of the relative permittivity on the sensor performance was realised by the measurement of several droplets of different liquids featuring different permittivities. The generation of comparable results using different liquids requires the generation of droplets featuring comparable properties like droplet shape, volume and velocity. This however, requires similar rheology of the certain liquids considering the fundamentals of droplet ejection, see chapter 2. Therefore, aqueous solutions with different saline content were used as sample liquids to study the influence of ε_r on the sensor signal. The dielectric properties of aqueous solutions vary with the saline concentration. This enables to change the relative permittivity of the solutions at nearly constant rheology [107, 108]. Five different sample solutions were prepared to investigate the influence of variable relative permittivity to the sensor performance. The properties of the individual solutions are given in table 7.5:

Table 7.5 Dielectric properties of the used sample solutions.

Solution	**Concentration [mol/l]**	**Dielectric constant ε_r @ 20 °C**
Water	pure (DI)	81
Saline solution	1.0	63
Saline solution	2.0	51
Saline solution	3.0	43
Oil (SHC624)	- - -	~ 2

To generate data at very low dielectric constants a non-polar liquid (gear oil - SHC624, ExxonMobil) was used for the experiments additionally (see table 7.5). Such liquids exhibit extremely different rheology compared to aqueous solutions and require different dispensing parameters to be ejected out of a dispenser nozzle. Furthermore, they tend to form liquid jets instead of spherical shaped droplets implementing non controllable errors for the measurement. The results of these additional accomplished experiments are used to visualize the differet effects to the measurement and the necessity of separate treatment of such liquids.

A validation of the individual droplet formation using the various aqueous solutions was realised by the application of a stroboscopic camera. Figure 7.19 illustrates three sample sequences of pure water droplets compared to an aqueous solution with a saline concentration of c = 3 mol/l. This solution represents the sample with the highest saline concentration, thus the highest rheological modification compared to pure water.

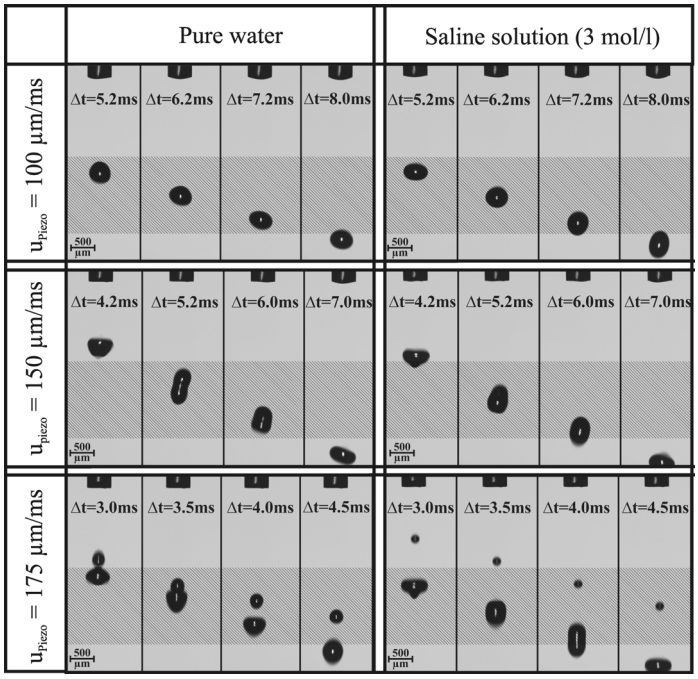

Figure 7.19 Comparison of six stroboscopic droplet ejection sequences of the droplets of pure water - and saline solution (c = 3 mol/l) using the PipeJet™ P18 module at different piezo extension velocities (u_{Piezo}, depict in the left column), and identical piezo extension length (Δl_{Piezo} = 35 µm). A detailed image explanation can be taken from figure 7.13.

The individual sequences were recorded at different piezo extension velocities (u_{Piezo}) to visualize the influence of different kinetic energy transported to the liquid. The piezo extension length was constant for all measurements (Δl_{Piezo} = 35 µm). It can be seen that the droplets formed by the individual solutions are similar in size, shape and velocity. This implies that an increased surface tension caused by the saline concentration does hardly affect the droplet formation process in the considered range. These results enabled to accomplish the planned experiments at comparable droplet properties. Further can be seen that higher kinetic energy transfered to the liquid entails increased deformation of the droplets. Even the splitting of a droplet to several satellite droplets can be identified, see figure 7.19.

The experimental study of the influence of variable relative permittivity was

focussed on the variation of the sensor generated signals by the application of the individual solutions. The droplets were generated at identical dispensing parameters for all aqueous solutions. The ejection of the oil droplets required modifications of the piezo extension velocity to enable the ejection of a droplet. The sensor generated data was evaluated regarding the calibration equation 7.3, applying the identified calibration factors (C_1 to C_3). The calculated droplet volumes were correlated to the gravimetrically determined reference volumes, c.f. figure 7.20. The black line indicates the function $y_{(x)} = x$ to serve as guidline to the eye and is not the linear regression of the data. Obviously, a change of the liquid's relative permittivity in the applied range ($\varepsilon_r = 43$ to 81) does not influenc the droplet volumes significantly. However, for very low relative permittivities, like in case of the tested gear oil, the deviation can be significant. The calculated volumes of the measured oil droplets by the application of the water calibrated sensor does not lead to satisfying values, see figure 7.20. The high deviation can be seen from theory. Whereas the Clausius Mossotti factor in case of the aqueous solutions varies in the range from $f_{\varepsilon r} = 0.93$ to 0.96 only, it takes a value of $f_{\varepsilon r} = 0.25$ for the gear oil. This confirms that the sensor requires a different calibration for liquids with relative permittivites $\varepsilon_r < 43$. Therefore, the assigned error for the present experiment considers the data generated using the aqueous solutions only. It is calculated by standard prognosis interval (95%) estimation and led to an error in volume accuracy of $\Delta V = \pm 8$ nl.

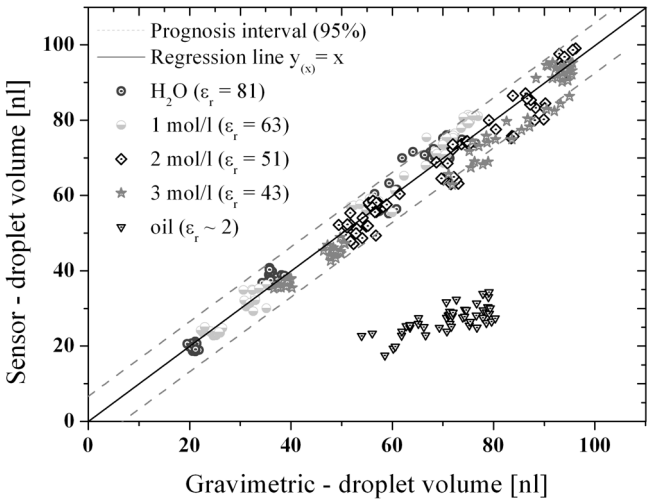

Figure 7.20 Evaluation of the influence of different relative permittivities to the sensor performance. Correlation of the sensor calculated droplet volumes according to equation 7.3 to the gravimetrically determined reference volume of the different sample solutions, see table 7.5.

A possible contribution to the estimated error can be seen by deviations in the flight path of the droplets applying the different solutions. The frequently exchange of the dispensing tube for each of the different sample solutions might have implied a misalignment of the dispenser orifice to the measurement capacitor. This entails deviations in the flight path of the droplets relative to the capacitor's center which contributes to the measurement error. The influence of droplet misalignment is studied in the following chapter. Nevertheless, this study has shown that the relative permittivity of the droplet medium does not influence the sensor performance significantly in the range from $\varepsilon_{\mathbf{r}} = \{43 \text{ to } 81\}$. A theoretical threshold can be seen at a value of $\varepsilon_r \approx 40$. This value entails a Clausius Mossotti factor $f_{\varepsilon\mathbf{r}} = 0.9$, thus all relative permittivities above ($\varepsilon_{\mathbf{r}} > 40$) converge to a Clausius Mossotti factor of $f_{\varepsilon\mathbf{r}} = 1$.

Concluding on this, the experiment indeed confirms the theory that the sensor performance can be considered nearly independent on the relative permittivity $\varepsilon_{\mathbf{r}}$ for liquids featuring relative permittivities larger than $\varepsilon_r \approx 40$ ($\rightarrow f_{\varepsilon r} \approx 0.9$). Beside the evaluation of the influence of $\varepsilon_{\mathbf{r}}$ to the sensor performance this experiment can also be taken as further validation for the deduced calibration factors C_1 to C_3. The results proof that it is possible to operate the sensor with a universal calibration for different liquids. The application of the identical calibration factors as identified previously led to a very high correlation to the reference values even for different liquids. Thus, equation 7.3 in combination with C_1 to C_3 is confirmed to be a precise volume calibration of CS 1 for the contactless measurement of dispensed droplets in the nanoliter range, featuring a relative permittivity $\varepsilon_r > 40$.

7.4.11 Influence of lateral droplet position

Further intension was given on the influence of the lateral position of a droplet in between the capacitor electrodes to the sensor performance. The theoretically inhomogeneous shape of the electric field lines caused by the half shell shape of the capacitor electrodes implies a certain dependency of the sensor performance to the lateral position of a passing droplet. The actual shape of the electric field lines was investigated by the application of the introduced CFD simulation tool, using the actual geometry of the implemented capacitor electrodes. Figure 7.21 shows the results of the electric field simulation. The shape of the electric field is indicated by the drawn field lines, whereas the field strength can be identified by the grey background value. Increasing grey scale intensity goes along with increasing field strength.

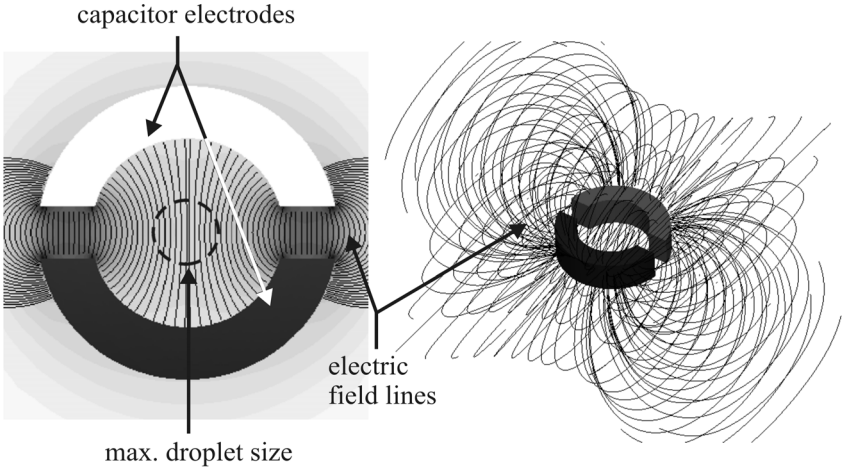

Figure 7.21 Illustration of the electric field distribution based on the CFD simulation of the loaded half shell electrode capacitor. a) top view of the capacitor; b) three dimensional electric field distribution

Thus, the electrical field strength increases in direction towards the capacitor trench (vertical direction in the image), whereas it decreases in direction towards the electrodes (horizontal direction). The inhomogeneity of the electric field is also indicated by the non-parallel field lines. The shown circle indicates for the maximal droplet size which can be ejected using the PipeJet™ dispenser. The distribution of the electric field strength implies the theoretical dependency of the sensor performance on the lateral position of a passing droplet. This can be deduced from Maxwell's first law. Is gives that the influence of a dielectric body (ε_r) inserted into an electric field changes the flux density proportional to the electric field strength *E* [50].

$$\vec{D} = \vec{E} \cdot \varepsilon_r \cdot \varepsilon_0 \tag{7.6}$$

This implies that a droplet passing through a region of initially high electric field strength (e.g. close to the separation trench, see figure 7.21 b) entails a larger change in flux density than passing a region of low electric field strength, thus to a larger change in capacitance of the enclosing plate capacitor. To proof this theory, the influence of the lateral droplet position on the sensor performance was studied by experiment. Five specific droplet positions (a. - e.) were defined, representing the regions of high electric field strength variations, see figure 7.22.

Within the experiment droplets of a water - ink mixture were dispensed through the sensor capacitor at the various positions. The measured droplets impinged on a hydrophobic coated glass slide which was mounted underneath the sensor capacitor. A camera was installed below the glas slide to monitor the actual droplet positions after they passed the sensor capacitor. The water - ink mixture was used to increase the contrast of droplets to the background of the images. The droplet positions yield by the experiment relative to the sensor capacitor are given by the picture sequence in figure 7.22. The schematic sketch on the left side of the image provides the desired target positions of the droplets (a. - e.).

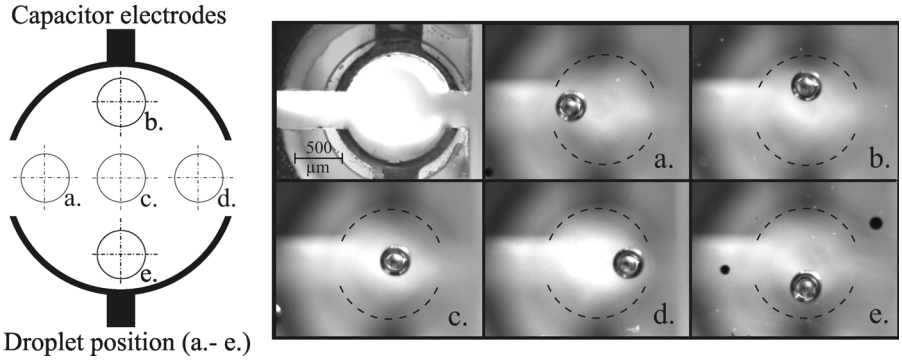

Figure 7.22 Different aspired droplet positions relative to the measurement electrodes vs. actually hit positions to evaluate the lateral position influence to the sensor performance

The diffuse illustration of the capacitor electrodes in the pictures a. - e. results from the small focal depth of the used camera. The dashed lines in the pictures represents the actual shape of the capacitor electrodes inner walls as guideline to the eye only. The sharp image of the sensor, taken at a diffferent optical focus is provided as reference in the left upper corner. All droplets were dispensed at identical dispensing parameters, thus feature equal velocity, volume and shape. Each position experiment was repeated ten times to yield a statistical significant conclusion. The results of the experiment are evaluated by the mean value of the resulting ten sensor signals, generated at each of the certain droplet positions individually. The results are shown in figure 7.23. Each of the sensor signal represents a particular position (a. - e.). The statistical standard deviation of the individual peak values is given by the provided error bars. It can be seen that the signal's shape stays constant for the various positions except the signal peak value changes significantly.

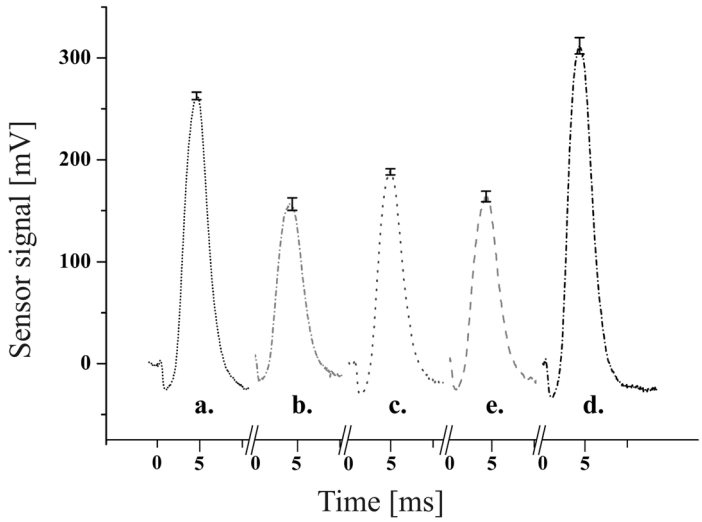

Figure 7.23 Generated sensor signals by single droplets passing the sensor capacitor at different lateral positions c.f. figure 7.22. All droplets were dispensed at identical dispensing parameters.

Like expected, the maximal signal peak values are generated at the positions close to the separation trench of the capacitor (position a. and d.). The lowest signal peaks are generated by the droplets passing the capacitor close to the electrodes (position b. and e.). The center positon, which is the desired measurement position, lead to a value in between. This implies that the experimental results are in agreement with the theory.

From these results the error for the calibrated sensor associated with the position dependency was identified to be max. $\Delta V \approx 12$ nl in the worst case. This arises from the application of the calibration equation 7.3 considering the variation of the signal peak value of approximately $\Delta U = 100$ mV, taken from the experimental results. Obviously, the alignment of the droplet's flight path through the sensor capacitor is an important parameter. Deviations in the flight path direction or misalignment of the nozzle to the sensor capacitor imply systematic errors in the mentioned order.

7.5 Characterisation of sensor CS 2

The following section provides the experimental characterisation of the sensor CS 2. The applied characterisation methods and the basic experimental setups used for the characterisation of sensor CS 2 are identically the same than applied for the characterisation of sensor CS 1. Therefore, the methods and setups won't be given in detail again.

The sensor CS 2 is designed for the application with the PipeJet™ P9 module (see figure 7.24), which is the reason for the smaller outline geometry of the sensor, see figure 7.5. The electronic design is based on capacitive bridge measurement like described in section 7.1. A further deviant aspect in contrast to sensor CS 1 is the requirement of a closed sensor front, based on the applied guardring technology, see section 7.1.2. The used high impedance front - end requires a driven guardring which is realised as strip line, enclosing the sensor capacitor, like depicted in figure 7.24. This strip line acts as third electrode and prevents the falsification of the sensor performance by parasitic leakage currents. A gap in this strip line would disable the proper functionality of the guardring. This aspect disables to monitor a droplet during it's flight through the sensor capacitor to compare the droplets' vertical position to the sensor signal characteristics.

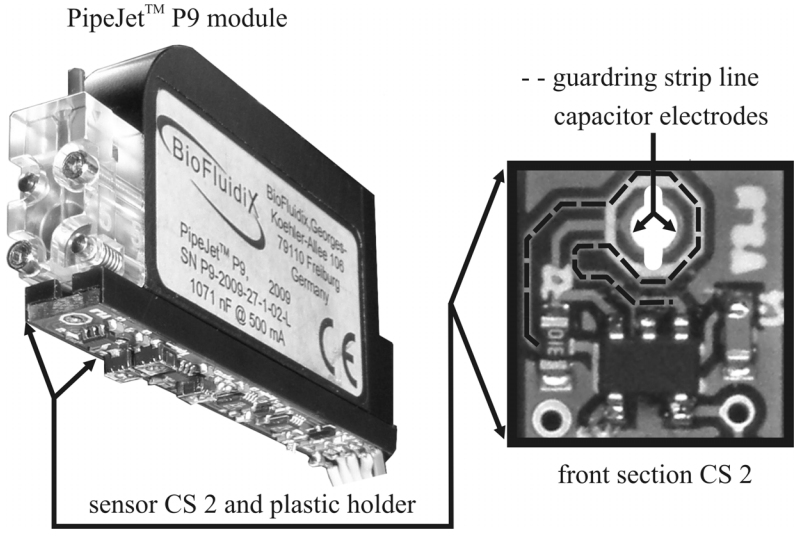

Figure 7.24 PipeJet™ P9 dispenser in combination with the sensor CS 2. The sensor is mounted to the bottom of the the PipeJet™ P9 dispenser by a specitfic plastic holder. The enlarged image visualizes the front section of the sensor CS 2 including the guardring electrode (strip line).

7.5.1 Investigations on typical signal characteristics

To study the typical characteristics of the signals generated by the sensor CS 2, droplets of pure water were dispensed through the sensor capacitor. The droplets were generated at constant piezo extension velocity (u_{Piezo}) and variable piezo extension length (Δl_{Piezo}) to generate droplets of different volumes at equal velocity using the PipeJet^{TM} P9 dispenser. Figure 7.25 shows four typical signals generated by the sensor CS 2 at four representative droplet volumes V = 21, 30, 39, 47 nl. It can be seen that the signals differ in their shape from the known signals generated by sensor CS 1, indicated by the multiple signal peaks. Also the high voltage peaks which reach potentials up to U_{max} = 2.3 V are deviant to the known amlitudes of CS 1. However, the dependency of the signal peak values on the causative droplet volume is still existent.

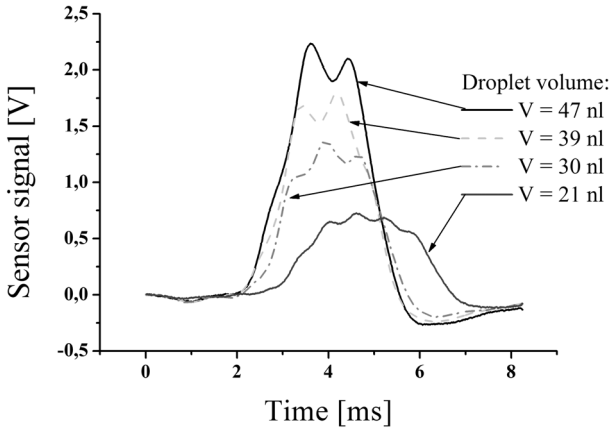

Figure 7.25 Typical sensor signals generated by droplets of different volumes V = 21, 30, 39, 47 nl measured by the sensor CS 2.

Closer examination on the signal characteristics reveals that the multiple signal peaks derive from deformation of the droplets shape during their flight through the measurement capacitor. Theoretically, lateral deformation of a droplet, which means an expansion of the droplet towards the electrodes, leads to higher capacitance changes than longitudinal expansions, see section 6.3.11. Figure 7.26 shows the correlation of the significant extrema in the signal characteristics to the corresponding droplet deformations, given as example. The images of the deformed droplets are take from a stroboscopic image sequence which was recorded without of an installed sensor. The droplets were dispensed at the identical driving parameters like applied for the generation of the 47 nl droplet which led to the displayed signal.

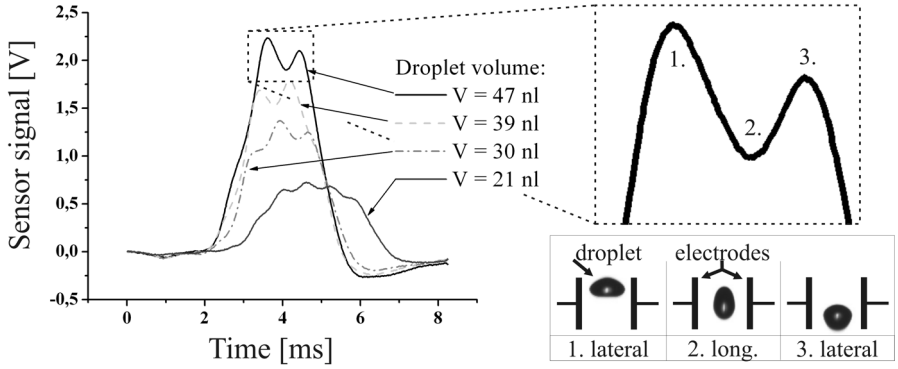

Figure 7.26 Illustration of the droplet deformation influence to the sensor signal. The images of the deformed droplets are taken at the points in time at the generation of the signal extrema without of installed sensor applying a stroboscopic camera.

The images were recorded at the moments in time of the genration of the signal extrema. The three droplet images are drawn to a sketch of the capacitor to visualize the effect of lateral droplet deformation to the signal chracteristics. The vertical droplet positions are estimated. It can be seen that the most lateral deformation leads to the highest signal peak, c.f. figure 7.26. On the other hand, a longitudinal deformation entails a decrease of the signal amplitude. This implies that the maximum signal peak cannot be simply taken as representative quantitative value.

This specific aspect could not be noticed during the characterisation of sensor CS 1. This might be based on the fast signal changes which occur due to the droplet deformation. These are in the time range of $t < 500$ µs which exeed the cut off frequency of the active low pass filter applied at CS 1 (f_g = 1 kHz).

7.5.2 Investigation on droplet volume at constant velocity

The determination of the droplet volume based on the sensor generated data requires the definition of a representative quantitative value. In contrast to the method applied for sensor CS 1 the maximum signal peak value cannot be simply used, see above. Rather a value have to be defined representing the maximum signal change caused by a spherical shaped droplet. A droplet takes a spherical shape in between the change from maximum lateral to maximum longitudinal deformation. This implies that the arithmetic mean value from maximum signal peak (c.f. figure 7.26 - 1. lateral) and it's neighbouring minimum (c.f. figure 7.26 - 2. longitudinal) represents the desired quantitative

value which was taken for the characterisation of sensor CS 2. The first characterisation experiment with respect to the volume sensitivity of the sensor CS 2 consisted of a measurement sequence of 60 droplets of different volumes at equal velocity ($u_{droplet}$= 0.8 m/s). The explained analysis method applied to the sensor generated data led to the results shown in figure 7.27. Here, the representative quantitative mean values are correlated to the gravimetrically determined reference values. It is clearly visible that the sensor CS 2 exhibits a linear behaviour with respect to the droplet volumes applying the described signal analysis method. The measurement sequence led to a coefficient of determination of $R^2 = 0.993$ which indicates for the high linearity and a volume accuracy of $\Delta V = \pm 3$ nl calculated by the application of standard prognosis interval estimation methods [28]. The high volume sensitivity can be seen by the changes in the sensor signal e.g. from the measurement of ~32 nl droplets to ~39 nl droplets. It sums up to approx. ΔU = 350 mV. This implies a volume sensitivity of sensor CS 2 of approx. 50 mV/nl for the measurement of droplets of variable volumes at equal velocity.

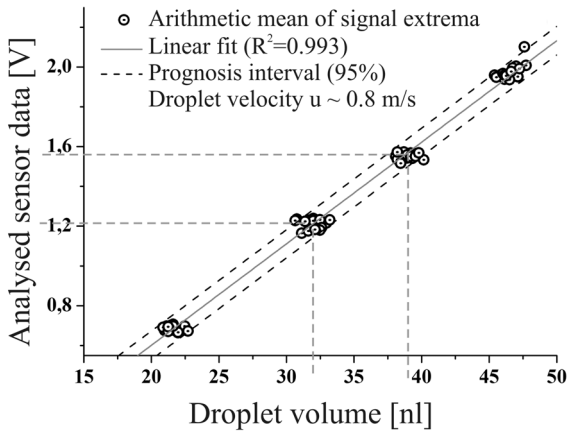

Figure 7.27 Correlation of the calculated sensor values regarding the descibed signal analysis method with the corresponding gravimetrically determined droplet volumes

7.5.3 Study of the influence of variable droplet velocity

Further experiments were focussed on the influence of variable droplet velocity to the sensor performance, see section 7.4.3. It turned out that sensor CS 2 exhibits a linear dependency of the generated signals on the droplet velocity like investigated for sensor CS 1. This implies that equation 7.3 can be reconsidered as calibration equation, considering the representative

analysed signal peak value, see above, and the droplet velocity. Only the calibration factors C_1 to C_3 have to be redefined to the performance of sensor CS 2.

A crucial detail considering equation 7.4 for the droplet velocity determination is the hardly detectable initial negative dip of the CS 2 generated signals. This signal minimum is essential for the application of the droplet velocity determination method explained in section 7.4.4. The absence of this signal characteristics can be explained by the application of the new PipeJet^{TM} P9 dispenser. This module differs in design parameters and materials from the PipeJet^{TM} P18 module applied in section 7.4. The negative signal dip is based on the effect of capacitive coupling, c.f. section 6.3.7, which depends on the conductivity of the used dispenser materials. Mainly the material of the dispensing piston which squeezes the dispenser tube defines the strength of the effect to the signal. This material was changed from brass (PipeJet^{TM} P18 module) to Polyphenylene sulfide (PPS) (PipeJet^{TM} P9 module) featuring completely different electrical conductivities, thus suppressing the effect capacitive coupling mostly. This implies that a novel droplet head velocity determination method had to be applied. An applicable method was found by the consideration of the geometrical defined distance from dispenser nozzle to the sensor capacitors's upper surface (l_{noz}) in correlation with the time (Δt) that a droplet needs to induce a defined signal raise to $U_{thresh,}$ see figure 7.28. This threshold was experimentally identified to be $U_{thresh} = 100$ mV and represents the entry of a droplet into the sensor capacitor. Since droplets of different parameters (velocity, volume, etc.) entail different signal slopes this value might imply a certain error.

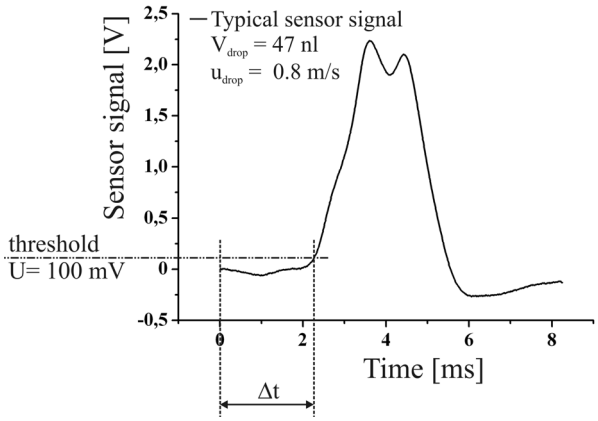

Figure 7.28 Illustration of the applied droplet velocity determination method applied for sensor CS 2. The threshold U_{thresh} is reached when a droplet enters the sensor capacitor.

The ratio of $l_{noz}/\Delta t$ now allows for the determination of the droplet head velocity, which is used for the application of the calibration equation 7.3. Finally the calibration factors C_1 to C_3 were identified by experiment to be $C_1 = 12.1$ nl/V, $C_2 = 22.2$ nls/m and $C_3 = -3.9$ nl applying multiple regression estimation [28].

The validation of the described method was realised by the measurement of 260 individual droplets of unknown volumes and velocities. The application of equation 7.3 considering the specific calibration factors for sensor CS 2 led to the result shown in figure 7.29. It shows the calculated droplet volumes based on the sensor generated data in correlation to the gravimetrically determined droplet volumes as references. The dashed lines indicate for the calculated prognosis interval boundaries (95%) whereas the black line serves as a guideline to the eye indicating the function $y_{(x)} = x$. The volume error which was identified by the calculated prognosis interval implies a maximal deviation of the droplet volumes of $\Delta V = \pm 4$ nl. The multiple regression analysis resulted in a standard deviation of $\sigma = 3.0$ nl and a coefficient of determination of $R^2 = 0.92$.

Obviously these results are somewhat different to the results achieved with sensor CS 1. However, contemplating on the high sensitivity as well as the sensitivity with respect to droplet deformation might distinguish this sensor for specific applications like for example highly precise fingerprinting.

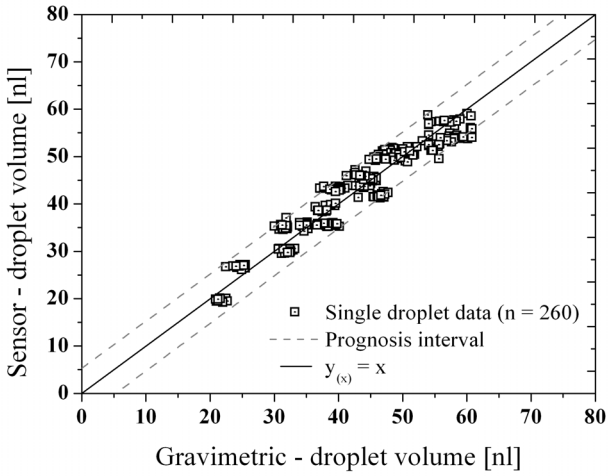

Figure 7.29 Correlation of the droplet volumes calculated by the sensor generated data according to equation 7.3 to the gravimetric determined reference values

7.5.4 Precision, resolution and sensitivty of sensor CS 2

The determination of the sensor performance of sensor CS 2 with respect to sensor precision, resolution and sensitivity was realised by the application of the methods given for the characterisation of sensor CS 1 in section 7.4.7 to 7.4.9.

The precision of sensor CS 2 was identified to be $\zeta = 0.49$ nl, whereas the volume of the smallest detectable pure water droplet was $V_{min} = 6.5$ nl. The sensitivity of the sensor at variable droplet velocities yields $S_i = 77$ mV/nl considering a velocity compensation factor $f_{vel} = 1.87$ Vs/m, c.f. section 7.4.9.

7.5.5 Influence of the media relative permittivity

The influence of the relative permittivity to the performance of sensor CS 2 was studied using the different media given in table 7.5, in accordance to the experiments explained in section 7.5.5. The implied volume error by the measurement of the different saline solutions with relative permittivities in the range from $43 < \varepsilon_r < 81$ was analysed to be $\Delta V = 7$ nl. The theoretically different influence of media with relative permitivities $\varepsilon_r < 40$ could also be verified by the application of sensor CS 2.

7.5.6 Influence of droplet lateral position

The study of variations in the droplet's lateral position with respect to the sensor capacitor electrodes was accomplished by the use of the experimental setup given in section 7.5.6. Ten droplets at the described individual positions were measured to identify the influence of the certain lateral misalignments to the sensor signal. The resulting deviation of the considered signal peak values yields $\Delta U_{peak} \approx 400$ mV, which implies an overall position dependency error of $\Delta V \approx 5$ nl.

7.6 Conclusion on the capacitive measurement method

Comparing the achieved performance of sensor CS 1 and CS 2 it can be said that both sensors yield satisfying results. Especially the accuracy of the measurement for droplets of equal velocity which is in the region of $\Delta V < 2$ nl for both sensors enables the sensors to be applied for the accurate determination of droplet volumes at constant conditions in the low nanoliter range. The velocity error which is compensated by the deduced calibration function increases the error slightly, but enable the application of the sensors for measurement of droplets of unknown properties (volume, velocity, etc.). The determined influence parameters influence the performance of both

sensors similarly and have to be considered for the application of the sensors. The major difference of sensor CS 1 and CS 2 can be found in the sensitivity with respect to the droplet volumes. Whereas sensor CS 1 provides a volume sensitivity of $S_{i\text{-}sensor1} = 5.3$ mV/nl, sensor CS 2 yields a sensitivity of $S_{i\text{-}sensor2} = 77.2$ mV/nl. Furthermore, sensor CS 2 features the property to detect even small deviations in the droplets shape during their flight, reflected by oscillations in the sensor signals. The high sensitivity of sensor CS 2 arises from the applied capacitive bridge measurement technique, implemented by the use of high performance components. This, however increases the fabrication costs to approx. two times the costs of sensor CS 1.

In conclusion it can be said that the implementation of the capacitive measurement technique enabled to realise cost effective sensors for the online measurement of the volume of dispensed nanoliter droplets. The independence of the relative permittivity of the measured liquid, for liquids featuring $\varepsilon_r > 40$, implements an almost media independent sensor which copes with priority 4, defined at the introduction to this work. The small mounting size, realised by the application of printed circuit board (PCB) technology allows for a smart integration to the dispensing device. Even the adaption of the sensor shape to any given requirements can easily be realised by changing the PCB layout. It can be summarized that the given requirements to improve the current drawbacks of the state-of-the-art systems, which are mainly big mounting size and contact measurement principles, could be successfully implemented by the application of the capacitive measurement method.

7.7 Validation of the simulation results

The experimental validation of the achieved simulation results (cf. section 6.3) was initialised by a qualitative comparison of the shape of an experimentally gained signal using sensor CS 1 and a signal generated by CFD simulation. The causative droplets (experiment and CFD simulation) featured similar properties like volume and velocity. The focus of this comparison was on the ratio of the negative signal dip in relation to the maximum rise of the signals. Figure 7.30 shows an overlap of the two signals. The depicted graph combines the simulation results, given in fC on the left y - axis and the experimentally gained signal, given in mV on the right y - axis. It can be seen that the focussed ratio is in good correlation for both signals until the maximum change in charge is reached. Even the rising slope of the signals are in good agreement. The slow signal decay after the maximum signal peak was reached, whichs can be seen in the experimentally gained signal, occurs from the electronic amplification circuit and does not change the information which can be taken from the signal.

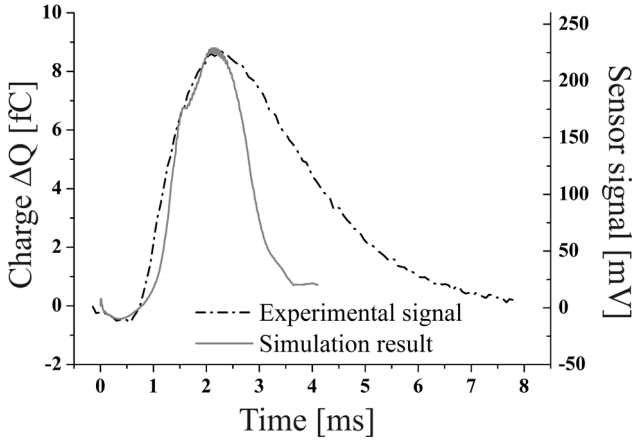

Figure 7.30 Qualitative comparison of a CFD simulation generated signal to an experimentally gained signal.

Further validation was focused on the sensitivity of the measurement technique to the droplet volume. Therefore, the maximum change in charge, taken from the CFD simulation of spherical droplets (cf. section 6.3.5) were fed into the electrical SABER [97] network model (cf. section 7.1.4) to simulate the amplification of the maximum changes in charge to a voltage level considering the electronic amplification circuit of sensor CS 1. The results of the simulation of spherical droplets were applied to cover a wide range of droplet volumes for the validation. The comparison of the simulation results and the experimentally gained changes in charge are shown in figure 7.31. Each experimental data point represents the mean value of the measurement of approximately 60 single droplets. The error bars represent the standard deviation of the recorded data (droplet volume - x - axis; maximum signal peak - y - axis). The error bars applied to the simulation results are defined by the applied grid refinement study given in section 6.3.4.

It can be seen that the sensitivity to the droplet volume S_i, which can be taken from the slope of the linear regressions, is in good agreement for simulation and experiment. Whereas the sensitivity taken from the experiment is S_{i_Exp} = 5.3 mV/nl, the simulation yields a sensitivity of S_{i_Sim} =5.0 mV/nl. Obviously, there is an offset between the measurement and the simulation results, which might be caused by deviations of the actual values of the electronic components used for the implementation of the sensor circuit (e.g. resistance, capacity etc.). The actual values can deviate up to 25% from the ideal values used for the simulation which influences the total amplification.

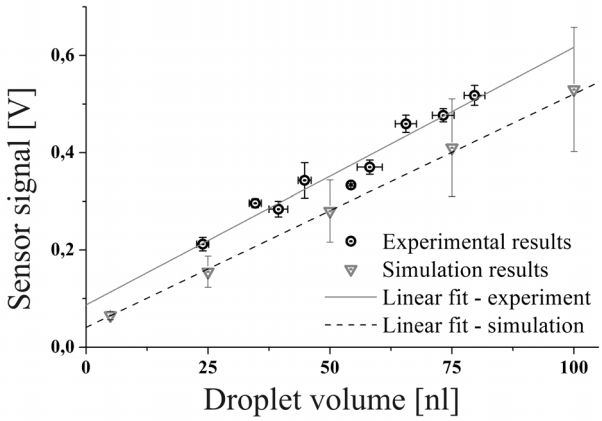

Figure 7.31 Quantitative validation of the simulated changes of the charge caused by single spherically shaped droplets applying CFD simulation with the performance of sensor CS 1. The CFD results are transformed by an established Saber network model to a comparable voltage level using the model of electronic amplification circuit of sensor CS 1.

This offset could probably be explained or compensated by checking each electronic component in the network model as well as the experimental setup for consistency, which is not the objective of this work. Another reason for the off-set might be the limited accuracy of the CFD simulations predicting the change of charge for a given droplet volume used as input to the network simulation as discussed before.

In summary, the results allow for the conclusion that the accomplished CFD simulation leads to a realistic linear scaling behavior and values for the change of the charge which are actually in the region of $\Delta Q < 30$ fC for pure water droplets in the range of $V_{droplet} < 100$ nl. In combination with the Saber network model a complete numerical description of the experimental setup has been accomplished featuring reasonable accuracy and consistency with the experimental results.

Chapter 8
Summary and outlook

The aim of this thesis was the development and the characterisation of sensors to monitor the dispensing process of non - contact nanoliter dispensing systems. The main focus was to implement a contact free measurement method to determine several parameters of single dispensed droplets after they are released out of a dispenser nozzle. In the best case a media independent volume determination of the droplets should be realised. The applied measurement technique must not be disruptive to the dispensing process and deliver the generated data inline. Also a small mounting size to realise a smart system integration and a fabrication in a cost effective manner are in focus.

These requirements are defined to develop a smart solution to eliminate the several present drawbacks of commonly available process control systems. These are mainly big mounting sizes, constraining the system integratability or contact measurement principles, entailing contamination or even loss of the sample medium. Furthermore indirect data processing and the high costs for the commercially available systems which are in the region of multiple 10 k€ are of considerable relevance. Whereas standard quantitative measurement systems like gravimetric balances require a highly complex set up consistent of a vibration damped table and a wind shield cover, the developed sensor systems have to be applicable at any standard industrial environment.

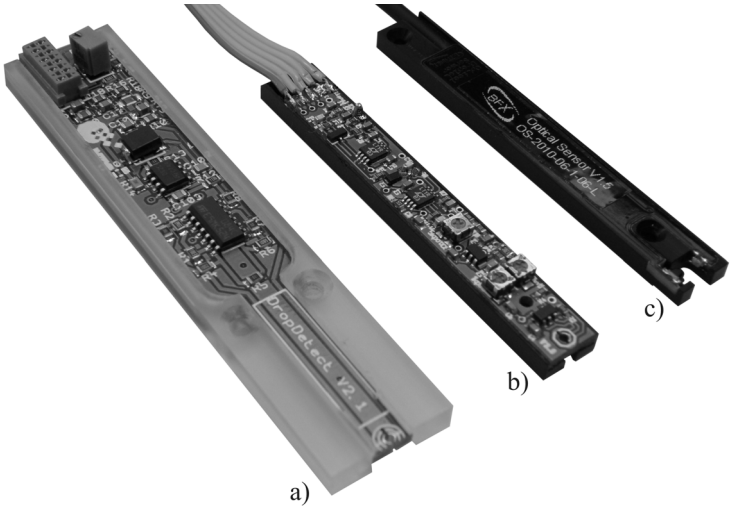

Figure 8.1 Non-contact droplet sensors developed in the presented thesis. A) capacitive sensor CS 1, b) capacitive sensor CS 2 and c) optical sensor OS 1.

The result of the research in this work is the successful implementation of three different sensor systems applicable for process control of dispensing systems, delivering single droplets in the volume range from V = {1.5 to 100 nl}. As feasible measurement techniques an optical approach, based on the effects of geometrical optics as well as a capacitive measurement method are identified. Both methods are applied for the realisation of small sensor units, see figure 8.1, which are studied with respect to their droplet detection performance. The sensors are experimentally characterised using dispensing devices of the PipeJet^{TM} dispenser family.

8.1 Optical measurement method

The optical measurement technique, presented in chapter 5, is based on the interaction of the dispensed droplets with an emitted light ray. A droplet which passes the ray causes a decrease of the light intensity based on effects of geometrical optics. The measurement of the light beam intensity by a photo sensitive element enables to analyse several droplet properties like droplet shape, velocity and even malfunctions in the dispensing process can be detected from one sensor generated voltage signal. A rough estimate for the absolute volume of the measured droplets can be obtained from the maximum voltage change. Beyond the simple detection of the presence of a droplet the voltage signals can be used to implement a semi-quantitative process control. This is realised by the detection of specific droplet 'fingerprint' signals, which encode the specific droplet properties. The correlation of signals, generated by successively dispensed droplets, enables to evaluate the stability of a dispensing process by the detection of the deviations in the signals characteristics. The application of Pearson's r correlation to the recorded data quantifies the stability of the dispensing process by values in the range from 1 to -1, reflecting the consistency of the dispensed droplets. Furthermore, the system facilitates to estimate the droplet velocity in flight with a maximal error in accuracy of $\Delta u_{ac} = \pm 0.3$ m/s and a precision of $\Delta u_{pr} = 0.3$ m/s. The sensitivity to the droplet volume was identified to be $S_i = 62.5$ mV/nl, determined for droplet volumes in the region of V = {42 to 47 nl}. However, it turned out that the sensitivity does not hold a linear behaviour for the entire measurement range. The smallest detectable droplet was identified by experiment to be $V_{min} = 1.5$ nl. Beside the application of the sensor for the detection of single droplets, it is able to measure the volume of ejected liquid jets quantitatively. In contrast to the method to detect single droplets, featuring a size smaller than the height of the measurement light beam, a liquid jet exeeds this length and has to be scanned fractionally while it passes the sensor. The correlation of the generated signals integral to the volume of the measured liquid jets led to a very good linear correlation ($r_{(x,y)} = 0.99$), implying the

feasibility to realise a quantitative measurement method for the determination of the volume of ejected liquid jets.

The optical sensor unit is commercialiced and distributed through BioFluidix GmbH (*http://www.biofluidix.com/index.php?id=124&L=2*), providing a novel level of process control for non-contact dispensing systems. Its simplicity and cost efficiency in combination with the demonstrated performance offers a very smart process control opportunity which is able to be adapted and integrated to a wide range of non - contact dispensing systems. Also the adaption to detect even smaller droplet volumes like presented is feasible using this basic technique. The possibility to identify absent droplets implies the possibility to repair defective droplet patterns by reprinting missing droplets at the certain defective positions. Furthermore, the online evaluation of the process stability enables a first level of quantitative process control. Therefore, incorrect printing sequences can be identified, thus inaccurately produced products can be sourced out. Also the combination of this sensor with liquid jet dispensing valves could revolutionise the world of microliter dispensing. An online volume control enables to implement closed loop controlled dispensing devices implying liquid ejection at highest volume accuracy.

8.2 Capacitive measurement method

The capacitive measurement method is based on the change of the capacitance of an open plate capacitor while a droplet passes through its electric field. A liquid droplet which does not touch any of the capacitor electrodes can be assuemd as dielectric body featuring the liquid materials relative permittivity. Beside the droplet's geometry, the relative permittivity is one of the major influence factors causing the magnitude of the change in capacitance. A numerical simulation study, applying computational fluid dynamics (CFD) simulation, allowed for the definition of the correct system description, which was identified to base on the effect of capacitive coupling. The simulation led to certain design rules enabling the improvement of the sensor geometry to achieve advanced sensor performance with respect to droplet volume determination. The linear dependency of the change in capacitance on the volume of the causative droplet was identified by simulation to be $\Delta C < 3$ fF for the considered volume range. Based on the CFD simulation results two different electronic amplification circuitries were designed, enabling the extraction of analogue voltage signals encoding droplet properties like droplet size or droplet velocity. The implementation of the electronic read out circuitries was improved by specific network simulations, which led to the realisation of two different capacitive sensors (sensor CS 1 and senor CS 2).

Both sensors were fabricated applying printed circuit board (PCB) technology, which enabled a highly cost effective and monolithic integration of the complete read out circuitry. The open measurement capacitor was implemented by the modification of a PCB through connection (via) which is symmetrically separated to created the capacitor electrodes. The sensors were experimentally characterised regarding their droplet detection performance. The target quantity was the change in the output voltage signals with respect to different droplet volumes. It was found that the performance of both sensors was in agreement with theory and featured a linear dependency on the droplet volume for droplets of equal velocity in the range V = {20 to 85 nl}. The droplet volumes could be measured with an accuracy of $\Delta V < \pm 2$ nl in both cases. A certain influence of variable droplet velocity was identified which had to be compensated by a specific calibration function. Therefore, the droplet velocity had to be determined, which could be implemented by the correct interpretation of the sensor generated data with an error of $\Delta u = \pm 0.1$ m/s. This implied an increased error of the measurement accuracy to $\Delta V = \pm 3$ nl for sensor CS 1 and sensor $\Delta V = \pm 4$ nl for sensor CS 2, which are still satisfying results.

Beside the sensitivity to the droplet volume and velocity, the sensors are sensitive to a variety of different influence factors. Especially the influence of deviations in the droplet's lateral position relative to the capacitor electrodes and the influence of the liquid's relative permittivity were studied by experiment. It turned out that deviations in the lateral droplet position, thus deviations in the droplet's flight path, can imply errors up to $\Delta V = \pm 12$ nl in the worst case. A big advantage of this measurement technique is the performance with respect to the liquid type. It was found that changes in the relative permittivity can be neglected if the permittivity exeeds a value of $\varepsilon_r = 40$. Sensor CS 2 is even sensitive to small deformations in the droplet's shape during its flight, which can be seen from fluctuations in the generated sensor signals. Finally, the numerical and analytical simulation results were validated with respect to the performance of sensor CS 1. The correlation of the results led to an admissible small deviation in sensitivity of 5.6%.

The fabricated capacitive sensors, applicable for online process control of non-contact dispensing systems, offer a novel level of global performance compared to state-of-the-art systems. The high volume accuracy in combination with the small mounting size realises an outstanding process control system. Considering the high cost efficiency and the variety of quantitative information, which can be taken from one generated signal, this sensor technique can be seen as serious competitor to the existing control systems. There is no system available which is able to identify a droplet's

volume and velocity directly in flight, without of contact to the medium and independent from the media type. Even the most expensive systems suffer from indirect measurement procedures, contact measurement principles or big mounting size.

It can be concluded that the results achieved in this work form a novel corner stone for the development of process control systems of unprecedented performance. The quality of the presented results are far beyond the successful implementation of the proof of concepts and enable to continue on the improvement of the sensor systems regarding their industrial capability.

Nomenclature

List of symbols

Symbol	Description
A	area [m^2]
A_b	absorbance [-]
a_λ	coefficient of absorbance [-]
α_{water}	contact angle (water) [°]
a	acceleration [mm/s^2]
$\vec{B}$	magnetic flux density [T]
C	capacitance [F]
C_{sens}	capacitance of measurement capacitor [F]
c	concentration [mol/l]
$\vec{D}$	electric flux density [C/m^3]
ΔC	change in capacity [C]
Δx, Δy, Δz	dimension dependent distance [m]
Δx_{bal}	balance error [µg]
Δm_{drop}	systematic mass error [µg]
Δl_{Piezo}	piezo extension length [µm]
Δt	time interval [ms]
ΔV	voltage change [V]
Δp	pressure difference [bar]
$\vec{E}$	electric field [V/m]
E_P	electric field inside a dielectric body [V/m]
E_{kin}	kinetic energy [J]
E_{sur}	surface energy [J]
E_{fric}	friction energy [J]
ε_0	permittivity of free space [8.854×10^{-12} F/m]

ε_r	relative permittivity [-]
η	dynamic viscosity [Pa s]
$f_{\varepsilon r}$	Causius-Mossotti factor [-]
$\vec{F}$	electrostatic force [N]
F_{cap}	capillary forces [N]
f	frequency [1/s]
ϕ	scalar quantity [a.u.]
h_{var}	adjustable distance between nozzle and sensor [m]
$\vec{H}$	magnetic field [Vs]
i	current [A]
k	factor [-]
χ	susceptibility [-]
l	characteristic length [m]
λ	wavelength [nm]
m	mass [kg]
m_{drop}	mass of a single droplet [µg]
m_{before}	balance mass before dispense [µg]
m_{after}	balance mass after dispense [µg]
n	index of refraction [-]
∇	Nabla operator [-]
On	Ohnesorge number [-]
p	relative pressure [bar]
ψ	scalar electric potential [V]
π	pi (3.1415927)
Q	charge [C]
q	volume charge density [c/m^3]
R_s	s - polarization [-]
R_p	p - polarization [-]

Re	Reynolds number [-]
R_B; R_F	fluidic resistance [(N/m^2)/(m^3/s)]
R^2	coefficient of determination [-]
$r_{(x;y)}$	coefficient of correlation [-]
r_{drop}	droplet radius [µm]
r; R	radius [µm]
ρ	density [g/cm^3]
S_i	sensitivity [mV/nl]
σ	surface tension [J/m]
s_x	standard deviation [a.u.]
ζ	precision [a.u.]
$\vec{s}$	distance [m]
T	transmittance [-]
t	time [s]
$t_{n-s;1-a/2}$	quantile of the students t distribution [a.u.]
t_{dis}	time of one dispense [ms]
θ	angle of incidence [°]
θ_c	critical angle for total reflection [°]
τ	time constant [s]
u	velocity [m/s]
U	electric potential [V]
u_{Piezo}	piezo extension velocity [µm/ms]
v_{flow}	liquid flow [cm^3/min]
V_{noise}	voltage noise [V]
V_{init}	initial voltage [V]
V	volume [l]
$\vec{v}$	velocity vector [m/s]
W	work [J]

We	Weber number [-]
We_{crit}	critical Weber number [-]
x_i	discrete datapoint [a.u.]
x^{LR}	linear regression [a.u.]
x^{P}	prognosis interval boundary [a.u.]
$\bar{x}$	arithmetic mean [a.u.]

List of abbreviations

Abbreviation	Description
A/D	analogue/digital
CFD	computational fluid dynamics
csv	comma separated value
DC/DC	direct current/direct current
FVM	finite volume method
GND	ground potential
GUI	graphical user interface
H	height
ID	inner diameter
IC	integrated circuit
kHz	kilo Hertz
L	length
LED	light emitting diode
MHz	mega Hertz
NC	nitro cellulose
NSE	Navier Stokes equation
PLIC	piecewise linear interface construction
p	pitch

PCB	printed circuit board
R_i	electric resistance
SNR	signal to noise ratio
VOF	volume of fluid
VA2	stainless steel (1.4301)
W	width
µC	micro controller

References

[1] M. Engelmann, A, Fekete, I. Gebefügi, P. Schmitt-Kopplin, „The dosage of small volumes for chromatographic quantifications using drop-on-demand dispenser system“, Technical Note, Anal Bioanal Chem, 2007, pp. 1109-1116

[2] P. B. Taylor et al., „A standard operation procedure for assessing liquid handler performance in high-throughput screening“, Journal of Biomulecular Screening, Volume 7, Number 6, 2002

[3] J. Comley, „Continued miniaturisation of assay technologies drives market for nanolitre dispensing“, Drug Discovery World, 2004, pp. 1-8

[4] T. Lindemann, Droplet Generation - From the Nanoliter to the Femtoliter Range, Ph.D. Thesis, IMTEK - Department of Microsystems Engineering, Albert-Ludwigs-University of Freiburg, 2006.

[5] http://www.i-micronews.com/upload/rapports/Inkjet_Head_flyer.pdf

[6] L. R. Allain, M. Askari, D. L. Stokes and T. Vo-Dinh, "Microarray sampling platform fabrication using bubble-jet technology for a biochip system", Fresenius Journal of Analytical Chemistry, vol. 371, no. 2, pp. 146-150, 2001.

[7] F. Takagi, R. Kurosawa, D. Sawaki, S. Kamisuki, M. Takai, K. Ishihara and M. Atobe, "Pico Liter Dispenser with 128 Independent Nozzles For High Throughput Biochip Fabrication", Proceedings of IEEE International Conference on Micro Electro Mechanical Systems, MEMS, Maastricht, The Netherlands, 2004, pp. 276-279.

[8] P. Cooley, D. Wallace and B. Antohe, "Applications of Ink-Jet Printing Technology to BioMEMS and Microfluidic Systems", SPIE Conference on Microfluidics and BioMEMS Proceedings, San Francisco, USA, 2001, pp. 177-188.

[9] A. Kuoni, M. Boillat and N. F. de Rooij, "A Modular High Density Multi- Channel Dispenser for Micro-Array Printing", Proceedings of IEEE Transducers, Boston, USA, 2003, pp. 372-375.

[10] A. Kuoni, M. Boillat and N. F. de Rooij, "A Highly Parallel Piezoelectric Printing Device for Micro-Array Technology", Proceedings of IEEE International Conference on Micro Electro Mechanical Systems, MEMS, Maastricht, The Netherlands, 2004, pp. 466-469.

[11] Shuler et al., „Direct read lateral flow assay for small analytes“, United

State Patent 5.798.273, 1998

[12] G. A. Posthuma-Trumpie, J. Korf, A. van Amerongen, „Lateral flow (immuno)assay: its strengths, weaknesses, oppotunities and threats. A literature survey“, Anal Bioanal Chem, 2009, pp. 569-582

[13] T. C. Tisone, H. Citeau, B. McIntosh, „In-line processing trends for lateral-flow immunoassay manufacturing“, IVD Technology, June 2007, Vol. 13, No. 5

[14] I. A. Darwish, D. A. Blake, „One-Step Competitive Immunoassay for Cadmium Ions: Development and Validation for Environmental Water Samples“, Anal. Chem., 2001, 73 (8), pp 1889–1895

[15] DELO Industrie Klebstoffe, DELO-Allee 1, 86949 Windach, Deutschland, *http://www.delo.de*

[16] Microfab GmbH, Lise Meitner Straße 5, 28359 Bremen, Germany, *http://www.microfab.de*

[17] D. B. Wallace and D. J. Hayes, "Solder Jet Technology Update", The International Journal of Microcircuits and Electronic Packaging, vol. 21, no. 1, 1998.

[18] J. Wei et al., „J. Wei et al., „Fabrication of vertical electrodes on channnel sidewall for picoliter liquid measurement“ Proc. of Transducers and Eurosensors, Lyon 2007, pp. 1013-1016

[19] J. Wei et al., „Implementation and characterization of a femto-farad capacitive sensor for pico-liter liquid monitoring“, Poc. of Eurosensors XXIII, 2009

[20] K. Thurow, T. Krüger, N. Stoll, „An optical approach for the determination of droplet volumes in nanoliterdispensing“, Journal of Automated Methods and Management in Chemistry, Volume 2009, Article ID 198732

[21] A. C. Best, „The size distribution of rain drops“, Quarterly Journal of the Royal Meteorological Society, 1950, pp. 16-36

[22] B. J. Mason, R. Ramanadham, „A photoelectric raindrop spectrometer“, Q.J.R. Meteorol. Soc., 79: 490–495. doi: 10.1002/qj.

[23] Battan, L.J., R.R. Braham, „a study of convective precipitation based on cloud and radar observations“, J. Atmos. Sci., 13, 587–591. al of the Royal Meteorological Society, 1953, pp. 490-495

[24] W. P. Winn, „An electrostatic theory for instruments which measure the radii of water drops by detecting a change in capacity due to the presence of a drop“, J. Appl. Meteor., vol. 7, 1968, pp. 929–937

[25] H. Liu, „Science and engineering of droplets: fundamentals and applications“, William Andrew Publishing, LLC Norwich, New York, USA, 2000, ISBN 0-8155-1436-0

[26] Sartorius AG, Weender Landstrasse 94-108, D-37075 Goettingen, Germany
http://www.sartorius-mechatronics.com/DE/de/Ultramikro--Mikrowaagen/Mikrowaagen--Ultramikrowaagen-ME-SE-/

[27] Chr. Berg, et al., „Grundlagen der Wägetechnik“, Sartorius AG 1995, 2, Auflage, 1996

[28] Schaum's outlines: Probability and Statistics, second edition, McGraw-Hill Company, 2000, ISBN 0-07-135004-7

[29] Kuang-Chao Fan et al., „Precision in situ volume measurement of micro droplets“, Journal of Optics A: Pure and Applied Optics, Volume 11, Number, 2009

[30] BioFluidix GmbH, Georges Köhler Allee 103, 79110 Freiburg, Germany, *http://www.biofluidix.com*

[31] Reinhard Steger, Benjamin Bohl, Roland Zengerle, Peter Koltay, „The dispensing well plate: a novel device for nanoliter liquid handling in ultra high-throughput screening“, Journal of the Association for Laboratory Automation (JALA), Vol 9, Issue 5, 2004, 291-299

[32] M. Hof, R. Hutterer, V. Fidler, „Fluorescence Spedcroscopy in Biology“, Springer-Verlag Berlin Heidelberg New York 2005, ISBN 3-540-22338-x

[33] O. Hidetaka, S. Norihisa, Y. Kenji, „Method for controlling amount of dispensation“, Japanese Patent JP 2004/251818, 2004

[34] J. E. Pillion et al., „Process and system for determining acceptibility of a fluid dispense“, United State Patent, US 6,617,079 B1, 2003

[35] H. W. Meinhold et al., „Sensor for detecting droplet characteristics“, United State Patent, US 6,764,168 B1, 2004

[36] H. Arakawa et al. (Konica Corporation), „Microscopic droplet detecting device and ink-jet recording apparatus“, United State Patent, US 6,726,318 B1, 2004

[37] S. Samrast et al. (Hellwett-Packard Company), „Methods and systems for detecting and determining trajectories of ink droplets“, United State Patent, US 2003/0011663 A1, 2003

[38] J. M. Carmichael et al., „Charge detection for ink jet printers“, United State Patent, US 3,852,768, 1974

[39] S. Bukshpan et al., „Automatic recording volume measurement apparatus“, United State Patent, US 2009/0055131 A1, 2009

[40] M. C. Barret et al., „Methods and apparatus for characterising, measuring, and dispensing fluid“, International Patent, WO 2005/ 121780 A2, 2005

[41] H. Hayashi et al., „Quantitative dispenser for a liquid“, United State Patent, US 4,944,922, 1990

[42] M. Boillat et al. (Seyonic SA), „Fluid dispensing device“, European Patent, EP 1 327 152 B1 (WO 2002/033423), 2001

[43] Seyonic SA, Rue du Puits-Godet 12, CH-2000 Neuchâtel, Switzerland, *http://www.seyonic.com/*

[44] Yaxin Liu, Liguo Chen and Lining Sun, „Design and Fabrication of a MEMS Flow Sensor and Its Application in Precise Liquid Dispensing“, Sensors 2009,9,4138-4150

[45] HSG-IMIT, Institut für Mikro- und Informationstechnik, Wilhelm-Schickard-Straße 10, D-78052 Villingen-Schwenningen, Germany, *http://www.hsg-imit.de/*

[46] M. Ashauer et al., „New applications for thermal flow sensors“ , Proc of Sensor 2001, Nürnberg, Germany

[47] W. Streule, M. Storz, S. Gracki, M. Ashauer, R. Zengerle, P. Koltay, „Kontaktfreie und medienunabhängige Volumenbestimmung in Nanoliter Dispensern“, Proc. Mikrosystemtechnik-Kongress 2005; Freiburg, Germany, 2005

[48] Eugene Hech, „Optik“, 4., überarbeitete Auflage, Oldenbourg Wissenschaftsverlag GmbH, München, 2005

[49] S. Jewett, „Physics for Scientists and Engineers“, 6th Edition; Thomson Brooks/Cole, 2004, ISBN 0534408427

[50] J.D. Jackson, "Classical Electrodynamics 3rd edition", 1998, ISBN 0-471-30932-x

[51] Helmut Lindner, „Physik für Ingenieure“, Fachbuchverlag Leipzig im Carl Hanse Verlag, 2001, ISBN 3-446-21703-7

[52] J. D. Anderson, „Computational Fluid Dynamics“, 1st Edition, McGraw-Hill, Science/Engineering/Math, 1995.

[53] CFD ACE+ V2009.4, Modules Manual, Part 2, pp. 124- 153, ESI CFD Inc., 6767 Old Madison Pike, Ste. 600, Huntsville, AL 35805

[54] C.W. Hirt and B.D. Nicholson, „Volume of fluid (VOF) method for the

dynamics of free boundaries“, J. Comp. Phys., 39, pp. 201-225, 1981

[55] J. W. Rider and D. B. Kothe, „Reconstruction volume tracking“, J. Comp. Phys., 14, 112, 1998

[56] D. B. Kothe, W. J. Rider, W.J. Mosso and J. S. Brock, „Volume tracking of interfaces having surface tension in two and three dimensions“, AIAA, 96-0859, 1996

[57] CFD-ACE+, ESI CFD, Inc., *http://esi-group.com, http://www.cfdrc.com, 2010.*

[58] CFD ACE+ V2009.4, Modules Manual, Part 2, pp. 12-60, ESI CFD Inc., 6767 Old Madison Pike, Ste. 600, Huntsville, AL 35805

[59] A. Tarnogrodzki, "Theoretical Prediction of the Critical Weber Number", International Journal of Multiphase Flow, vol. 19, no. 2, pp. 329-336, 1993.

[60] E. R. Lee, Microdrop Generation, 1 ed., Boca Raton: CRC Press, 2002.

[61] W. von Ohnesorge, "Die Bildung von Tropfen an Düsen und die Auflösung flüssiger Strahlen", Zeitschrift für angewandte Mathematik und Mechanik, vol. 16, no. 6, pp. 355-358, 1936.

[62] Wolfgang Streule, Timo Lindemann, Gerhard Birkle, Roland Zengerle, Peter Koltay, „PipeJet: a simple disposable dispenser for the nano- and microliter range“, Journal of the Association for Laboratory Automation (JALA), Vol 9, Issue 5, 2004, 300-306

[63] W. Streule, „Non-contact liquid dispensing for the nano- and microliter range based on the PipeJet technology“, Dissertation University of Freiburg - IMTEK, 2011

[64] MSP430x11x Mixed Signal Microcontrollers, Texas Instruments, *http://www.ti.com/ww/de/msp430.htm*

[65] Blue Sky and Rayleigh scattering *http://hyperphysics.phy-astr.gsu.edu/hbase/atmos/blusky.html#c2*

[66] Mie-Streuung und Lokalisierung *http://www.staff.uni-mainz.de/oschmidt/thesis/node15.html*

[67] Osram GmbH, Hellabrunner Straße 1, 81543 München *http://catalog.osram-os.com/catalogue/*

[68] Sharp Electronics (Europe) GmbH, Sonninstraße 3, 20097 Hamburg *http://www.sharpsme.com/Page.aspx/europe/en/part/PT100MF1MP1/*

[69] Honeywell International Inc., Product Page HOA 1397-03 *http://sensing.honeywell.com/*

[70] A. Beer, „Bestimmung der Absorption des roten Lichts in farbigen Flüssigkeiten“, Annalen der Physik und Chemie 86 (1852), pp. 78–87

[71] M. Born and E. Wolf, „Principles of Optics: Electromagnetic Theory of Propagation, Interference and Diffraction of Light (7th ed.)“, Cambridge University Press, Cambridge, United Kingdom (1999) ISBN:0-521r-r64222-1, pp. 40–45

[72] Beta Layout GmbH, Im Aartal 14, 65326 Aarbergen
http://www.pcb-pool.com/

[73] robotmech Rapid Prototyping Stössl GmbH, Bundesstraße 11, 6842 Koblach
http://www.robotmech.com/stereolithografie.html

[74] TC Tisone, "In-Line Manufacturing for Rapid-Flow Diagnostic Devices", IVD Technology 6, no. 3 (2000), pp. 43-60

[75] TC Tisone, "Dispensing Systems for Miniaturized Diagnostics", IVD Technology 4, no. 3 (1998), pp. 40-46.

[76] J. L. Rodgers and W. A. Nicewander, „Thirteen ways to look at the correlation coefficient“, The American Statistician, 42(1): 59-66, Feb 1988

[77] L.D. Landau, E.M. Lifschitz, „Lehrbuch der theoretischen Physik VIII - Elektrodynamik der Kontinua“, Akademie-Verlag GmbH, 108 Berlin, 1967

[78] W. Ko, M. Bao and Y. Hong, „A high sensitivity integrated circuit capacitive pressure transducer“, IEEE Trans Electron Devices, ED-29, 48-56, 1983

[79] J. Summto, G. Yeh, T. Spear and W. Ko, „Silicon diaphragm capacitive sensor for pressure, flow, acceleration and altitude measurements“, Proc. 4th Int Conf Solid-State Sensors and Actuators (Transducers ’87) Tokyo, Japan, June 2-5, 336-339, 1987

[80] A. Hanneborg, T. Hansen, P. Ohlkers, E. Calson, B. Dahl and O Holwech, „A new integrated capacitive pressure sensor with frequency modulated output“, Proc. 3rd Int Conf Solid-State Sensors and Actuators (Transducers ’85), Philadelphia, PA, USA, June 7-11, 186-188, 1985

[81] D. Olney, „Acceleration measurement using variable capacitance“, Proc. Sensors Nürnberg ’88, Germany, 149-160, 1988

[82] Y. Lee and K. Wise, „A batch-fabricated silicon capacitive pressure transducer with low temperature sensitivity“, IEEE Trans Electron

Devices, ED-29, 42-48, 1982

[83] C. Sander, J. Knutti and J. Meindl, „A monolithic capacitive pressure sensor with pulsed period output“, IEEE Trans Electron Devices, ED-17, 927-930, 1980

[84] G. Delapierre, H. Grange, B. Chambaz, L. Destannes, „Polymer-based capacitive humidity sensor: characteristics and experimental results“, Sensors and Actuators, Volume 4, 1983, pp. 97-104

[85] A. Ernst, W. Streule, P. Koltay, and R. Zengerle, „Non-contact detection of free flying nanoliter droplets“, Transducers & Eurosensors ’07, Lyon, France, 2007, 751-754

[86] Phillip L. Geissler, Christoph Dellago, David Chandler, Jürg Hutter, Michele Parrinello, "Autoionization in Liquid Water", Science, 16 March 2001, Vol. 291. no. 5511, pp. 2121 - 2124

[87] K. Mutschler, „Investigation of electric field characteristics with respect to capacitive droplet detection using CFD-simulation“, Diploma Thesis, IMTEK - Department of Microsystems Engineering, Albert-Ludwigs-University of Freiburg, 2010.

[88] J. Auge, K. Dierks, S. Prange, B. Henning, „Monitoring of droplet growth with nano-litre resolution for liquid flow rates, level or surface measurement“, Sens. Actuator A 110 (2004) 18–27.

[89] L.K. Baxter, „Capacitive Sensors—Design and Applications“, John Wiley & Sons, 1997.

[90] B. T. Williams, "Low impedance electrostatic detector", United States Patent, US 4,370,616, 1983

[91] D. Marioli, et al., „Measurement of small capacitance variations“, IEEE Trans.Instrum. Meas. 40 (2), 1991

[92] R.J. Widlar, „IC Op Amp Beats Fets on Input Current“, National Semiconductor, Application Note 29, September 2002

[93] EXAR, Corporate Headquarters, 48720 Kato Road, Fremont, CA 94538, USA
http://www.exar.com

[94] C&D Technologies, Inc., 1400 Union Meeting Road, Blue Bell, Pennsylvania 19422-0858 USA
http://www.cdtechno.com

[95] U. Tietze, Ch. Schenk, „Halbleiter-Schaltungstechnik“, 11. Auflage, Springer Verlag Berlin Heidelberg New York, 1999, ISBN 3-540-64192-0

[96] Meilhaus Electronic GmbH, Fischerstraße 2, 82178 Puchheim, Germany
http://www.meilhaus.de

[97] Synopsis, *http://www.synopsys.com/home.aspx (2010)*.

[98] J. Franz, „Methods to Measure Small Capacitances with high resolution“, Technisches Messen 67, 2000

[99] Ing.- Büro Friedrich, Am Schwarzen Rain 1,6124 Eichenzell, Deutschland, *http://server.ibfriedrich.com/ (2010)*

[100] *http://de.farnell.com (2010)*

[101] Jürgen Behrendt Feinmechanik, Schwenninger Straße 21, 78083 Dauchingen
http://www.juergen-behrendt.de

[102] A. Ernst, W. Streule, R. Zengerle, P. Koltay, “Quantitative volume determination of dispensed nanoliter droplets on the fly“, Proc. Transducers, Denver, Colorado, USA, 2009, 1750-1753

[103] Lin Feng, Zhongyi Zhang, Zhenhong Mai, Yongmei Ma, Biqian Liu, Lei Jiang, and Daoben Zhun,“A Super-Hydrophobic and Super-Oleophilic Coating Mesh Film for the Separation of Oil and Water“, Angew. Chem. Int. Ed. 2004, 43, pp. 2012 –2014

[104] cetoni GmbH, Gewerbegebiet Korbwiesen, Am Wiesenring 6, 07554 Korbußen,
http://www.cetoni.de/produkte/spritzenpumpe_nemesys.html (2010)

[105] IDS Imaging Development Systems GmbH, Dimbacher Strasse 6-8, 74182 Obersulm, *http://www.ids-imaging.de/ (2010)*

[106] Stephen J. Paddison, Reginald Paul and Karan V.I.S. Kaler, “Multiple valued Clausius–Mossotti Factors Resulting from Nonlinear Boundary Conditions: An Exactly Solvable Model“, IEEE EMBS Proceedings of “The Sixteenth Annual International Conference, Engineering Advances: New Opportunities for Biomedical Engineers”, 16, 301-305 (1994).

[107] A. Horibe, S. Fukusako and M. Yamba, "Surface tension of low-temperature aqueous solutions", International Journal of Thermophysics, Vol. 17, No. 2, 1996

[108] J.A. Lane and J.A. Saxton, "Dielectric dispersion in pure polar liquids at very high radio frequencies", Proceedings of the Royal Society of London. Series A, Mathematical and Physical Sciences (1952)

Acknowledgement

I would like to thank Prof. Dr. Roland Zengerle for the possibility to work on this 'sensitive' topic at the chair for MEMS applications and the opportunity to write this thesis. I also thank Prof. Dr. Leonard Reindl for co-referee the thesis. Furthermore, I'd like to thank Dr. Peter Koltay for his great support, crazy ideas and nice climbing sessions.

Thanks to Prof. Dr. Bernhard Vondenbusch and Lin Ju for the good project collaboration and the support in electrical engineering.

Thanks to Dr. Wolfgang „W0lli" Streule who initiated the sensor topic at IMTEK.

Thanks to the diploma and bachelor students Julien Troendle, Norbert Schmitt, Matthias Pohl and Klaus Mutschler who worked on different sensor topics and supported this thesis by their specific works.

Special thanks to Nils Paust and Laurent Tanguy who supported the simulation work intensively and answered every question.

Thanks to my BioFluidix colleagues - market leaders in PipeJet dispensing -

Dr. Lutz Riegger - expert in computer science and surface chemistry

Dr. Chris Steinert - big upper arm and big brain.

Norbert Schmitt - electrician, philosopher and paraglider

Julien Tröndle - expert in marketing questions and design

Matthias Blümle - the new guy in the team and worth to be mentioned

Dr. Peter Koltay and Dr. W0lli - who were already mentioned above

Great thanks to Melanie Baumann and Ulrike Grundmann - the most efficient secretary team in the world. No chair without of you! Thanks for all your support and nice words.

Thanks to all the lab members and colleagues at the chair for MEMS applications for the nice time, all the funny moments and fruitfull discussions.

All my love to my wife Carolin and my chlildren Sarah and Jonah for being the best family in the world.